

Comparison of the magnetic properties of ferromagnetic films and nanostructures

Dissertation
zur Erlangung des Doktorgrades
an der Fakultät für Mathematik, Informatik und Naturwissenschaften
Fachbereich Physik
der Universität Hamburg

vorgelegt von
STEFAN FREERCKS

Hamburg
2020

Gutachter der Dissertation:

Prof. Dr. Hans Peter Oepen
Prof. Dr. Robert H. Blick

Zusammensetzung der Prüfungskommission:

Prof. Dr. Hans Peter Oepen
Prof. Dr. Robert H. Blick
Prof. Dr. Wolfgang Hansen
Prof. Dr. Daniela Pfannkuche
Prof. Dr. Dorota Koziej

Vorsitzender der Prüfungskommission:

Prof. Dr. Wolfgang Hansen

Datum der Disputation:

17.11.2020

Vorsitzender des Fach-Promotionsausschusses PHYSIK:

Prof. Dr. Günter H.W. Sigl

Leiter des Fachbereichs PHYSIK:

Prof. Dr. Wolfgang Hansen

Dekan der Fakultät MIN:

Prof. Dr. Heinrich Graener

Abstract

This thesis deals with the magnetic properties of ultrathin Pt/Co/Pt films and nanostructures. The films are sputtered under high vacuum conditions. The nanostructures are then fabricated from the films by using electron beam lithography and argon ion milling. Pt/Co/Pt multilayers possess an uniaxial anisotropy that is either in-plane or out-of-plane, depending on the thickness of the cobalt layer.

Pt/Co/Pt multilayer with an in-plane anisotropy are investigated and the temperature dependence of the magnetic anisotropy is measured. The Co thickness t_{Co} is varied and the films are either sputtered on a SiO_2 or Si_3N_4 substrates. At $t_{\text{Co}} \leq 2$ nm the anisotropy increases linearly with increasing temperature for both substrates. For thicker films the anisotropy decreases. Interface and volume anisotropy have been determined. The interface anisotropy linearly increases with increasing temperature, while the volume anisotropy decreases. Since the conventional method to determine the volume and interface anisotropy assumes that the interfaces between Co and Pt are perfect, a model is proposed that takes alloying at the interfaces, caused by interdiffusion, into consideration. Due to the alloying, the saturation magnetisation is reduced with increasing temperature, resulting in an increase of the anisotropy. The effect on the volume anisotropy is negligible. However, the conventional approach of using sharp interfaces, overestimates the interface anisotropy.

For single magnetic nanostructures, the magnetisation behaviour has been investigated. The three dimensional switching surface has been measured and a deviation from the uniaxial anisotropy model is found. It is known from previous simulations [1], that these deviations stem from a tilt between different anisotropy contributions, that is caused by the local grain structure.

While measuring the temperature dependence of the switching field in the blocked regime and the switching frequency in the superparamagnetic regime, a too high attempt frequency of the Néel-Arrhenius law is found. Since the temperature dependence of the anisotropy can explain such a behaviour, the latter is measured. The temperature dependence is inherited from the initial film possesses however, the wrong sign to correct the too high attempt frequency.

In conclusion, the thesis proves that often overlooked properties, like the inter-

faces in metallic multilayers or the tilting of the grains, can have a significant influence on the magnetic properties of films and nanostructures and should not be neglected.

Zusammenfassung

Diese Arbeit widmet sich den magnetischen Eigenschaften von ultradünnen magnetischen Filmen, sowie magnetischen Nanostrukturen. Die Filme werden im Ultrahochvakuum mittels Sputterdeposition hergestellt. Die Nanostrukturen werden mit Elektronenstrahlolithographie und Ionenätzen aus den Filmen erzeugt. Bei den untersuchten Proben handelt es sich um Pt/Co/Pt-Schichtsysteme. Dieses System zeichnet sich durch eine uniaxiale Anisotropie aus, welche abhängig von der Kobalt Schichtdicke aus der Filmebene heraus zeigt oder parallel zur Filmebene liegt. Es wurden temperaturabhängige Messungen der Anisotropie von Filmen durchgeführt für verschiedene Kobalt-Dicken und verschiedene Substrate. Die leichte Achse der Magnetisierung liegt in der Filmebene. Dabei konnte gezeigt werden, dass die Anisotropie mit steigender Temperatur linear ansteigt. Das Vorzeichen der Steigung ist abhängig von der Co-Dicke. Bemerkenswert ist die positive Steigung bei dünnen Co-Schichten. Weiterhin wurde die Temperaturabhängigkeit der Grenzflächen- sowie der Volumenanisotropie bestimmt. Für die Ermittlung der Anisotropiekonstanten werden perfekte Grenzflächen angenommen. Es wird ein Model vorgestellt, welches den Einfluss einer Legierungsbildung an den Grenzflächen berücksichtigt. Es konnte gezeigt werden, dass die Legierungsbildung zu einer Reduzierung der Sättigungsmagnetisierung führt. Während der Einfluss auf die Volumenanisotropie vernachlässigbar ist, führt die Annahme scharfer Grenzflächen zu einer Überschätzung der Grenzflächenanisotropie.

Für eine einzelne Nanostruktur wurde die drei-dimensionale Schaltfläche gemessen. Diese weicht stark vom uniaxialen Anisotropiemodel ab. Frühere Simulationen von Staeck [1] haben gezeigt, dass dieses Verhalten auf die lokale Kornstruktur zurückzuführen ist. Die Verkippung der Körner, führt zu einer Verkippung der einzelnen Anisotropiebeiträge.

Die Temperaturabhängigkeit des Schaltfeldes sowie der Schaltfrequenz ergeben eine zu hohe Versuchsschaltfrequenz. Da dieses durch die Temperaturabhängigkeit der Anisotropie erklärt werden kann, wird letztere untersucht. Die Temperaturabhängigkeit wird vom ursprünglichen magnetischen Film übertragen, besitzt aber das falsche Vorzeichen um die Abweichung der Versuchsschaltfrequenz zu erklären. Zusammenfassend zeigt diese Thesis, dass häufig vernachlässigte Eigenschaften, wie die Legierungsbildung an den Grenzflächen oder die lokale Kornstruktur, die

magnetischen Eigenschaften von Filmen und Nanostrukturen beeinflusst und nicht ignoriert werden sollten.

Contents

1	Introduction	1
2	Theoretical background	5
2.1	Basics of magnetism	5
2.2	Magnetic energy terms	6
2.3	Single domain systems	11
2.3.1	Stoner-Wohlfarth model	13
2.3.2	Domain wall nucleation	17
2.4	Thermal effects	17
2.5	Magnetotransport effects	19
2.5.1	Longitudinal magnetoresistance effects	20
2.5.2	Transversal magnetoresistance effect	23
3	Sample preparation and experimental details	25
3.1	Pt/Co/Pt sample system	25
3.2	Measurement technique	27
3.3	Lithography and nano-structuring	29
3.4	Experimental setup	34
4	Magnetisation behaviour of ultrathin magnetic films	37
4.1	Temperature dependence of the anisotropy in ultrathin magnetic films	37
4.1.1	Introduction	37
4.1.2	Determination of anisotropy constants in magnetic films	40
4.1.3	Silicon oxide substrate	41
4.1.4	Silicon nitride substrate	48
4.1.5	Discussion	55

Contents

4.2	Magneto-transport measurements	67
4.2.1	Anisotropy in films with perpendicular magnetic anisotropy	67
4.2.2	Change of longitudinal resistance	71
5	Investigation of single magnetic nanostructures	79
5.1	Magnetisation behaviour of single magnetic nanostructures	84
5.1.1	Three dimensional switching curve	84
5.1.2	Thiaville method to determine three dimensional switching curves	89
5.1.3	Limits of the measurement technique	92
5.2	Temperature dependence of the anisotropy in single magnetic nanos- tructures	96
5.2.1	Temperature dependence of switching field and superpara- magnetic behaviour	98
5.2.2	Determination of the magnetic moment	101
5.2.3	Determination of anisotropy constants in nanostructures .	104
5.2.4	Field dependent switching times based on Coffey and Kalmykov	109
5.2.5	Comparing film and dot	110
6	Conclusion	113
	Bibliography	119
	Publications	141

1 Introduction

The unstoppable advance of the information age leads to an increasing demand of data storage capacity. Since the development of the first hard disk drive (HDD) in 1956 by IBM [2], magnetic recording has been utilised and constantly researched. The underlying concept of magnetic recording is the storage of data in magnetic domains of granular magnetic media. The bits are defined as the direction of the magnetisation in the domains. Early on, the increase of data storage was hindered by the read heads, that are needed to read out the data. The breakthrough came in 1988, when Fert [3] and Grünberg [4] discovered the giant magneto-resistance that has been first used in 1997.

The cornerstone of today's storage media is the perpendicular magnetic anisotropy (PMA). Based on PMA, perpendicular magnetic recording (PMR) was first proposed by Iwasaki in 1977 [5]. In PMR the magnetisation points perpendicular to the medium unlike the previous used longitudinal recording, where it lies in the plane. Though much higher storage densities can be achieved, it took 28 years until the first hard disk drives utilising PMR hit the market in 2005.

The everlasting increase in storage density is hindered by the superparamagnetic limit [6,7]. Superparamagnetism describes a magnetic state in very small magnetic structures, like the grains used as storage units. At a certain temperature, spontaneous magnetisation reversal will be induced by thermal activation, resulting in a loss of residual magnetisation. The structure behaves like a paramagnet, only with a much stronger magnetisation. The limit is given by :

$$\frac{KV}{k_B T} = 25 \quad (1.1)$$

K stands for the magnetic anisotropy, V describes the volume of the nanostructure, k_B is the Boltzmann constant and T is the temperature. It is evident, that the storage density can not be increased by simply reducing the size of the storage

1 Introduction

units, because eventually the units become superparamagnetic. The problem can be solved by increasing the magnetic anisotropy. However, a higher anisotropy results in a need of stronger magnetic fields to write the data. Such strong magnetic field can not be achieved by the commonly used write heads [6, 8, 9].

This dilemma lead to the development of energy-assisted magnetic recording. One method is the heat-assisted magnetic recording (HAMR) [10]. A laser locally heats the magnetic medium, which lowers the needed magnetic write field. An alternative to HAMR is microwave assisted magnetic recording (MAMR) [11, 12]. Here, a spin-torque oscillator creates an additional magnetic field. A higher anisotropy becomes possible, which allows to reduce the size of the granular storage units and thereby increasing the storage density. As of today, the newest road map by the company Western Digital, shows that neither HAMR nor MAMR HDDs are realised. Instead a new concept simply called energy-assist PMR (ePMR) will be utilised. HAMR and MAMR are not to be released before 2023 [13].

PMA remains an important research topic today, not only due to PMR but also because of the possible application in spin-transfer torque magneto-resistive random access memory (STT-MRAM) [14]. The technique has the advantage of being non-volatile, because the data is stored in magnetic storage elements.

Due to the possible application in data storage media, materials possessing PMA were studied intensively. Gradman et al. fabricated ultra-thin NiFe films on Cu(111) by means of epitaxy and measured PMA as early as 1966 [15]. Starting in 1985, Carcia found PMA in sputtered Co/Pd multilayers [16]. In the following years, PMA was also proven in Co/Pt [17], Co/Au [18], Co/Ru [19] and Co/Ir [20] multilayers. In the group of Prof. Oepen, Co/Pt films have been thoroughly studied [21–27]. A characteristic of sputtered multilayers, is the emergence of intermixing zones due to interdiffusion, which results in the formation of an alloy at the interfaces. Usually the influence of the intermixing zones on the magnetic properties is neglected. However, it will be shown that some properties are affected.

Despite the long history of research, basic properties like the temperature dependence of the anisotropy $K(T)$ are sparsely investigated. The temperature dependence of the anisotropy is well understood in bulk Co, but for the case of ultrathin Co/Pt multilayers, which is needed to create perpendicular magnetic anisotropy, the behaviour is not well understood. First measurements in our group

were made by Kobs [26]. This thesis continues on this investigation.

To further increase the data storage capacity, concepts beyond the energy-assisted magnetic recording are needed. One such concept is bit patterned media (BPM) [28], where nanodots are used as storage units, instead of grains in a magnetic film. The nanodots are made by electron beam lithography and can be compactly arranged, to maximise the storage density. For BPM to work, the switching field distribution needs to be small, so that the bits can be written by the same field strength. To understand if that is possible, the measurement and understanding of single nanodots is desirable.

The magnetisation behaviour of single nanodots is investigated, by using nanosized Hall bar magnetometry. The nanodots are carved out of ultra-thin Co/Pt films by using electron beam lithography and argon ion milling. The emphasis of this thesis lies on the angular dependence of the switching field, as well as the temperature dependence of the anisotropy. Further works in this project were done by A. Neumann [29], C. Thönnißen [30], P. Staeck [1] and E.-S. Wilhelm [31]. Also, results are published in [32].

Chapter 2 discusses the theoretical background and chapter 3 describes the experimental basics. Chapter 4 deals with the temperature dependence of the anisotropy in ultra-thin films. In chapter 5 the magnetisation behaviour of single magnetic nanodots is investigated. Chapter 6 is the conclusion.

2 Theoretical background

In this chapter the theoretical background will be discussed, that is necessary to understand the experimental outcome of this thesis. The main emphasis is put on the magnetic anisotropy and the magnetic behaviour of single domain particles. For further details [33–36] are referenced.

2.1 Basics of magnetism

The fundamental equation to describe magnetism in solid materials is given by:

$$\vec{M} = \bar{\chi} \vec{H} \quad (2.1)$$

\vec{H} is the magnetic field strength vector, $\bar{\chi}$ the magnetic susceptibility tensor and \vec{M} the magnetisation vector. The latter is defined as $\vec{M} = \frac{d\vec{m}}{dV}$, where \vec{m} is the atomic magnetic moment and V is the volume of the solid. The susceptibility $\bar{\chi}$ can be understood as the response of the magnetisation to an external magnetic field. In a case of a linear relation between \vec{H} and \vec{M} , the susceptibility becomes a scalar χ . Depending on sign and magnitude of χ three different classes of magnetic material are defined.

The case $-1 < \chi < 0$ is defined as diamagnetism, where \vec{M} is aligned in the opposite direction of the external field \vec{H} .

The case $0 < \chi < 1$ is defined as paramagnetism. The magnetic moments of the individual atoms are randomly oriented and there is no residual magnetisation. By applying an external magnetic field, the magnetic moments can be aligned in the direction of the magnetic field, resulting in a magnetisation. The magnetisation can be described by a Langevin equation.

The case $\chi \ll 1$ is defined as ferromagnetism. Due to the exchange interaction, the magnetic moments are parallel aligned and build a residual magnetisation, that

2 Theoretical background

exist even without an external magnetic field. To minimise the demagnetisation energy, the ferromagnet builds domains.

2.2 Magnetic energy terms

To describe the magnetic energy E_{Mag} three different contributions are considered. These are the exchange energy E_{Exc} , the magnetostatic energy $E_{\text{M-S}}$, the magnetic anisotropy energy E_{Ani} .

$$E_{\text{Mag}} = E_{\text{Exc}} + E_{\text{M-S}} + E_{\text{Ani}} \quad (2.2)$$

Exchange energy

The exchange interaction describes a quantum mechanical effect, that stems from the interplay of the spin dependent part of the Coulomb interaction and the Pauli principle. It couples neighbouring spins in a manner, that a parallel alignment is favoured. Because of the Pauli principle, the wave function of electrons is anti-symmetric regarding the permutation of two particles. The Hamiltonian H_{Exc} is defined as:

$$H_{\text{Exc}} = -2 \sum_{i < j} J_{ij} \vec{S}_i \cdot \vec{S}_j \quad (2.3)$$

\vec{S}_i and \vec{S}_j are the spin functions of the neighbouring electrons i and j .

Magnetostatic energy

The magnetostatic energy has two contributions: First the Zeeman energy that describes the energy that is induced from an external magnetic field on a ferromagnet and second the demagnetisation energy, which stems from the external stray field that is created in a ferromagnet.

Zeeman energy

The Zeeman energy is given by:

$$E_{\text{Zeeman}} = -\mu_0 \int_V \vec{M} \cdot \vec{H} \, dV \quad (2.4)$$

2.2 Magnetic energy terms

μ_0 is the vacuum permeability given by $4\pi \cdot 10^{-7}$ H/m. When the magnetic field and the magnetisation are homogeneous, therefore independent of V , the formula is simplified by using the vector product:

$$E_{\text{Zeeman}} = -\mu_0 V M_S H \cos(\theta) \quad (2.5)$$

M_S is the saturation magnetisation and θ is the angle between \vec{M} and \vec{H} .

Demagnetisation energy

The demagnetisation energy is the result of the stray field of a ferromagnet. It is a result of the Maxwell equation $\text{div}\vec{B} = \mu_0 \text{div}(\vec{M} + \vec{H}_D) = 0$, which is equivalent to $\text{div}\vec{M} = -\text{div}\vec{H}$. The demagnetisation energy is then given by:

$$E_{\text{Demag}} = -\frac{1}{2} \mu_0 \int_V \vec{M} \cdot \vec{H}_D \, dV \quad (2.6)$$

The demagnetisation energy is easy to calculate for a ellipsoid, where the magnetic field is homogeneous. This can also be approximated for a thin film, which is a limiting case of the ellipsoid. The magnetic field is given by $\vec{H}_D = \vec{N}_D \cdot \vec{M}$. \vec{N}_D is the demagnetisation tensor, that depends on the shape of the sample. In the case of rotational symmetry of the ellipsoid the demagnetisation energy is given by:

$$E_{\text{Demag}} = -\frac{1}{2} \mu_0 M_S^2 V (N_{\parallel} \sin^2(\theta) + N_{\perp} \cos^2(\theta)) \quad (2.7)$$

Here, θ is the angle between the magnetisation and the rotational axis and N_{\parallel} and N_{\perp} are the parallel and perpendicular contributions of the demagnetisation tensor.

The demagnetisation energy depends on the direction of the magnetisation. In a thin film this is described by:

$$E_{\text{Demag}} = -\frac{1}{2} \mu_0 M_S^2 V \cos^2(\theta) \quad (2.8)$$

θ is the angle between magnetisation and film plane. The demagnetisation energy is at a maximum for $\theta = 90^\circ$ and at minimum for $\theta = 0^\circ$, which means the magnetisation is favoured to lie in the film plane. The difference in energy density is called shape anisotropy $K_{\text{shape}} = \frac{E(\theta=0^\circ) - E(\theta=90^\circ)}{V}$.

2 Theoretical background

Shape anisotropy

The shape anisotropy of a magnetic film lies parallel to the film plane and is given by:

$$K_{\text{shape, film}} = -\frac{1}{2} \mu_0 M_S^2 \quad (2.9)$$

Besides magnetic films, lithographically made nanodots are a main topic in this thesis. To describe the shape anisotropy of nanodots an expression for cylinders derived by Millev et al. [37] is used:

$$K_{\text{shape, dot}} = -\frac{1}{2} \mu_0 M_S^2 \left(1 + \frac{2}{\pi} \kappa - \frac{3}{2} \frac{1}{\sqrt{1 + \kappa^2}} \cdot {}_2F_1 \left(\frac{5}{2}; \frac{1}{2}; 2; \frac{\kappa^2}{1 + \kappa^2} \right) \right) \quad (2.10)$$

$\kappa = d/t$ is the the aspect ratio between the diameter d of the cylinder and the thickness t of the magnetic layer. ${}_2F_1$ is the Gaussian hypergeometric function. When performing nanostructuring of a magnetic film into a nanodot the shape anisotropy changes by a value of $\Delta K_{\text{shape}} = K_{\text{shape, dot}} - K_{\text{shape, film}}$.

Magnetic anisotropy

In a solid certain directions of the magnetisation are preferred, called easy axes of magnetisation. Energetically unfavourable directions are called hard axes of magnetisation. The magnetic anisotropy is defined as the difference in energy density between the easy axis and the hard axis of magnetisation. This anisotropy is caused by a multitude of physical effects, the main contributions being the magneto-crystalline anisotropy, interface anisotropy and strain anisotropy.

Magneto-crystalline anisotropy

The magneto-crystalline anisotropy is caused by the spin-orbit interaction that couples the magnetic moments of the atoms to the crystal lattice of the solid. The easy axes of magnetisation are equal to certain crystal axes, depending on the crystal lattice. For hcp Cobalt the easy axis is the 001-direction of the lattice. Such a system with one preferred direction is called a uniaxial anisotropy and is described by

$$E_{\text{uni}}/V = K_1 \sin^2(\theta) + K_2 \sin^4(\theta) + \mathcal{O}(\sin^6(\theta)) \quad (2.11)$$

2.2 Magnetic energy terms

K_1 and K_2 are the anisotropy constants in first and second order, V is the volume of the system and θ is the angle between the easy axis and the magnetisation.

In cubic crystals another anisotropy occurs, the cubic anisotropy. The energy density can be expressed by using the direction cosines of the magnetisation α_1, α_2 and α_3 . The energy density is given by:

$$E_{\text{cubic}}/V = K_{\text{cub},1} (\alpha_1^2 \alpha_2^2 + \alpha_2^2 \alpha_3^2 + \alpha_3^2 \alpha_1^2) + K_{\text{cub},2} \alpha_1^2 \alpha_2^2 \alpha_3^2 \quad (2.12)$$

$K_{\text{cub},1}$ and $K_{\text{cub},2}$ are the cubic anisotropy constant of the first and second order. Higher orders are neglected.

Interface anisotropy

On surfaces or interfaces of thin films the translation symmetry is broken. This leads to another contribution of the anisotropy, which causes an easy axis of magnetisation perpendicular to the film plane. This interface or surface anisotropy is described by:

$$E_S/V = \frac{2K_{\text{Int}}}{t} \sin^2(\theta) \quad (2.13)$$

t is the thickness of the film and the factor 2 stems from the fact, that there are usually two interfaces. E_{Int} decreases with higher film thickness and plays an important part for the magnetism in thin films.

Magneto-elastic energy

In this chapter the magneto-elastic energy is discussed. Any elongation or compression of a crystal results in a change of the magnetisation, because the latter is connected to the crystal by spin-orbit coupling. This results in another anisotropy term, known as strain anisotropy. The magneto-elastic energy has been extensively studied by Sander et al. [38–41]. Though Co can grow in hcp as well as fcc structure, only the magneto-elastic energy of fcc Co is important in this thesis. The energy density is given by Kittel [42] or Lee [43]:

$$E_{\text{ME,fcc}}/V = B_1 (\epsilon_1 \alpha_1^2 + \epsilon_2 \alpha_2^2 + \epsilon_3 \alpha_3^2) + B_2 (\epsilon_4 \alpha_2 \alpha_3 + \epsilon_5 \alpha_3 \alpha_1 + \epsilon_6 \alpha_1 \alpha_2) \quad (2.14)$$

ϵ_i is the elastic strain tensor, B_i are the magneto-elastic coupling constants and α_i are the direction cosines. The equation is restricted to the first and second

2 Theoretical background

order. Higher orders are discussed by Becker and Döring [44] and Carr [45], but are neglected in this thesis. The magneto-elastic coupling constants are given by:

$$B_1 = -\frac{3}{2}(c_{11} - c_{12})\lambda_{100} \quad (2.15)$$

$$B_2 = -3c_{44}\lambda_{111} \quad (2.16)$$

c_{ij} are the elastic stiffness constants and λ the magneto-strictive strain constants. The numbers of the constants are tabulated in [40] by Sander. It follows for fcc Co: $c_{11} = 242$ GPa, $c_{12} = 160$ GPa, $c_{44} = 128$ GPa, $\lambda_{100} = 75 \cdot 10^{-6}$, $\lambda_{111} = -20 \cdot 10^{-6}$, $B_1 = -9.2$ MJ/m³ and $B_2 = 7.7$ MJ/m³. The magnetic anisotropy is defined as the difference in energy density between the easy axis of magnetisation and the hard axis. For the films investigated in this thesis, this is the difference between a magnetisation pointing in the film plane and pointing parallel to the film normal. For a fcc crystal with a (111) texture this results in:

$$K_{ME} = B_2(\epsilon_{ip} - \epsilon_{oop}) \quad (2.17)$$

ϵ_{ip} is the in plane strain and ϵ_{oop} the out of plane strain. They are connected by the elastic stiffness constants. Sander [40] gives the following relation:

$$\epsilon_{oop} = -\frac{c_{11} + 2c_{12} - c_{44}}{c_{11} + 2c_{11} + 4c_{11}} 2\epsilon_{ip} \quad (2.18)$$

This results in $\epsilon_{oop} = -0.57\epsilon_{ip}$, hence:

$$K_{ME} = B_2 \cdot 1.57 \epsilon_{ip} \quad (2.19)$$

Effective anisotropy

The above mentioned anisotropy terms can be summed up to an effective anisotropy:

$$K_{Eff} = K_{MC} + K_{Shape} + \frac{2K_{Int}}{t} + K_{ME} = K_{V,eff} + \frac{2K_{Int}}{t} \quad (2.20)$$

Depending on the film thickness the effective anisotropy might lie in the plane of the film (in-plane anisotropy) or perpendicular to the film plane (out-of-plane anisotropy). Usually, a negative sign is given to the in-plane contribution of the

anisotropy and a positive sign to the out-of-plane contribution. The transition from out-of-plane to in-plane anisotropy is called spin reorientation transition (SRT). K_{MC} and K_{ME} can be understood as the volume anisotropy $K_V = K_{MC} + K_{ME}$. Volume anisotropy and shape anisotropy give the effective volume anisotropy $K_{V,eff} = K_V + K_{shape}$.

2.3 Single domain systems

Two effects act on the magnetic moments in a solid. The exchange interaction favours the magnetic moments to align parallel to another. However, the demagnetisation energy favours an anti-parallel alignment, which minimises the stray field. The interplay of both effect results in the emergence of domains. That are regions within the solid, where the magnetic moments are aligned parallel. The domains themselves are not parallel to another. Typical domain state structures are stripe domain or Landau domain structures. The transition region between two domains is called domain wall. The width of the domain walls is determined by the exchange interaction and the magnetic anisotropy. The exchange favours only a small rotation of each individual magnetic moment, to hinder a strong deviation from the parallel alignment. The anisotropy favours a large rotation in the hard axis of magnetisation. For a Bloch wall the width is given by $\delta_0(K_{eff}) = \pi\sqrt{\frac{A_{ex}}{K_{eff}}}$ [46]. $A_{ex} = 31.4 \text{ pJ/m}^3$ is the exchange constant of Co. Depending on the anisotropy one can find typical domain wall width of $\delta_0(100 \text{ kJ/m}^3) = 56 \text{ nm}$ and $\delta_0(300 \text{ kJ/m}^3) = 32 \text{ nm}$.

Reducing the size of a magnetic structure will at a certain point result in a single domain state. It is then energetically unfavourable to create domains. Depending on the size of the structure, different types of magnetisation reversal exist. For this thesis most important is the model of coherent rotation, also known as Stoner-Wohlfarth model. Magnetisation reversal by coherent rotation means, that all magnetic moments of the structure rotate uniformly from one state to the other like a single macrospin. Increasing the size of the structure will lead to another form of magnetisation reversal called domain wall nucleation. In this case a domain in the opposite magnetisation state will be created and grow in size until the whole structure has changed its state. The critical diameter for coherent rotation in a cylindrical nanostructure has been given by Skomski [47]

2 Theoretical background

as $D(t) \approx 23 \frac{l_0^2}{t}$. The variable t defines the thickness of the magnetic material. $l_0 = \sqrt{\frac{2A_{\text{ex}}}{\mu_0 M_S^2}} = 4.8 \text{ nm}$ [46] is the magnetostatic exchange interaction length, with $M_S(0 \text{ K}) = 1.458 \text{ MA/m}$ [48] as the saturation magnetisation. Typical diameters are $D(0.7 \text{ nm}) = 757 \text{ nm}$ and $D(1 \text{ nm}) = 529 \text{ nm}$. The nanostructures that are investigated are between 16 nm and 45 nm in diameter. Therefore, coherent rotation is expected, which will be discussed in the next section.

2.3.1 Stoner-Wohlfarth model

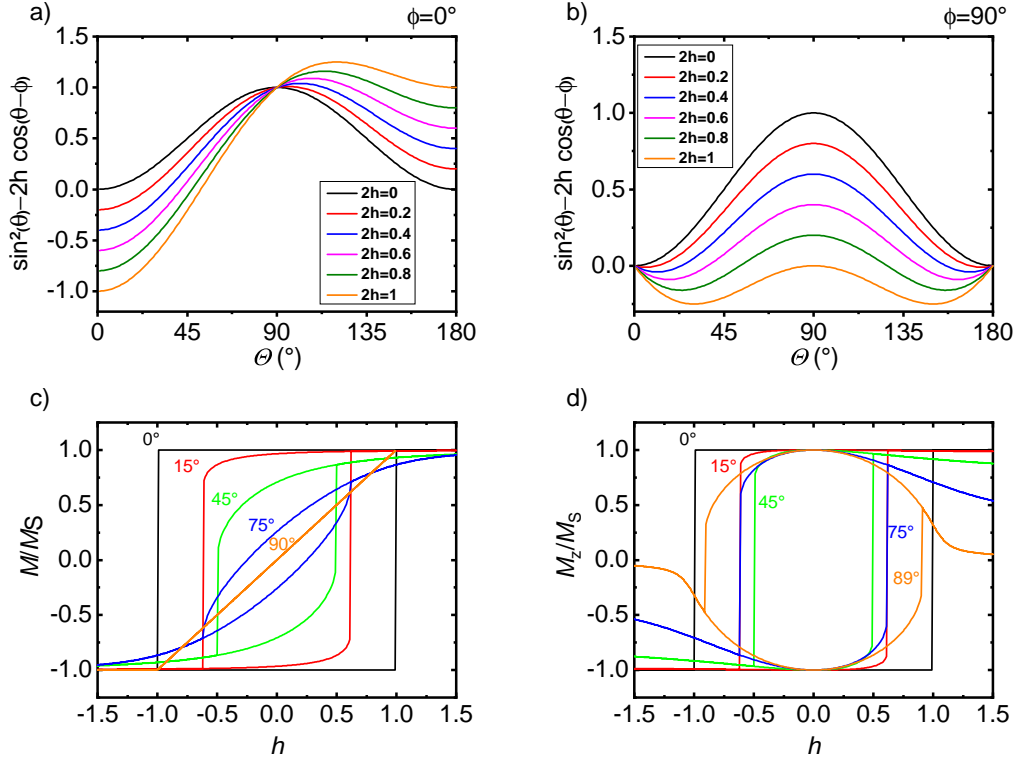


Figure 2.1: a) shows the uniaxial energy potential with a magnetic field applied in the easy axis of magnetisation. h is the reduced field H/H_K . The different colors represent the different field strength. For $h = 0$ two minima can be seen, that represent the two states of magnetisation. They are separated by the energy barrier. When a magnetic field is applied the energy potential is altered. When the minimum disappears, the magnetisation is reversed.

b) shows the case when the magnetic field is applied in the hard axis of magnetisation. With increasing field, the energy barrier shrinks and the minima converge to another. Eventually only one minimum remains.

c) shows the hysteresis curves of the magnetisation M/M_S in dependence of h for varying angles ϕ . At $\phi = 0^\circ$ a rectangular hysteresis curve emerges. Moving closer to 90° will result in a closing of the hysteresis.

d) shows the perpendicular projection of the magnetisation M_z/M_S . At 0° the hysteresis curve is rectangular and gets consequently rounder in shape, when moving to 90° . The two plateaus are the two states of magnetisation. When the switching field H_{Sw} is reached, the magnetisation is reversed, which is seen as a jump in the hysteresis. The switching field is dependent of ϕ .

The model of coherent rotation was developed by Stoner and Wohlfarth and published in 1948 [49] and republished in 1991 [50]. A review is found in [51]. The

2 Theoretical background

model is based on an uniaxial anisotropy potential, that is effected by an external magnetic field, which is described by a Zeemann-term. The energy density is given by:

$$E_{\text{SW}}/V = K \sin^2(\theta) - \mu_0 H M_S \cos(\theta - \phi) \quad (2.21)$$

ϕ describes the angle between the easy axis of magnetisation and the external magnetic field. Of particular interest are the cases of the applied magnetic field parallel to the easy axis of magnetisation ($\phi = 0^\circ$, see fig. 2.21 a)) and perpendicular to the easy axis ($\phi = 90^\circ$, see fig. 2.21 b)). The magnetic field is displayed as the reduced field $h = H/H_K$. The latter is the critical field, which is given by $H_K = \frac{2K}{\mu_0 M_S}$.

In the first case, the deformation of the energy landscape with increasing magnetic field, will manifest in the vanishing of one of the minima and the state parallel to the magnetic field will be preferred. In the second case the energy barrier between the two minima will shrink and the two minima will converge until at a certain field, the energy barrier disappears and only one minimum remains. The energy barrier is defined as the product of anisotropy and volume of the structure: $\Delta E = KV$. It is dependent on the magnetic field and is given by:

$$\Delta E = KV \left(1 - \frac{H}{H_K}\right)^{n(\phi)} \quad (2.22)$$

Pfeiffer [52] gave an approximation of the exponent, which is $n(\phi) = 0.86 + 1.14 \cdot H_{\text{Sw}}(\phi)$. In the easy and hard axis of magnetisation $n = 2$.

In the experiment, usually magnetic field sweeps are performed. Fig. 2.21 c) shows the magnetisation M/M_S in dependence of the reduced field. These curves are called hysteresis curves. Different angles ϕ are displayed. At $\phi = 0^\circ$ the curve has a rectangular form. Moving to $\phi = 90^\circ$, the hysteresis begins to close. The coercive field at $\phi = 0^\circ$ and 90° is identical to the critical field H_K . The measurement technique, that is used in this thesis, is only sensitive to the perpendicular component of the magnetisation M_z . Fig. 2.21 d) shows hysteresis curves of $M_z/M_S(h)$. The hysteresis does not close, when approaching $\phi = 90^\circ$, but becomes circular. The two plateaus seen in the graph are the two states of magnetisation. Once the magnetic field strength reaches the switching field H_{Sw} , the magnetisation is reversed. The magnetisation reversal is represented by a jump in the hysteresis curve. The switching field $H_{\text{Sw}}(\phi)$ is depending on the

2.3 Single domain systems

angle between the magnetic field and the easy axis of magnetisation.

The angular dependence of the switching field is determined by deriving the local minimum of the energy landscape in dependence of θ and is given by:

$$H_{\text{Sw}}(\theta) = \frac{2K}{\mu_0 M_S} \left(\sin^{\frac{2}{3}}(\theta) + \cos^{\frac{2}{3}}(\theta) \right)^{-\frac{3}{2}} \quad (2.23)$$

$H_{\text{Sw}}/H_K(\phi)$ is plotted in fig. 2.2 a). The black line shows the angular dependence of the switching field given by the Stoner-Wohlfarth model. The switching field is at maximum in the easy axis ($\phi = 0^\circ$) and the hard axis of magnetisation (90° and -90°). The curve is symmetric to 45° and -45° , where there is a minimum. The red line shows an extension of the model, that was proposed by Kronmüller [53]. The extension adds the second order of the anisotropy K_2 and is given by:

$$H_{\text{Sw,Kronm.}} = H_{\text{Sw}} \left(1 + \frac{2K_2}{K_1} \frac{(-\tan(\phi))^{\frac{2}{3}}}{1 + (-\tan(\phi))^{\frac{2}{3}}} \right) \quad (2.24)$$

The equation is valid for $K_2/K_1 \ll 1$. In the plot a ratio $K_2/K_1 = 0.25$ is chosen, that is in alignment to the experiment. The second order of the anisotropy increases the switching field in the hard axis of magnetisation. The easy axis remains unchanged and the local minima stay at 45° . Chang [54] also investigated the second order and gave an analytical solution. His findings in the case of $K_1 > 0$ and $K_2 > 0$ and $K_2/K_1 \ll 1$ are in close resemblance to the solution given by Kronmüller [29]. Another way of displaying the angular dependence of the switching field is the Stoner-Wohlfarth astroid, where the switching field is separated into the perpendicular and parallel contribution (see fig. 2.2 b)). In order to understand the three dimensional angular dependence of H_{Sw} , the astroid can be rotated around the ordinate. The two dimensional astroid can be understood as a slice, that is cut out of the three dimensional surface. Fig. 2.3 shows the three dimensional switching surface of the Stoner-Wohlfarth model. The switching surface is defined by certain characteristics. There is a distinct easy axis point, that is expressed by a sharp peak in the direction of the easy axis of magnetisation. The hard plane of magnetisation has a circular shape.

The angular dependence of the switching field is good indicator for the reversal mode of the investigated nanostructure. Next to coherent rotation, also domain wall nucleation is possible in single domain systems, which leads to a different

2 Theoretical background

angular dependence. This will be briefly explained in the next section.

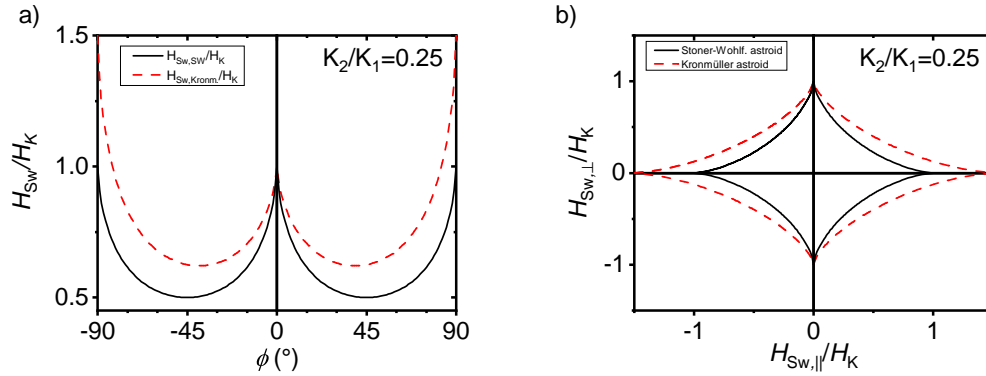


Figure 2.2: a) The plot displays the angular dependence of the switching field. The black line shows the Stoner-Wohlfarth model. H_{Sw} peaks in the easy and hard axis of magnetisation and is axis symmetric. Also there is a symmetry around 45° . The red line represents an extension of the model made by Kronmüller, that takes the second order of the anisotropy into account. This results in an increase of h_{Sw} in the hard axis. b) is an alternative form of presentation, that is called the Stoner-Wohlfarth astroid. H_{Sw} is separated into the perpendicular and parallel contributions. The red line shows again the extension of Kronmüller. The astroid can be understood as a slice of the three dimensional switching surface. The latter can be created by rotating the astroid around the ordinate.

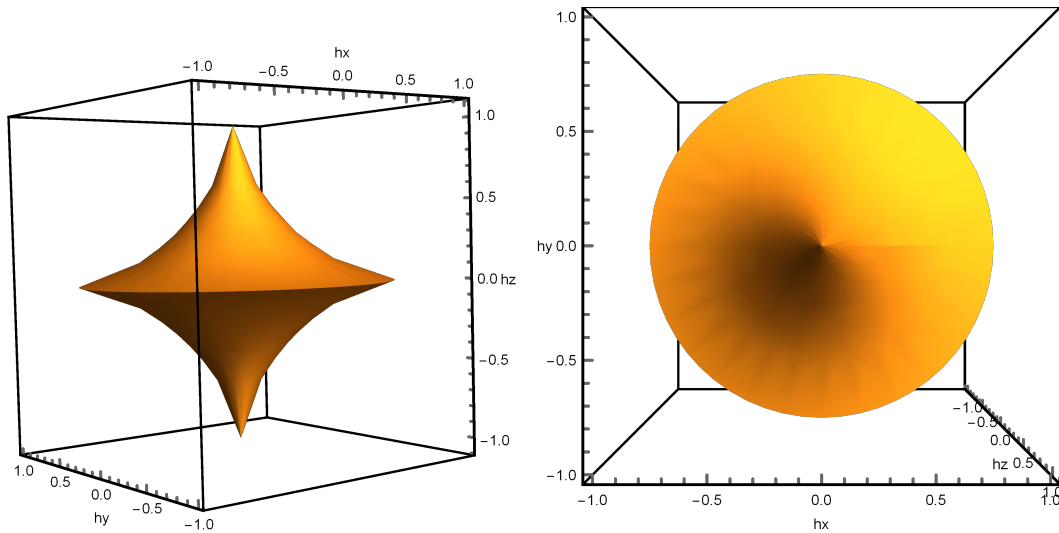


Figure 2.3: The three dimensional switching surface of the Stoner-Wohlfarth model is presented. On the left side, a viewpoint from the side is shown. The surface has a distinct easy axis point. On the right side, a viewpoint from the top is seen. The hard plane of magnetisation has a circular shape.

2.3.2 Domain wall nucleation

The model to describe domain wall nucleation in a single domain nanostructure was published by Kondorsky in 1940 [55]. In this case, the magnetic moments will not rotate like a macrospin. Instead a nucleus of the reversed magnetisation state will form somewhere in the nanostructure. This reversed domain will grow and the domain wall will move through the sample until the whole magnetisation is reversed. Due to the time scale of the process, in experiment domain wall nucleation can not be distinguished from coherent rotation by looking at the hysteresis curve. Instead one can measure the angular dependence of the switching field. While for coherent rotation the angular dependence is given by eq. 2.23. For domain wall nucleation the angular dependence is proportional to $1/\cos(\theta)$.

2.4 Thermal effects

In single domain structures an effect called superparamagnetism emerges above a certain temperature. The temperature is called blocking temperature T_B . Once the thermal energy $k_B T$ becomes comparable in size to the energy barrier KV spontaneous magnetisation reversal will occur. A common definition for the blocking temperature is given by $KV = 25k_B T$. Superparamagnetism displays the same characteristics as paramagnetism, albeit with a much higher magnetisation. The average time between two magnetisation reversals, called switching frequency, is given by the following equation, which was developed by Néel based on an Arrhenius ansatz and is therefore known as Néel-Arrhenius law [56]

$$f = f_0 \exp\left(-\frac{KV}{k_B T}\right) \quad (2.25)$$

f_0 is the exponential prefactor. After Néel, Brown took on the problem and found a solution based on the magnetisation dynamics [57, 58]. The magnetisation dynamics is described by the Landau-Lifschitz-Gilbert equation (LLG). Using the LLG as a basis, Brown derived the switching frequency, which is always given by the form of $f = f_0 \exp\left(-\frac{\Delta E}{k_B T}\right)$. Hence the equation is also known as Néel-Brown law. In the case of a large energy barrier $\Delta E \gg k_B T$ and a magnetic field applied

2 Theoretical background

along the easy axis of magnetisation the following rate equation is derived:

$$f_{\pm} = f_{0,\pm} \exp\left(-\frac{\Delta E}{k_B T}\right) = f_{0,\pm} \exp\left(-\frac{KV}{k_B T} (1 \pm h)^2\right) \quad (2.26)$$

'+' describes the change of magnetisation orientation from the energetically preferred minimum into the metastable minimum, while '-' describes the opposite case. The attempt frequency $f_{0,\pm}(h, T)$ is given by Brown as:

$$f_{0,\pm}(h, T) = \frac{\alpha\gamma}{1 + \alpha^2} \cdot \sqrt{\frac{(\mu_0 H_K)^2 M_S V}{2\pi k_B T}} \cdot (1 \pm h) \cdot (1 - h)^2 \quad (2.27)$$

γ is the gyromagnetic ratio, α is the damping parameter of the material and H_K is the anisotropy field, which is given by $H_K = \frac{2K}{\mu_0 M_S}$. Usual values of the attempt frequency f_0 are in the range of 10^9 Hz and 10^{11} Hz. The pre-factor plays a prominent role in this thesis and will be discussed later on in the experimental section.

Spontaneous magnetisation behaviour with an applied magnetic field

Coffey and Kalmykov [59] calculated the effect of an applied magnetic field on the attempt frequency $f_0 = 1/\tau_0$. The magnetic field is applied in the hard axis of magnetisation. They looked at two specific cases, that depend on the damping parameter α . The two cases are called very low damping (VLD) for $\alpha \ll 1$ and intermediate high damping (IHD) for $\alpha > 1$. For the VLD case the following equation is found, where $\sigma = \frac{KV}{k_B T}$ and $h = H/H_K$ $\beta = \frac{V}{k_B T}$.

$$1/f_{\text{VLD}}(h, T) = \frac{\pi \cdot \left[1 - \frac{13}{6}h + \frac{11}{8}h^2 - \frac{3}{16}h^3 + \mathcal{O}(h^4)\right]}{8\sigma^2 \cdot \sqrt{h(1-h)^2}} \exp\left(\sigma(1-h)^2\right) \quad (2.28)$$

With $\tau_N = \frac{M_S V}{k_B T} \cdot \frac{(1+\alpha^2)}{2\gamma\alpha}$, the IHD case is given by:

$$1/f_{\text{IHD}}(h, T) = \frac{2\tau_N \pi \sqrt{h}}{\sigma \sqrt{1+h} \cdot (1-2h + \sqrt{1+4h(1-h)\alpha^{-2}})} \exp\left(\sigma(1-h)^2\right) \quad (2.29)$$

The exponential term of both functions is identical to the Néel-Arrhenius law. The frontal terms can be understood as field dependent attempt frequencies $f_{0,\text{VLD}}(h)$

and $f_{0,\text{IHD}}(h)$.

Temperature dependence of the switching field

Below T_B , thermal energy also effects the switching field of single domain structures. The magnetisation may be reversed before the local minimum in the energy potential disappears, due to thermal activation. The switching field is thus smaller than in the case of the Stoner-Wohlfarth model. Different models for $H_{\text{Sw}}(T)$ have been compared by Neumann [29]. He finds that the solution given by Garg [60] describes the switching field best:

$$H_{\text{Sw}}(T) = \frac{2K}{\mu_0 M_S} \left(1 - \left[1 + \frac{\gamma_{\text{EM}}}{2 \ln \left(\frac{k_B T f_0}{\mu_0 M_S V} \frac{1}{R} \right)} \right] \sqrt{\frac{k_B T}{KV} \ln \left(\frac{k_B T f_0}{\mu_0 M_S V} \frac{1}{R} \right)} \right) \quad (2.30)$$

$\gamma_{\text{EM}} = 0.5772$ is the Euler-Mascheroni constant. R is the sweeping rate of the magnetic field. In the experiment usually 0.01 T/s is used.

2.5 Magnetotransport effects

In general, electric resistivity is described by Ohm's law, which connects the current density \vec{j} and the electric field \vec{E} by the electrical conductivity tensor $\bar{\sigma}$.

$$\vec{j} = \bar{\sigma} \cdot \vec{E} \quad (2.31)$$

The inverse of the conductivity tensor is the resistivity tensor $\bar{\rho} = \bar{\sigma}^{-1}$. In a classical sense, Ohm's law can be derived by the Drude model. In the Drude model, the metal consists of positively charged ions while the electrons are treated like a classic gas. The electrons, that move with a constant velocity, are permanently colliding with the ions, with an average collision time τ . The conductivity, that is a scalar in the model, is given by $\sigma = \frac{e^2 n \tau}{m_e}$. n is the electron density and m_e the electron mass.

Non-classical Ohm's law can be derived by solving the Boltzmann equation. The mean collision time τ_{col} is given by $\tau_{\text{col}} = \lambda/v_F$. The latter is the Fermi velocity $v_F = \sqrt{2E_F/m_e}$, where E_F is the Fermie energy. λ is the mean free path, which is typically 10 – 100 nm at room temperature.

τ depends on the different scattering processes. The electron can scatter on lattice,

2 Theoretical background

interfaces, as well as phonons, and magnons. As the electron-phonon as well as the electron-magnon scattering is temperature dependent, so is τ . The different processes are connected by Matthiesens's rule, which is given by:

$$\frac{1}{\tau_{\text{col}}} = \frac{1}{\tau_{\text{defects}}} + \frac{1}{\tau_{\text{int}}} + \frac{1}{\tau_{\text{ph}}(T)} + \frac{1}{\tau_{\text{magn}}(T)} \quad (2.32)$$

Usually, only scattering on lattice defects and phonons are take into consideration. Scattering at interfaces is only important in ultrathin films and the contribution of electron-magnon scattering is small compared to electron-phonon scattering. The temperature dependence of the specific resistivity is decided by the temperature dependence of the electron-phonon scattering, which is given by the Bloch-Grüneisen formula:

$$\rho = \rho_0 + \rho(T) = \rho_0 + A \left(\frac{T}{\Theta_D} \right) \int_0^{\Theta_D/T} \frac{x^5 dx}{(e^x - 1)(1 - e^{-x})} \quad (2.33)$$

A is a material constant and Θ_D is the Debye temperature.

2.5.1 Longitudinal magnetoresistance effects

A magnetic field applied to an electrical conductor will lead to a change in resistivity of the conductor, which is known as magnetotransport. In a ferromagnet, like the Pt/Co/Pt samples investigated in this thesis, additionally to the magnetic field \vec{H} the magnetisation \vec{M} has to be considered, thus leading to a resistivity tensor $\vec{\rho}(\vec{H}, \vec{M})$. The latter is connected to the electrical field \vec{E} and the electrical current \vec{j} by Ohm's law:

$$\vec{E} = \vec{\rho}(\vec{H}, \vec{M}) \cdot \vec{j} \quad (2.34)$$

In this thesis the current is applied in the xy-plane of the film, which leaves two resistivity contributions ρ_x and ρ_y . The former is the longitudinal resistivity (the resistance along the current direction \vec{j}) and the latter is the transversal resistivity (the resistance perpendicular to the current direction).

The longitudinal magnetoresistance effects are defined by Onsager's law as even functions of the resistivity: $\rho_x(\vec{H}, \vec{M}) = \rho_x(-\vec{H}, -\vec{M})$. In this thesis the following magnetoresistance (MR) effects are discussed: Anisotropic MR, anisotropic interface MR, geometrical size effect, Lorentz MR and Spin disorder MR.

Anisotropic magnetoresistance

The anisotropic magnetoresistance (AMR) occurs in ferromagnetic materials and was discovered by W. Thompson in 1856 [61]. As a consequence of the AMR, the resistance is depending on the angle Φ between magnetisation and the applied electric current $\Phi \angle(\vec{M}, \vec{j})$. Models describing the AMR are based on an anisotropy in the spin orbit interaction [62–65]. Usually, the resistivity is larger in the longitudinal case of ρ_{long} with $\Phi = 0^\circ$ than for the transversal case of ρ_{trans} with $\Phi = 90^\circ$. The magnitude of the AMR is usually defined by $\Delta\rho_{\text{AMR}} = \rho_{\text{long}} - \rho_{\text{trans}} > 0$. In the case of technical saturation $M = M_S$, the angular dependence of the AMR is given by

$$\rho(\Phi) = \rho_{\text{trans}} + \Delta\rho_{\text{AMR}} \cos^2(\Phi) \quad (2.35)$$

Kobs and Oepen [66] showed that the AMR in Co/Pt multilayers depends on the thickness of the Co layer, because of an additional AMR contribution that stems from the interfaces. The overall magnitude of the AMR is thus determined by the ratio of interface to bulk.

Anisotropic interface magnetoresistance and geometrical size effect

In 2010 Kobs et al. [67] found a new effect in ultrathin multilayers, which was called anisotropic interface magneto resistance (AIMR). This effect behaves similar to the AMR though it depends on the angle between magnetisation and film normal $\Theta \angle(\vec{M}, \vec{n})$. The magnitude of the AIMR is given by the difference between the polar case $\rho(\Theta = 0^\circ) = \rho_{\text{polar}}$ and the transversal case $\rho(\Theta = 90^\circ) = \rho_{\text{trans}}$, hence $\Delta\rho_{\text{AIMR}} = \rho_{\text{polar}} - \rho_{\text{trans}}$. In textured films, the angle dependence is nearly identical to the AMR albeit higher orders can be observed especially for Co/Ni multilayers and to a lesser extent in Co/Pt multilayers:

$$\rho = \rho_{\text{trans}} + \Delta\rho_{\text{AIMR}} (\cos^2(\Theta) + \cos^4(\Theta) + \cos^6(\Theta)) \quad (2.36)$$

Phenomenology the effect can be explained with magnetisation-dependent scattering probabilities of the electrons on interfaces [66]. Weinberger developed a fully relativistic model, that includes spin-orbit interaction. The AIMR is only detectable in thin films, where the magnetic layer is less than 50 nm [68].

2 Theoretical background

The geometrical size effect (GSE) was discovered in 2005 by Gil et al. [69]. The GSE stems from magnetisation dependent scattering probability in respect to the texture of the film. In Pt/Co/Pt film systems the GSE occurs in the same geometry as the AIMR and is thus superimposed with the latter. It has a negative sign and, because it is a bulk effect, is independent of the thickness. Therefore the GSE serves as a constant negative offset to the AIMR in Co/Pt films [67].

Lorentz magnetoresistance

The Lorentz magneto-resistance (LMR) is an anisotropic effect that manifest as an increase of the resistivity above technical saturation, where the magnetisation is aligned parallel to the magnetic field. The LMR is a result of the Lorentz force. An external magnetic field that is applied transversal to the current direction forces the electrons on helical orbits, which reduces the effective mean free path in the current direction. The strength of the LMR goes quadratic with the applied magnetic field [70]:

$$\rho_{\text{LMR}} \propto B^2 \quad (2.37)$$

The LMR also occurs when the magnetic field is applied in the direction of the electric current, though the magnitude of the effect is smaller [71].

Spin-disorder magnetoresistance

The saturation magnetisation M_S is temperature dependent, which will become an important aspect in later parts of this thesis. At higher temperatures the temperature dependence can be described by Bloch's $T^{3/2}$ law [72]:

$$M_S(T) = M_S(0 \text{ K})(1 - bT^{3/2}) \quad (2.38)$$

b is the Bloch constant, which is a constant, that depends on the exchange stiffness A and the lattice constant a of the material. Stearns gives $b = 1.5 \cdot 10^{-6} \text{ K}^{-3/2}$ [73] for hcp Co above 100 K. Whereas Liu et. al give $b = 3.3 \cdot 10^{-6} \text{ K}^{-3/2}$ [74] for bulk Co. In Co nanoparticles or nanostructures [75–77] the Bloch constant might deviate from this values, because of surface effects. This might lead to a higher temperature dependence of the saturation magnetisation.

When applying a magnetic field spin-waves (or magnons) are reduced. This

2.5 Magnetotransport effects

reduction of magnon density leads to a decrease in magnon-electron scattering, whereby the resistance will decrease. This effect is known as spin-disorder magneto resistance (SMR). The SMR is an isotropic effect that exhibits a linear dependence of the resistance in respect to the magnetic field [78]:

$$\rho_{\text{LMR}} \propto -|B| \quad (2.39)$$

At very low temperatures the SMR deviates from the linear behaviour. A change in sign is observed and the resistance is increasing with the field [79]. Though this could also be the result of the LMR, when all magnons are annihilated and magnon-electron scattering (and thus the SMR) completely vanishes.

2.5.2 Transversal magnetoresistance effect

Normal and anomalous Hall effect

When a magnetic field $\mu_0 H_Z$ is applied perpendicular to an electric current a voltage will emerge, that is perpendicular to the field and the current. This effect was discovered in 1879 by Edwin Hall and named Hall effect [80, 81]. The Hall effect is caused by the Lorentz force, which deflects the conducting electrons perpendicular to the field and current direction j_X . The emerging voltage is known as Hall voltage U_{Hall} and is described by:

$$U_{\text{Hall}} = R_{\text{NHE}} \frac{I_X \mu_0 H_Z}{t} \quad (2.40)$$

t is the thickness of the material and R_{NHE} is the Hall constant, which is a material parameter.

In 1880 Hall discovered the anomalous Hall effect [82, 83], that emerges only in ferromagnetic material, which possess a spontaneous Magnetisation M_S , e.g. Fe, Co and Ni. This effect is caused by Spin-Orbit interaction, which results in spin dependent scattering probabilities. Phenomenologically, normal and anomalous Hall effect are described by:

$$U_{\text{Hall}} = \mu_0 (R_{\text{NHE}} H_Z + R_{\text{AHE}} M_Z) I_X / t \quad (2.41)$$

2 Theoretical background

R_{AHE} is the anomalous Hall constant. The anomalous Hall effect is often by orders of magnitude higher than the normal Hall effect. For the materials used in this thesis, cobalt and platinum, the following values are found in literature. The normal Hall constant in cobalt and platinum are $R_{\text{NHE,Co}} = -1.1 \cdot 10^{-10} \text{ m}^3/\text{C}$ and $R_{\text{NHE,Pt}} = -2,3 \cdot 10^{-11} \text{ m}^3/\text{C}$, while the anomalous Hall constant of Co is given as $(1.2 - 2) \cdot 10^{-9} \text{ m}^3/\text{C}$ [84].

3 Sample preparation and experimental details

In this chapter the sample preparation and experimental details are discussed. The main emphasis will lie on the Pt/Co/Pt system that is investigated in this thesis. Also the lithography and nano-structuring that was performed to create the Hall bars and nanodots will be explained. An expansion of the measurement principle will be shown with the idea to measure magneto-resistance effects in nanodots. Furthermore different nanodot lattices will be shown, that were created for investigations with synchrotron radiation.

3.1 Pt/Co/Pt sample system

In this thesis measurements of ultra-thin Pt/Co/Pt films and nanostructures have been performed. The films have been investigated in the group of Prof. Oepen over the past two decades [21–27]. The samples are created by electron cycle resonance (ECR) sputtering and direct current (DC) magnetron sputtering. Starting with a SiO₂ or Si₃N₄ substrate a Pt seed layer is evaporated by ECR sputtering, which induces a good texture. Afterwards another layer of Pt is evaporated by DC magnetron sputtering. This is followed by the Co layer and a Pt cap layer, both of them also made by DC magnetron sputtering. The two interfaces between the Co and Pt layers ensure a strong uniaxial anisotropy, that is perpendicular to the film plane for thin Co layers. Typical layer thicknesses are (4 + 1) nm or (4 + 3) nm for the Pt seed layer and 3 nm for the Pt cap layer. The Co thickness is varied from 0.7 nm to 30 nm, whereby the system will undergo a spin reorientation transition between 1.2 nm and 1.5 nm, depending on the substrate.

Prior investigations [26,27] insist that the Co layer will grow in a fcc-structure and is strained at thin Co thickness, because of different lattice parameters of Pt and

3 Sample preparation and experimental details

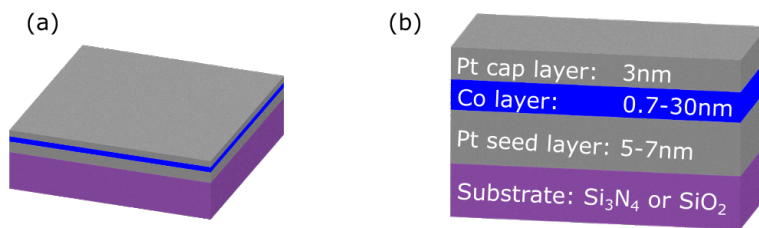


Figure 3.1: (a) and (b) depict a model of the film system. The film is evaporated on a Si_3N_4 or SiO_2 substrate. The first layer consists of 4 nm of Pt that is deposited by electron cyclotron resonance sputtering. This layer of Pt is characterised by a very good texture. On top of the Pt another layer of 1 – 3 nm of Pt is deposited by direct current magnetron sputtering. This Pt layer is deposited with less energy, so that the thickness of the interface with the following Co layer is minimised. The Co layer is varied between 0.7 nm and 30 nm, depending on the experiment. Out-of-plane anisotropies are achieved below 1.2 nm and everything above will have an in-plane anisotropy. Above the Co layer another 3 nm of Pt is deposited by DC magnetron deposition. This layer creates another interface to enhance the out-of-plane anisotropy and also protects the Co layer from oxidation.

Co. The strain contributes to the out-of-plane contribution of the anisotropy. Also the samples are poly-crystalline, with a typical grain diameter of about 16 nm [31]. These grains are tilted to the film normal. The tilt can be described by a Gaussian distribution with a peak in the direction of the film normal at 0° . The half width maximum is 11° and the maximal tilt is 23° . The tilt is isotropically distributed in all spatial directions and therefore disappears on average. The ramifications of these structural properties will be discussed in the main part of this thesis.

3.2 Measurement technique

The goal of this thesis was to study the magnetic properties of ultrathin Pt/Co/Pt films and nanostructures, with the main focus on the magnetic anisotropy. The measurement principle for the films is basic magnetotransport measurement, with a direct current applied. Pads made of gold are used to contact the samples by wire bonding and the longitudinal as well as the transversal voltage are measured. The nanostructures are probed by Hall magnetometry. Therefore nanosized Hall bars are used to study the magnetisation behaviour of single nanodots. The basic effects behind the method are the ordinary and anomalous Hall effect. The ordinary Hall effect (OHE) occurs in Pt and Co and is proportional to the applied magnetic field. The anomalous Hall effect (AHE) emerges only in Co, as it solely appears in ferromagnetic materials. It is dependent of the magnetisation. The resulting Hall voltage is given by:

$$U_{\text{Hall}} = \mu_0 (R_{\text{OHE}}H_Z + R_{\text{AHE}}M_Z) I_X/t \quad (3.1)$$

R_{OHE} and R_{AHE} are the corresponding Hall constants and H_Z and M_Z the perpendicular components of the applied field and the magnetisation of the sample. I_X is the applied current and t the dimension of the sample. Both effects are present in Pt/Co/Pt systems, but the AHE term $R_{\text{AHE}}M_Z$ dominates the OHE term by orders of magnitude. Thus the perpendicular component of the magnetisation is directly proportional to the Hall voltage U_{Hall} . Since the investigated samples possess an easy axis of magnetisation that lies perpendicular to the film plane, the magnetisation is directly measurable.

The core issue with this technique is the current flow through the Co. In our case,

3 Sample preparation and experimental details

the interfaces between the Co and the Pt ensure this point.

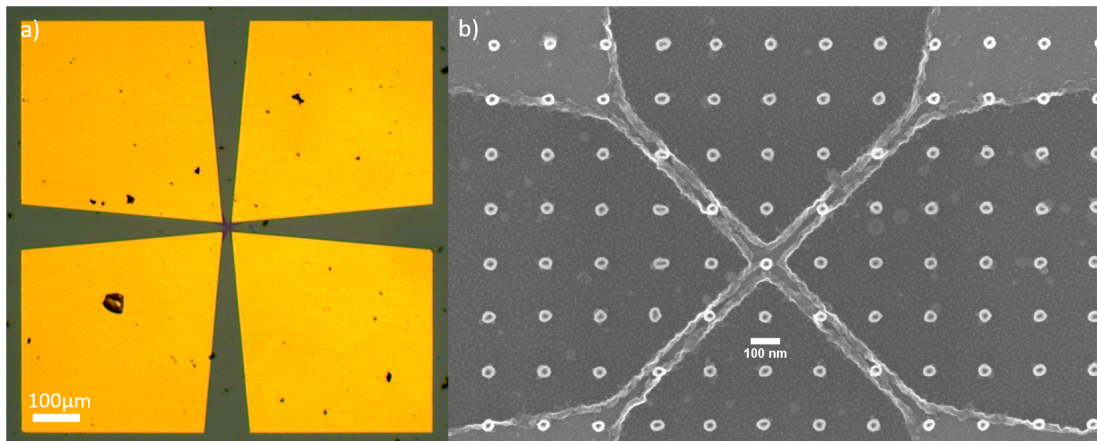


Figure 3.2: a) A microscope image of the four gold plates to contact the samples. The area between the pads has a size of $20\ \mu\text{m} \times 20\ \mu\text{m}$. b) A SEM micrograph of a typical Hall bar. The leads have a width of 80 nm and the nanodot has a diameter of 45 nm.

3.3 Lithography and nano-structuring

The creation of the nanostructures requires distinguished fabrication processes that are based on photo- and electron-beam-lithography [29, 30]. In a first step, the Pt/Co/Pt film is covered with contact pads made of gold. This is done with standard photo-lithography technique utilising a shadow mask and a negative photo-resist. Afterwards Au is evaporated by sputter coating and the remaining resist is removed in an ultrasonic bath. These golden contact pads are used for aluminium wire bonding to contact the sample. The gold pads are shown in fig. 3.2 a) and a finished Hall bar in fig. 3.2 b).

Afterwards an array of nanodots is fabricated between the four contact pads. The process is depicted in fig. 3.3. This is done by using electron beam lithography and a negative electron beam resist to create cylindrical shadow masks. With the SEM and commercially available electron beam resist, a minimal diameter of 35 nm was possible. To further reduce the diameter of the shadow masks an oxygen plasma could be used. Unfortunately the cylindrical shadow mask would fall over, if the ratio of diameter and height (80 nm) would become critical. Due to this the resist was diluted and the height of the resist reduced. This allowed to create shadow masks with a diameter as small as 12 nm. Afterwards the film is etched by using argon ion milling. The cylindrical shadow masks protect the film beneath them, so that the dots are carved into the film. The etching process is stopped in

3 Sample preparation and experimental details

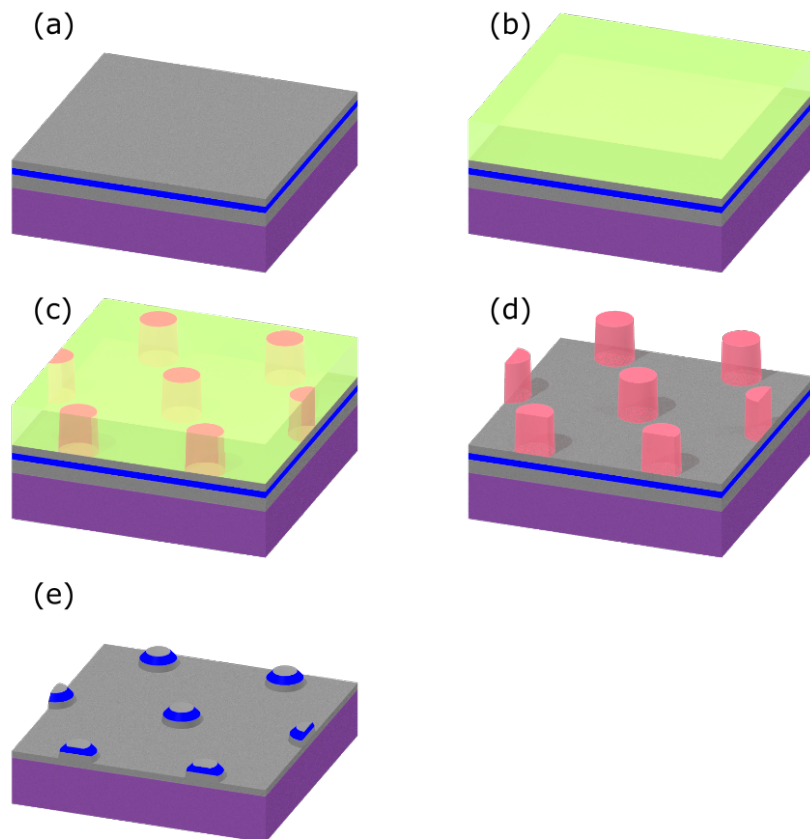


Figure 3.3: The figure shows the creation of the nanodots from a thin film. (a) The starting point is a thin film, that was created by sputter deposition. The composition of the film is described in fig. 3.1. The procedure is optimised for this film composition but can also be applied to other systems. (b) The film is coated with a negative electron beam resist by using spin coating. (c) The resist is exposed to the electron beam. An array of dots is written. (d) The resist is developed. The parts of the resist, that were not exposed to the electron beam are removed by the developer. An array of resist cylinders remains, that serve as a shadow mask. (e) The film with the shadow mask on top is subjected to an ion milling process. The film is removed, except for the parts that are protected by the shadow mask. The ion milling is stopped in the lower Pt layer and the sample is cleaned to remove the remaining resist.

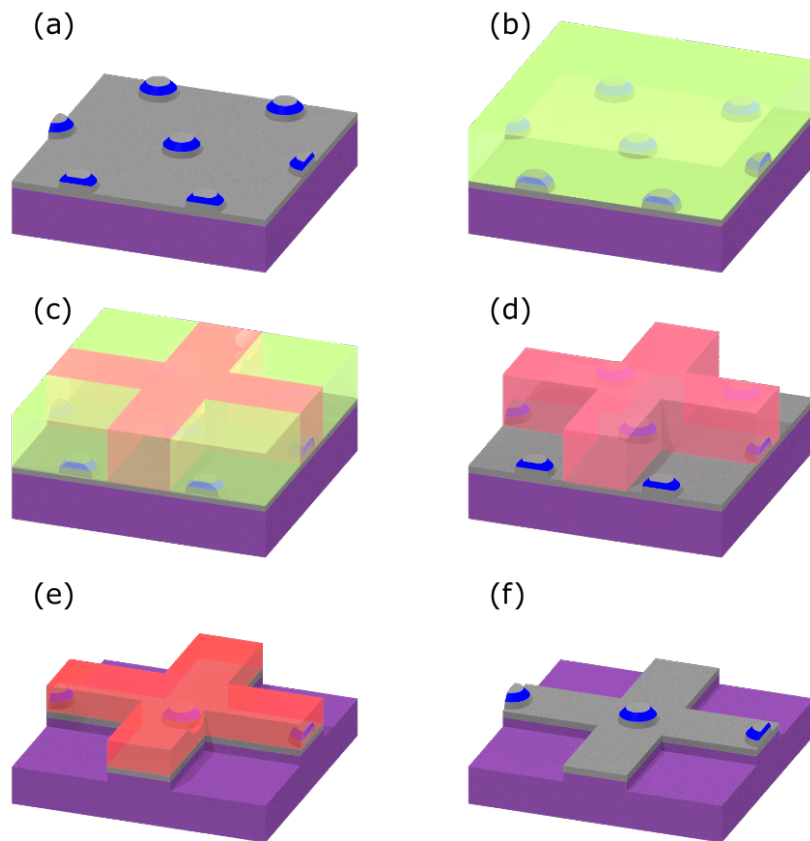


Figure 3.4: The figure shows the creation of the Hall bar. (a) The sample from fig. 3.3 e) serves as the starting point. (b) The sample is coated with a negative electron beam resist. (c) The resist is exposed to the electron beam. A cross is written by the electron beam. (d) The resist is developed and the non-exposed resist is removed. The cross shape remains on the sample and serves as a shadow mask. (e) The remaining film is removed by ion milling. The part beneath the shadow mask is protected from the ion milling. (f) The sample is cleaned and the remaining resist is removed. A Hall bar is created from the remaining Pt layer, with a single nanodot in the crossing area of the Hall bar.

3 Sample preparation and experimental details

the Pt seed layer, which will later be used as the current lead through the nanodot. Usually about 2 nm of the seed layer are removed. After ion milling the diameter of the nanodots will always exceed that of the shadow masks. Possible reasons for this are redeposition of sputtered materials or a bloating of the shadow mask during the ion milling process. Nanodots with a diameter ranging from 16 nm to 45 nm were fabricated and investigated in this thesis.

Finally the process is repeated to create the nanosized Hall bar, that served as the aforementioned current lead and the measuring probe for the magnetisation. This can be seen in fig. 3.4. Again using electron beam lithography and utilising the alignment program of the software, a Hall bar shadow mask is build above the nanodot array. The width of the single leads is usually chosen to be 80 nm though it may also be smaller, e.g. 60 nm, depending on the size of the nanodot. With perfect alignment the crossing area will cover a single nanodot. Afterwards the ion milling is used once again, this time removing the remaining seed layer, except where it is protected by the shadow mask. The latter now needs to be removed, which is usually achieved by oxygen plasma, though sometimes a treatment with peroxymonosulfuric acid is necessary. Usually 36 samples are produced on one substrate, with at least half of them defective, as the alignment of nanodots and Hall bar did not work out or for other reasons like a defect in the resist.

The typical layout is the Hall bar shown fig. 3.2 with the four leads. Two of the leads will be used to apply the current. Usually $20 - 40 \mu\text{a}$ are applied. The other two leads will be used to measure the Hall voltage. The voltage usually has a magnitude of several hundred nV. Since it was interesting to also measure longitudinal magnetoresistance effects, the layout was extended. To achieve this, eight contact pads were put on the sample and the Hall bar had two additional leads, to pick up the longitudinal voltage. This is shown in fig. 3.5. These additional leads ought to be as close to the crossing area, that contains the nanodot, as possible. This was limited due to the proximity effect. The lead for the Hall voltage and the two leads for the longitudinal voltage would fuse together if the distance between them is too small. A distance of 60 nm could be achieved. While the lithography was successful, the longitudinal magnetoresistance of a single nanodot could not be probed. The reason for this is probably the poor filling factor. Due to this the magnetoresistance effects of the magnetic nanodot are superimposed by effects stemming from the Pt seed layer. As a consequence,

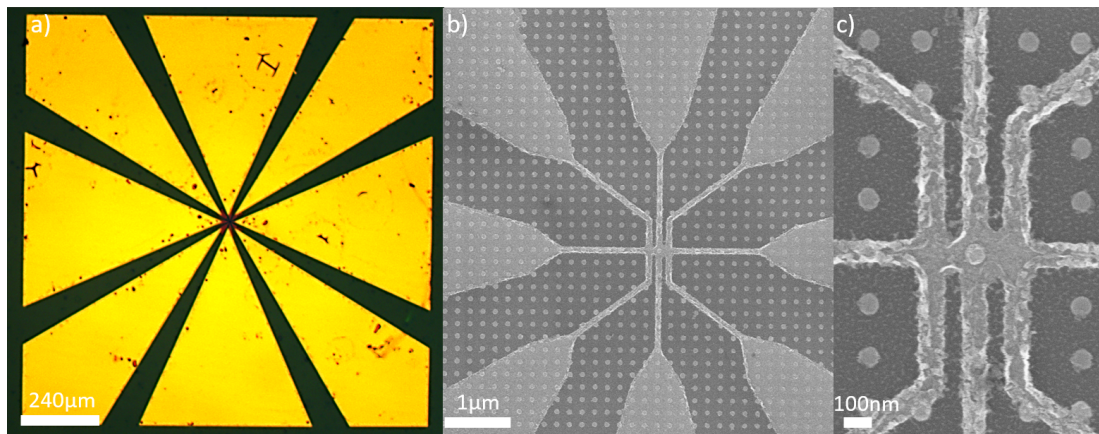


Figure 3.5: a) Displays a microscope image of the eight gold plates to contact the samples. The area between the pads has a size of $40\ \mu\text{m} \times 40\ \mu\text{m}$. b) Additional leads have been added to the Hall bar, allowing the measurement of the longitudinal voltage. c) The width of the leads is 80 nm. The space between the leads is 60 nm.

the idea to measure longitudinal magnetoresistance effects in single magnetic nanodots was no longer pursued.

In collaboration with projects working with synchrotron radiation big arrays of magnetic nanodots on ultrathin Si_3Ni_4 ($t = 25 - 100\ \text{nm}$) membranes were made. Fabricating these had a very particular difficulty, as the membranes would very easily rupture with the slightest bit of touch, thus requiring pronounced fine-motor skills. The two techniques based on synchrotron radiation used to investigate the nanodots were magnetic x-ray holography and coherent x-ray scattering. For x-ray holography dot arrays in simple cubic and kagome lattice were made with varying distance between the dots. Since more magnetic material is needed to do holography, Pt/Co/Pt-multilayers were used instead of single layers. In fig. 3.6 an SEM image of a Kagome lattice is depicted as well as a magnetic hologram. The measurements were performed by J.Wagner, R.Frömter and others and are discussed in J.Wagners PhD thesis [85].

For the coherent x-ray scattering simple cubic lattices were made. One lattice was a checkerboard with alternating hard and soft magnetic nanodots. This was done by using positive electron beam resist. With electron beam lithography nanosized holes were created in the resist and later filled with magnetic material. Afterwards the resist was removed and magnetic nanodots remained. The process was repeated and with alignment technique it was possible to make this aforementioned

3 Sample preparation and experimental details

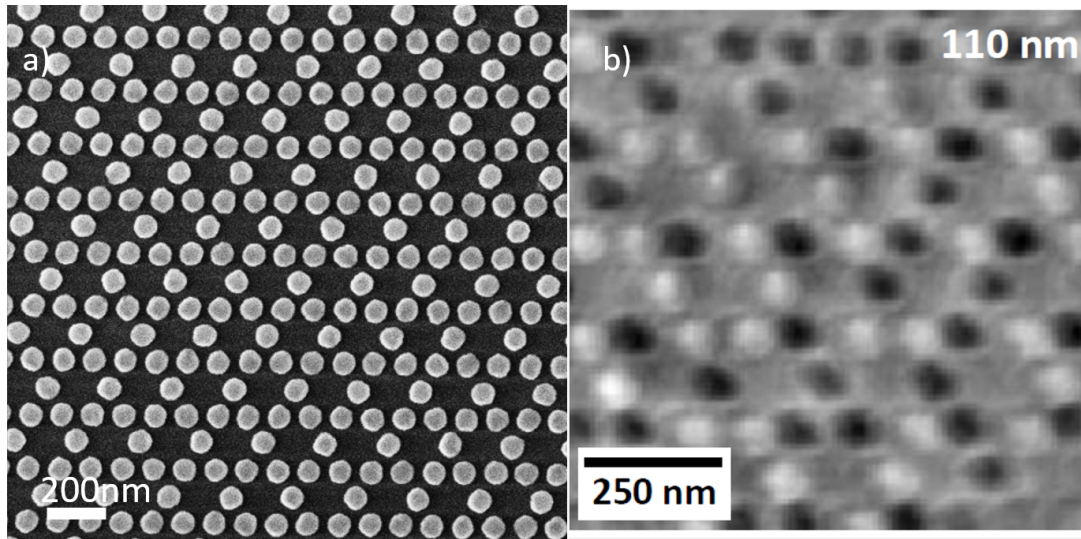


Figure 3.6: a) Displays a Kagome lattice of multi-layered Co/Pt nanodots. The sample was created on a silicon nitride membrane that allows X-ray transmission measurements. b) A magnetic X-ray holographic measurement of a Kagome lattice as shown in a). The 110 nm in the upper right describe the distance from center point to center point of to aligning dots. The measurement was performed by J. Wagner, R. Frömter and others at the Petra 3 beamline at Desy. The technique is described in Wagners PhD thesis [85].

chequerboards. In fig. 3.7 SEM images of the chequerboard are shown.

3.4 Experimental setup

The samples are electrically contacted by using wire wedge-bonding. Various experimental setups were used over the course of the thesis. Mainly a setup consisting of a cooling finger and a rotatable electro-magnet has been used. The cooling finger allows to investigate the sample in a temperature range of 77.5 K and 300 K, when using liquid nitrogen. The electro-magnet can apply magnetic fields up to 800 mT. The electro-magnet can be rotated in one plane by 360°, allowing measurements in the film plane, film normal and in arbitrary angles in between.

The second setup is a SpectroMag, which is a cryostat with a superconducting coil from Oxford Instruments. The SpectroMag is used in a temperature range of 2.5 K up to 300 K. Magnetic fields up to 6 T are applied. The sample holder can be rotated within the magnetic field. Using an in plane or out of plane holder allows to measure arbitrary angles.

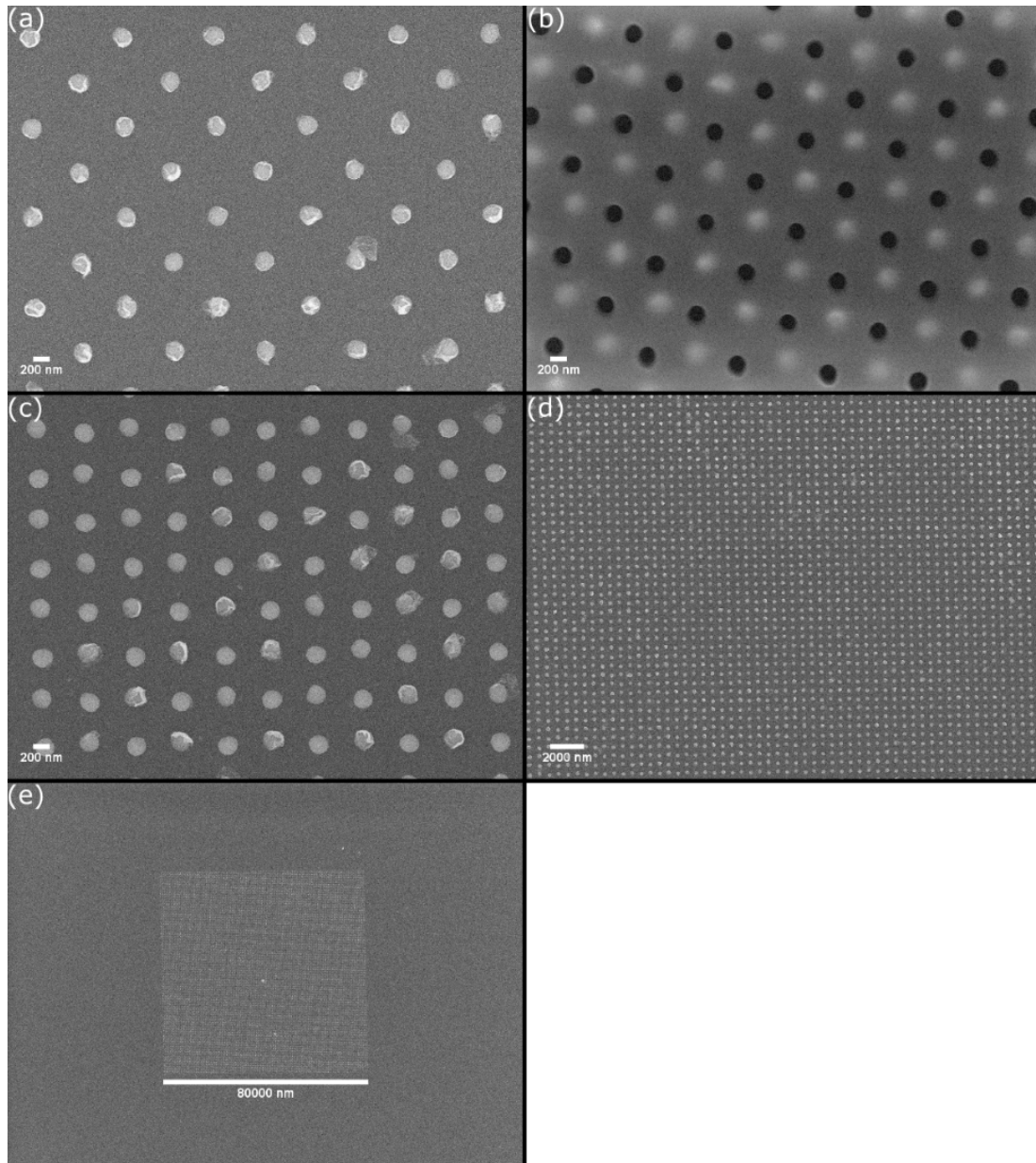


Figure 3.7: (a) The first lattice of magnetically soft dots is created by using an additive lithography technique. The diameter of the dots is 200 nm. (b) A positive electron beam resist is layered on top of the dots. The black holes serve as evaporation mask for the second lattice. The two lattices are aligned by the software. (c) The second lattice of dots is created and fits shows a good alignment with the first lattice. (d) and (e) The finished checkerboard is shown in larger magnification. The lattice constant of the checkerboard is 500 nm. The overall size of the checkerboard is $80 \mu\text{m} \times 80 \mu\text{m}$

3 Sample preparation and experimental details

Third, is the Dynacool a closed-cycle cryostat by 'Quantum Design'. The Dynacool can vary the temperature very fast in a range of 2.5 K up to 300 K. Like in the SpectroMag up to 6 T are applied, but only perpendicular to the sample.

The fourth experimental setup is a three dimensional vector magnet from 'Oxford Instruments'. This cryostat has three superconducting coils. Therefore the magnetic field can be applied in every spatial angle up to 500 mT.

4 Magnetisation behaviour of ultrathin magnetic films

4.1 Temperature dependence of the anisotropy in ultrathin magnetic films

4.1.1 Introduction

Sec. 3.1 introduced the Co/Pt multilayers that have been the subject of extensive research over the past two decades [21–27]. The Co/Pt films are always fabricated in the same way. Via electron cyclotron sputtering a Pt seed layer is deposited on either a silicon oxide (SiO_2) or a silicon nitride (Si_3N_4) substrate. The high energy of the deposited atoms creates a film with a fcc (111) texture. Afterwards another Pt layer, followed by the Co layer and a final Pt cap layer is deposited on the ECR-Pt seed layer. For this part DC-magnetron sputtering is used. The lower energy of the technique generates better defined interfaces. The Co layer grows in a (111) fcc crystal structure and the film is poly-crystalline. The typical grain size is 16 nm. The grains are also tilted from the film normal. The tilting can be described by a Gaussian distribution with the peak at zero degree. For a SiO_2 substrate a sigma of $\sigma = 11^\circ$ and a maximal tilting of 23° are found. The tilting is isotropically distributed in all spatial directions. The magnetic properties of the film can be described by an uniaxial anisotropy model. Most importantly, the films exhibit a spin reorientation transition, meaning the easy axis of magnetisation switches from in-plane for a high Co thickness to out-of-plane for a small Co thickness. When the transition occurs depends on the substrate. Usually the SRT lies between 1.5 nm and 1.2 nm. The films are well understood, nevertheless open questions remain, for example the temperature dependence of the ferromagnetic anisotropy.

4 Magnetisation behaviour of ultrathin magnetic films

The magnetocrystalline anisotropy is the result of spin-orbit coupling. Due to the exchange coupling the individual moments of the atoms build a reasonable energy contribution. This is linked to the structure of the crystal, resulting in energetically favoured and less-favoured directions of the magnetisations. The energy difference between the favoured direction (called easy axis) of magnetisation and the least-favoured direction (called hard axis of magnetisation) is called the anisotropy energy, which is characterised by a strong temperature dependence. This is not caused by the spin-orbit coupling. The mechanism behind the temperature dependence of the anisotropy is thermal excitation of individual magnetic moments. The moments will start to precess and the perfect alignment is destroyed, resulting in a decrease of the anisotropy. Akulov [86] and Van Vleck [87] published the first theoretical investigation both using a quantum mechanical approach. Zener [88] later used a classical ansatz. Keffer [89], Carr [90, 91] and Kittel [92] expanded the existing theories. Later, Callen and Callen [93, 94] solved the problem for low temperatures, while Jensen [95] extended the theory to higher temperatures. The result is a power law given by $K(T) = K(0)(M_S(T)/M(0))^n$. The magnitude of n differs for fcc ($n = 10$) and hcp ($n = 3$). As can be seen, the temperature dependence of the anisotropy is determined by the temperature dependence of the saturation magnetisation.

For the saturation magnetisation of Co the value given by Crangle will be used [48]. He gives $M_S(0) = 1.458 \text{ MA/m}$. The temperature dependence of the saturation magnetisation is described by Bloch's $T^{\frac{3}{2}}$ law [72]. M_S is reduced with rising temperature due to the increased creation of spin waves. The law is not valid close to the Curie temperature T_C . It is defined as:

$$M_S(T) = M_S(0)(1 - BT^{\frac{3}{2}}) \quad (4.1)$$

B is a constant that is depending on the exchange stiffness A and the lattice constant a . For Co $B = 1.5 \cdot 10^{-6} \text{ K}^{2/3}$ at 100 K can be found in literature [73]. In this thesis a temperature window ranging from 2.5 K to 300 K has been investigated. The saturation magnetisation would be reduced from $M_S(0) = 1.458 \text{ MA/m}$ to $M_S(300 \text{ K}) = 1.447 \text{ MA/m}$. This is a reduction of 0.75%. Kuz'min proposed an analytical expression for the shape of $M_S(T)$ [96]. He found that most ferromagnetic materials obey the formula, based on the available experimental

4.1 Temperature dependence of the anisotropy in ultrathin magnetic films

data. That includes fcc Co. The expression is given as:

$$M_S(T) = M(0) \left(1 - s \cdot \left(\frac{T}{T_C} \right)^{\frac{3}{2}} - (1 - s) \left(\frac{T}{T_C} \right)^p \right)^{\frac{1}{3}} \quad (4.2)$$

s and p are material parameters, as well as the Curie temperature T_C . For fcc Co the following values are given: $s = 0.11$, $p = 5/2$ and $T_C = 1385$ K. Using this equation a reduction from $M_S(0) = 1.458$ MA/m to $M_S(300 \text{ K}) = 1.443$ MA/m is found. This is a reduction of 1%. In the following the temperature dependence given by Kuz'min is used, as the factor B in the Bloch $T^{\frac{3}{2}}$ law is only given for $T < 100$ K. However, the deviations for both models are pretty small.

The temperature dependence of the anisotropy for bulk hcp Co is well known. First qualitatively good measurements were performed by Sucksmith and Thompson [97] in 1954 and was later on the research was continued by many others [98–108]. While the temperature dependence is qualitatively the same, the quantitative value of the anisotropy constant has a spread of about 30%. This lack of consistency is taken up by Paige et al. [108], who finds inaccuracies in some works and concludes that the best results are indeed given by Sucksmith and Thompson [97], Ono [106, 107] and himself. The first order of the magnetic anisotropy K_1 remains constant up to the point of about 130 K, from where on it starts to decrease linearly. In this thesis, the temperature window between 2.5 K and 300 K is important. The work of Ono shows a decrease in this window from $K_1(2.5 \text{ K}) = 770$ kJ/m³ to about $K_1(300 \text{ K}) = 500$ kJ/m³. Paige [108] also compares the results for the second order of the anisotropy K_2 . It can be concluded that the second order is constant in the relevant temperature range.

Regarding the Co/Pt films investigated in this thesis, previous investigations [27] reveal that Co grows in the fcc phase. Despite the fcc structure, the films do not show a cubic anisotropy but an effectively acting uniaxial anisotropy. Suzuki et al. [109] determined the anisotropy constants $K_{\text{cub},1}$ and $K_{\text{cub},2}$ of thick fcc Co films ($t_{\text{Co}} \approx 100$ nm) at 77 K and 300 K. $K_{\text{cub},1}$ decreases linearly from -72 kJ/m³ to -62 kJ/m³. $K_{\text{cub},2}$ decreases from (20 ± 5) kJ/m³ to a value of the order of 10^3 J/m³.

Kobs [26] started the investigation of the temperature dependence in ultra-thin films. This thesis will present a continuation of that investigation.

4 Magnetisation behaviour of ultrathin magnetic films

4.1.2 Determination of anisotropy constants in magnetic films

To determine the anisotropy constants of Pt/Co/Pt films, Hall bar magnetometry has been performed. Therefore a magnetic field sweep is performed in the hard axis of magnetisation, which is the film normal of the film, and the resistance in dependence of the field is measured. This is called Hall resistance and consists of the normal Hall effect and the anomalous Hall effect (s.a. sec. 2.5.2) and is given by $R_{\text{Hall}} = \mu_0 (R_{\text{OHE}} H_Z + R_{\text{AHE}} M_Z) 1/t$. R_{OHE} and R_{AHE} are the normal and anomalous Hall constants. The normal Hall effect manifest in a linear slope that is proportional to the applied magnetic field, which emerges above technical saturation, hence if $M_Z \parallel H_Z$. As the normal Hall constant in Pt and Co is negative, a negative slope emerges. Since only the anomalous Hall effect is significant for the determination of the anisotropy, the normal Hall effect is extrapolated to zero field and subtracted from the measurement (see inset in fig. 4.1). Under the assumption of coherent reversal of the magnetisation, the anisotropy will be determined from the rotation of the magnetisation from the easy axis of magnetisation to the hard axis. From this rotation the anisotropy can be determined, as long as the saturation magnetisation is known. The formula is derived from the model of coherent rotation $E/V = K_1 \sin^2(\theta) + K_2 \sin^4(\theta) - \mu_0 M_S H \cos(\theta - \phi)$ with $\phi = 90^\circ$, as hard axis field sweeps are performed. Determining the energy minimum $\frac{E/V}{\theta} = 0$ and substituting $\cos(\theta)$ with $M_Z/M_S = m_Z$ results in:

$$\frac{2K_1}{M_S} m_Z + \frac{4K_2}{M_S} (1 - m_Z)^2 m_Z = -\mu_0 H \quad (4.3)$$

m_Z is identical to U_{Hall}/U_S , since the Hall voltage is proportional to the magnetisation, which means K_1 and K_2 can be determined by fitting the formula to the inverse curve of the measured data. An example is shown in fig. 4.1. This measurement was performed for a sample with a Co thickness of 3.2 nm evaporated on a SiO₂-substrate and at 150 K. As can be seen the formula is fitted very well to the measured data. From the fit $K_1 = -(602 \pm 0.5) \text{kJ/m}^3$ has been determined. For K_2 a mean value of $K_2 = (70 \pm 30) \text{kJ/m}^3$ has been found, which is in the span of numbers found in literature. To avoid an impact on the investigation of K_1 , K_2 has been set to 70kJ/m^3 . For the saturation magnetisation of fcc Co $M_S = 1458 \text{kA/m}$ at $T = 0 \text{K}$ is used. To respect the temperature dependence of

4.1 Temperature dependence of the anisotropy in ultrathin magnetic films

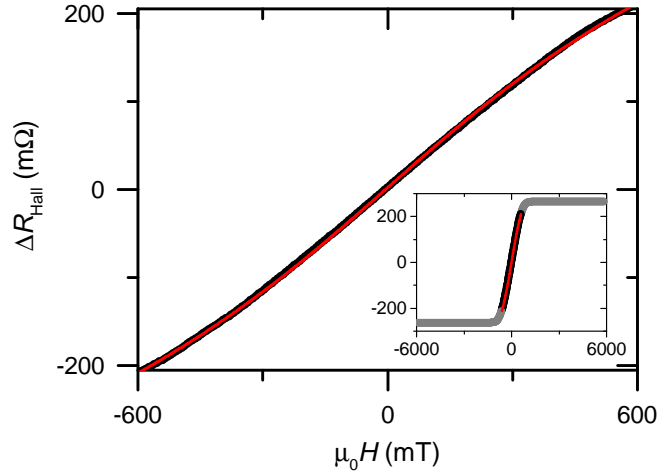


Figure 4.1: Magnetisation reversal vs. magnetic field for a Co thickness of 3.2 nm evaporated on a SiO₂-substrate measured at 150 K. The red line shows the fit of eq. 4.3 in order to determine K_1 . From the fit $K_1 = -(602 \pm 0.5)$ was determined with $K_2 = 70 \text{ kJ/m}^3$ and $M_S = 1454 \text{ kA/m}$ as fit parameters. The inset show the complete measurement. In gray is the high field behaviour where $M_Z \parallel H_Z$, which is not part of the fit.

M_S the model of Kuz'min was applied. It is important to note that the temperature dependence of M_S affect only slightly the fitting results. The outcome of the investigation is discussed in the following section.

4.1.3 Silicon oxide substrate

In this chapter the samples that were sputtered on a SiO₂-substrate will be discussed. Overall eleven samples have been investigated with the lowest Co thickness being 2 nm and the highest 30 nm. All of the samples possess an in-plane anisotropy, which means that the easy axis of magnetisation lies within the film plane. The measurements were performed in a DynaCool cryostat as explained in the preceding chapter. The temperature range reached from 2.5 K to 300 K. The temperature dependence of the effective anisotropy K_{eff} is shown in fig. 4.2. Two distinct behaviours are found. At higher thickness above 4 nm the effective anisotropy is decreasing with rising temperature and for a lower thickness of 2 nm the anisotropy is increasing. When looking at the data points in more detail a

4 Magnetisation behaviour of ultrathin magnetic films

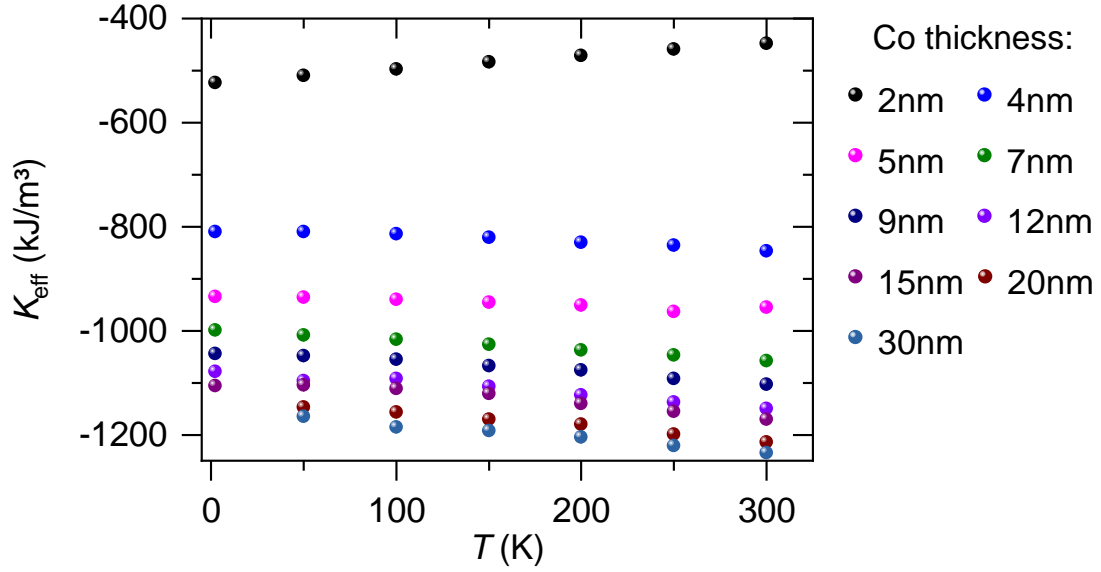


Figure 4.2: The graph shows the effective anisotropy vs. the temperature for varying Co thickness. For 2 nm the anisotropy increases linearly. Below 4 nm the anisotropy decreases linearly.

few characteristics are noteworthy. For example although the anisotropy is overall increasing for lower thickness, between 200 K and 250 K the increase is halted and the slope of the temperature dependence seems to change the sign. Additionally the values for 20 nm and 30 nm don't differ much from each other. At this thickness the interface anisotropy does not contribute much to the system and the effective anisotropy is dominated by the volume anisotropy. Overall a linear approach for the temperature dependence is justifiable. The effective anisotropy is then given by:

$$K_{\text{eff}}(T) = K_{V,0} + K_{V,T} \cdot T + \frac{2(K_{S,0} + K_{S,T} \cdot T)}{t} \quad (4.4)$$

In order to quantify the effect, linear equations are fitted to the data in the temperature range of 50 K to 250 K. This range was chosen because for some samples the values at 2.5 K or 300 K deviate from a linear behaviour (for example 20 nm in fig. 4.2). The slope of the fit determines the size of the effect $\frac{dK_{\text{eff}}}{dT}$ and is shown in fig. 4.3. At 2 nm the slope is positive with a magnitude of $(250 \pm 1) \text{ J/m}^3\text{K}$. Between 2 nm and 4 nm the slope changes to a negative value and is reduced to $(-138 \pm 1) \text{ J/m}^3\text{K}$. With increasing Co thickness the slope decreases further

4.1 Temperature dependence of the anisotropy in ultrathin magnetic films

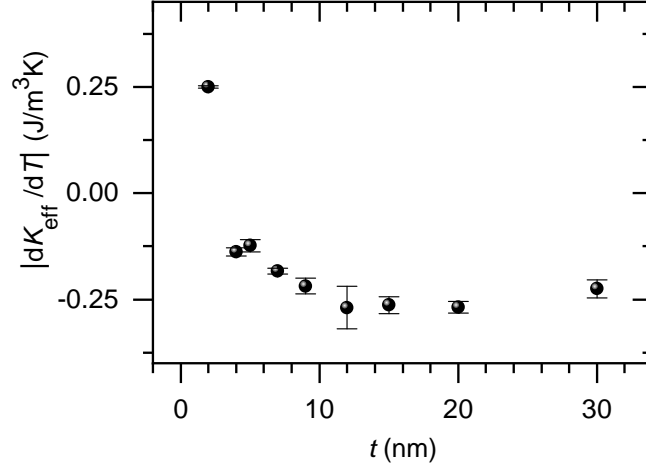


Figure 4.3: The graph shows the slope of the temperature dependence. At 2 nm the slope is positive with a magnitude of $(250 \pm 1) \text{ J/m}^3\text{K}$. Between 2 nm and 4 nm the slope changes to a negative value and is reduced to $(-138 \pm 1) \text{ J/m}^3\text{K}$. With increasing Co thickness, the slope decreases further and saturates to a mean value of $(-270 \pm 45) \text{ J/m}^3\text{K}$.

and saturates to a mean value of $(-270 \pm 45) \text{ J/m}^3\text{K}$. Two of the linear fits mentioned above are used in a system of linear equations, in order to determine $K_V(T) = K_{V,0} + K_{V,T} \cdot T$ and $K_S(T) = K_{S,0} + K_{S,T} \cdot T$. For the analysis the data points of 2 nm and 7 nm are used. The linear fits of $K_{\text{Eff},2\text{nm}}(T)$ and $K_{\text{Eff},7\text{nm}}(T)$ are used to solve a system of linear equations. This results in:

$$K_{V,\text{Eff}}(T) = 1189 \frac{\text{kJ}}{\text{m}^3} - 0.37 \frac{\text{kJ}}{\text{m}^3\text{K}} \cdot T \quad (4.5)$$

$$K_S(T) = 666 \cdot 10^{-3} \frac{\text{J}}{\text{m}^2} - 0.62 \cdot 10^{-3} \frac{\text{J}}{\text{m}^2\text{K}} \cdot T \cdot \frac{1}{t} \text{ nm} \quad (4.6)$$

The result is shown in 4.4. The solid lines are the linear equations used to calculate $K_S(T)$ and $K_{V,\text{eff}}(T)$. The dashed lines represent the results for the corresponding thickness. Though there is an offset between the model and the 4 nm sample, most measurement are described well by the model. This implies a linear temperature response of both anisotropy contributions.

To further elaborate on that point, a second method is used, which takes all data points into account. $K_{V,\text{eff}}(T)$ and $K_S(T)$ can be determined by plotting the data

4 Magnetisation behaviour of ultrathin magnetic films

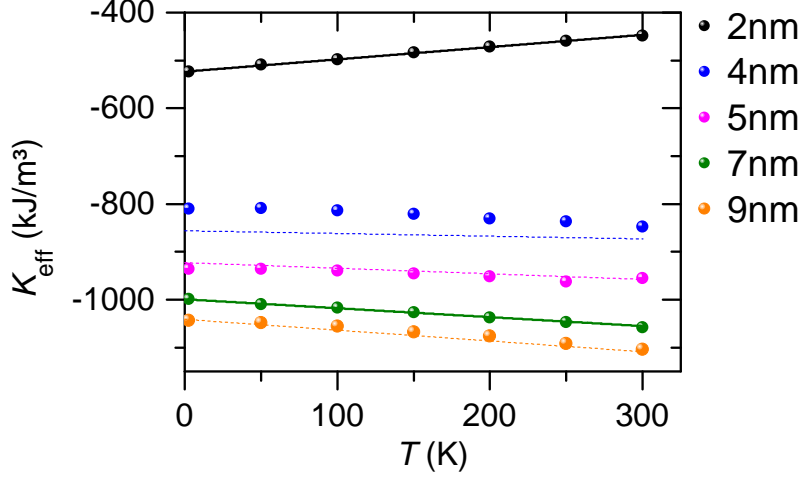


Figure 4.4: The effective anisotropy over temperature for varying Co thickness. For 2 nm and 7 nm linear fits were applied. From a system of linear equations predictions for 4 nm, 5 nm and 9 nm were made. While there seems to be an offset for the first, the others fit quite well, showing that the interface and volume anisotropy might be linear in their response to temperature.

points as $K_{\text{eff}} \cdot t$ over t . This will give one plot for every temperature. $K_{\text{eff}}(t) \cdot t$ can be expressed as $K_{\text{eff}} \cdot t = K_{\text{V,eff}} \cdot t + 2K_{\text{S}}$. By fitting a linear function to the plot, $K_{\text{V,eff}}$ can be determined from the slope and K_{S} from the intercept of the fit. Two exemplary measurements are shown in fig. 4.5. One at 300 K and one at 50 K. Both data sets are described by a linear equation. This holds true for all measurements of the SiO_2 samples in the investigated temperature range. The obtained value for K_{S} and $K_{\text{V,eff}}$ are plotted in fig. 4.6. Also K_{V} is shown, that can be determined by subtracting the shape anisotropy from $K_{\text{V,eff}}$. K_{S} increases from $670 \mu\text{J}/\text{m}^2$ at 2.5 K to $835 \mu\text{J}/\text{m}^2$ at 300 K. The red line in fig. 4.6 shows a linear fit over the whole temperature range.

$K_{\text{V,eff}}$ decreases from $-1193 \text{ kJ}/\text{m}^3$ at 2.5 K to $-1281 \text{ kJ}/\text{m}^3$ at 300 K. K_{V} decreases from $142 \text{ kJ}/\text{m}^3$ at 2.5 K to $-1281 \text{ kJ}/\text{m}^3$ at 29 K. All terms show a linear behaviour, so that K_{S} , $K_{\text{V,eff}}$ and K_{V} can be expressed as linear functions of T :

$$K_{\text{S}}(T) = K_{\text{S},0} + K_{\text{S},T} \cdot T \quad (4.7)$$

$$K_{\text{V,eff}}(T) = K_{\text{V},0} + K_{\text{V,eff},T} \cdot T \quad (4.8)$$

4.1 Temperature dependence of the anisotropy in ultrathin magnetic films

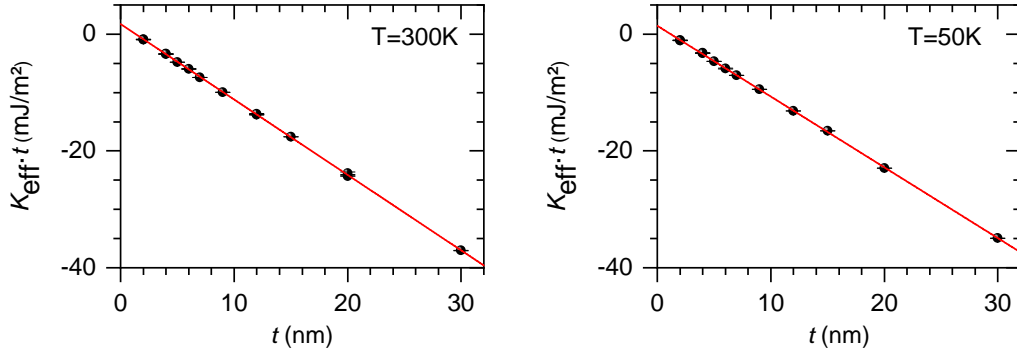


Figure 4.5: To determine the interface and volume anisotropy at different temperatures, $K_{\text{eff}} \cdot t$ over t plots are made. From linear fits K_S and K_V can be determined, where the former is the intercept and the latter is the slope. For all temperatures the linear equation fits well to the data points.

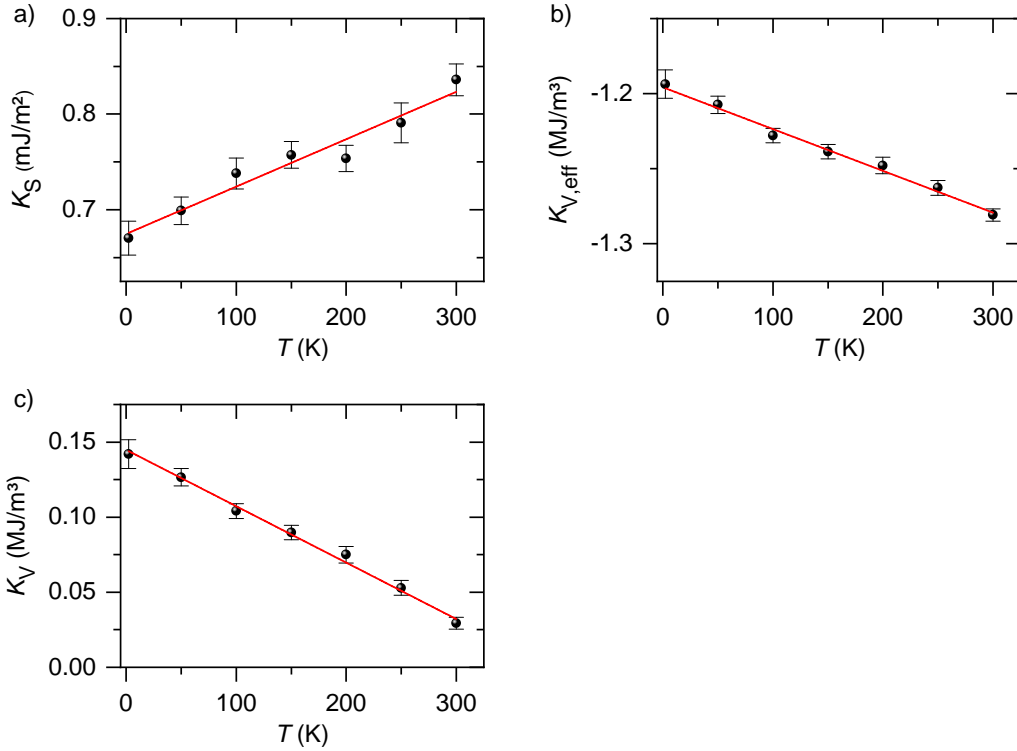


Figure 4.6: The interface anisotropy K_S , the effective volume anisotropy $K_{V,\text{eff}}$ and the volume anisotropy K_V , which is the effective volume anisotropy minus the shape anisotropy are shown for the SiO₂ substrate. The values are determined from the measurements shown in fig. 4.5. The interface anisotropy increases linearly with temperature by $(0.674 \pm 0.07) \mu\text{J}/\text{m}^2\text{K}$. The effective volume anisotropy decreases by $(-0.28 \pm 0.01) \text{kJ}/\text{m}^3\text{K}$, as well as the volume anisotropy that decreases by $(-0.38 \pm 0.01) \text{kJ}/\text{m}^3\text{K}$.

4 Magnetisation behaviour of ultrathin magnetic films

$$K_V(T) = K_V + K_{V,T} \cdot T \quad (4.9)$$

The values that were obtained in the fit are shown in table 4.1. Both methods yield very close results. Nevertheless, the $K_{\text{eff}} \cdot t(t)$ method takes all of the measurements into account and is to be preferred. The solution of the linear equations only uses two data points but can lead to adequate results, when only a few measurements can be performed. In fig. 4.7, the $K_{\text{eff}} \cdot t(t)$ fits of all measured temperatures are

$K_{S,0}$	674 ± 10	$\mu\text{J}/\text{m}^2$
$K_{S,T}$	0.5 ± 0.07	$\mu\text{J}/\text{m}^2\text{K}$
$K_{V,\text{eff},0}$	-1196 ± 2	kJ/m^3
$K_{V,\text{eff},T}$	-0.28 ± 0.01	$\text{kJ}/\text{m}^3\text{K}$
$K_{V,0}$	145 ± 2	kJ/m^3
$K_{V,T}$	-0.38 ± 0.01	$\text{kJ}/\text{m}^3\text{K}$

Table 4.1: The obtained values of the interface and effective volume anisotropy on a SiO_2 substrate

shown for the SiO_2 substrate. The lines are at first parallel to one another and ordered by their temperature. In a thickness range of (4 – 5) nm all lines cross and the order of the lines is reversed. This behaviour is the result of the fact that both the slope and the intercept are linearly dependent of the temperature and that the slope is of an opposing sign to the intercept.

4.1 Temperature dependence of the anisotropy in ultrathin magnetic films

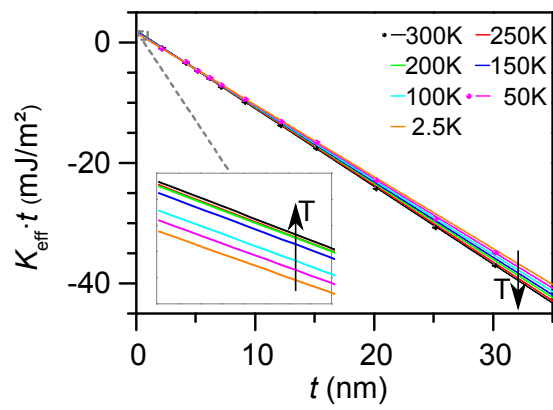


Figure 4.7: The $K_{\text{eff}}(t) \cdot t$ fits of all measured temperatures are shown for the SiO_2 substrate. The lines are at first parallel to one another and ordered by their temperature. In a thickness range of (4 – 5) nm all lines cross another and the order of the lines is reversed.

4 Magnetisation behaviour of ultrathin magnetic films

4.1.4 Silicon nitride substrate

It is known from previous investigations [26, 27], that the choice of the substrate affects the anisotropy. Therefore, films that are prepared on a Si_3N_4 substrate are investigated. Analogous to the previous chapter, the effective anisotropy constants for varying Co thickness have been measured as a function of temperature and are plotted in fig. 4.8. The results are similar to the silicon oxide substrate and a positive slope is found at 1.5 nm and 2 nm, while a negative slope is found above 3.2 nm. The slope is once again determined from linear fits between 50 K and 250 K.

To determine K_S and K_V , $K_{\text{eff}} \cdot t$ as a function of t is plotted. In a contrast to

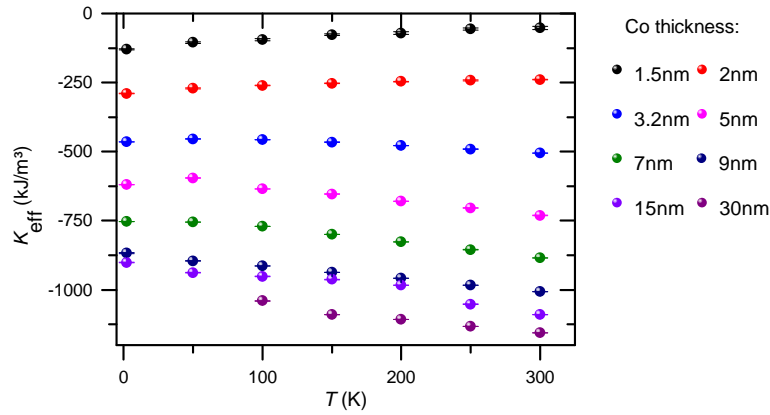


Figure 4.8: To understand the influence of the substrate, the investigation has also been carried out by using samples that were sputtered on a Si_3N_4 substrate. The figure shows the effective anisotropy in response to the temperature for varying Co thickness.

the samples sputtered on a silicon oxide substrate, the $K_{\text{eff}} \cdot t$ over t behaviour is not linear over the whole thickness range. Between 3.2 nm and 5 nm a kink occurs. This can be seen in fig. 4.9, which shows the plot at 300 K and 50 K. The samples in the range from 1.5 nm to 3.2 nm can be described by one linear function as well as the samples ranging from 5 nm to 30 nm. This behaviour is present in the whole temperature range. Therefore, two thickness regimes are defined: the lower thickness regime ($t \leq 3.2$ nm) and the higher thickness regime ($t \geq 5$ nm). For both cases K_S and K_V have been determined. In the lower thickness regime K_S shows a linear increase and K_V a linear decrease, see fig. 4.10. In the higher thickness regime shown in fig. 4.11, K_S seems to be constant, with a high error

4.1 Temperature dependence of the anisotropy in ultrathin magnetic films

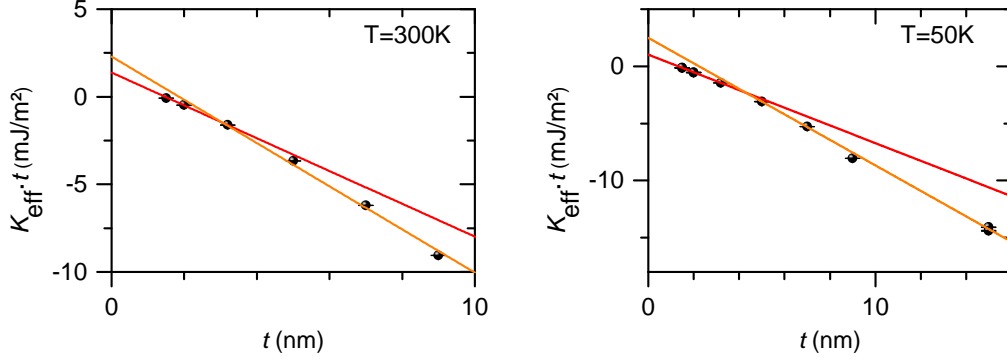


Figure 4.9: $K_{\text{EFF}} \cdot t$ over t plots at 300 K and 50 K. Unlike the SiO_2 substrate, the measurements on the Si_3N_4 substrate can not be described by one linear equation. The first three points are described by the red line and all the points above by the orange line. Therefore two thickness regimes are defined. The lower thickness regime for $t \leq 3.2$ nm and the higher thickness regime for $t \geq 5$ nm. For both regimes the the temperature dependence of the interface and the volume anisotropy has been determined from the linear equations. Note that also measurements at other temperatures have been performed.

bar. K_V as expected from bulk behaviour decreases linearly.

The values are shown in tab. 4.2 together with the values for the silicon oxide substrate from the previous chapter. The comparison will be discussed in the following chapter. The found values are within the span of the literature [110–113] for Co(111) films. The interface anisotropy K_S can be found in the range of $(270 - 1290) \mu\text{J}/\text{m}^2$ at room temperature. For the volume anisotropy $K_V = (80 - 950) \text{kJ}/\text{m}^3$ is published.

	SiO_2	Si_3N_4 ($t \leq 3.2$ nm)	Si_3N_4 ($t \geq 5$ nm)	
$K_{S,0}$	675 ± 10	477 ± 5	-	$\mu\text{J}/\text{m}^2$
$K_{S,T}$	0.50 ± 0.07	0.68 ± 0.02	-	$\mu\text{J}/\text{m}^2\text{K}$
$K_{V,\text{eff},0}$	-1196 ± 2	-745 ± 4	-1062 ± 10	kJ/m^3
$K_{V,\text{eff},T}$	-0.28 ± 0.01	-0.64 ± 0.02	-0.59 ± 0.04	$\text{kJ}/\text{m}^3\text{K}$
$K_{V,0}$	145 ± 2	616 ± 4	275 ± 10	kJ/m^3
$K_{V,T}$	-0.38 ± 0.01	-0.77 ± 0.02	-0.68 ± 0.04	$\text{kJ}/\text{m}^3\text{K}$

Table 4.2: K_S , K_V and $K_{V,\text{eff}}$ for both substrates

4 Magnetisation behaviour of ultrathin magnetic films

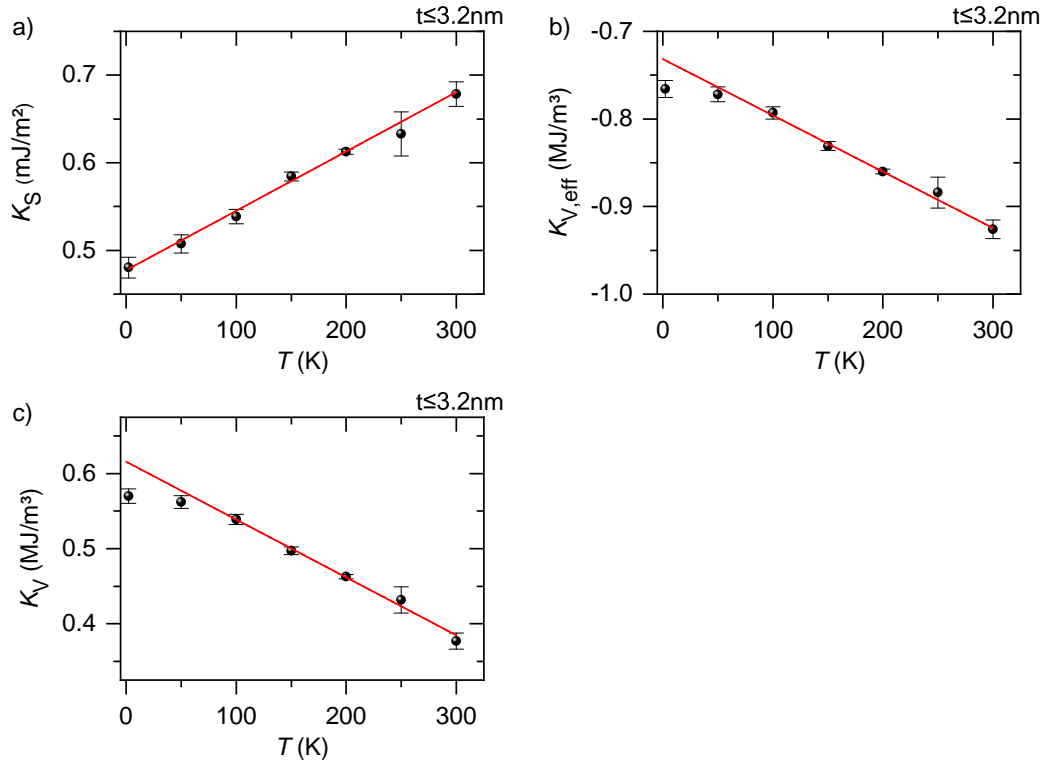


Figure 4.10: The interface anisotropy K_S , the effective volume anisotropy $K_{V,\text{eff}}$ and the volume anisotropy K_V are shown for the lower thickness regime of the Si_3N_4 substrate. The values are determined from the measurements partly shown in fig. 4.9. The interface anisotropy increases linearly with temperature by $(0.68 \pm 0.02) \mu\text{J}/\text{m}^2\text{K}$. The effective volume anisotropy decreases by $(-0.64 \pm 0.02) \text{kJ}/\text{m}^3\text{K}$, as well as the volume anisotropy that decreases by $(-0.77 \pm 0.02) \text{kJ}/\text{m}^3\text{K}$.

4.1 Temperature dependence of the anisotropy in ultrathin magnetic films

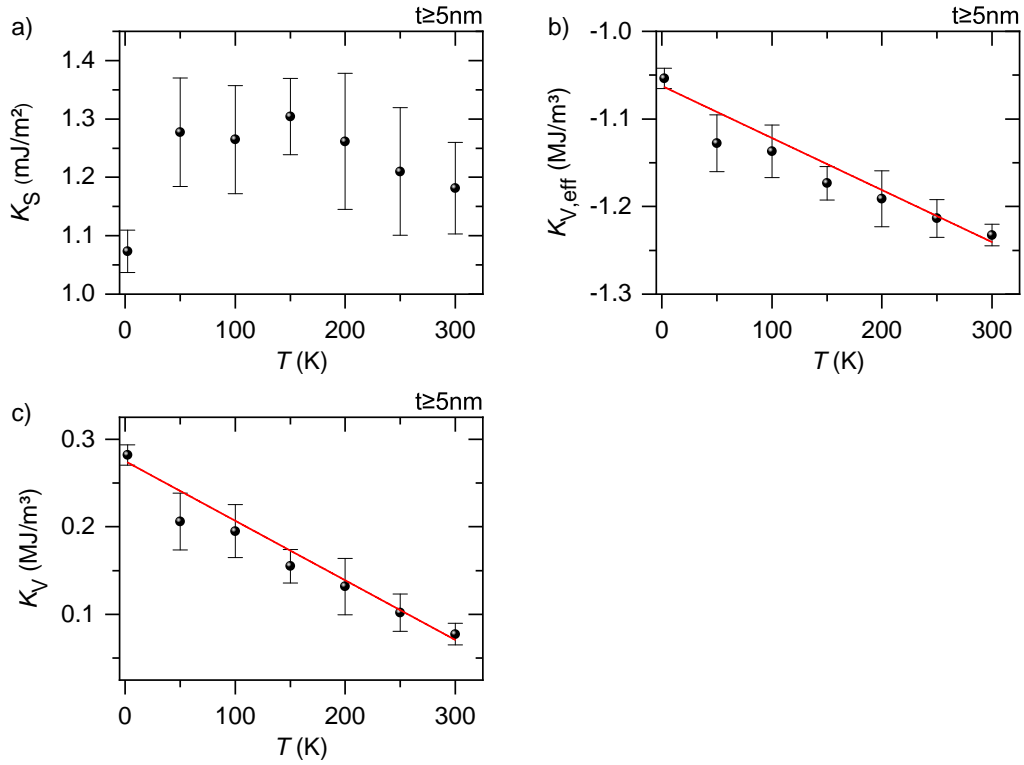


Figure 4.11: The interface anisotropy K_S , the effective volume anisotropy $K_{V,\text{eff}}$ and the volume anisotropy K_V are shown for the higher thickness regime of the Si_3N_4 substrate. The values are determined from the measurements partly shown in fig. 4.9. The slope of the interface anisotropy cannot be determined in the higher thickness regime. The effective volume anisotropy decreases by $(-0.59 \pm 0.04) \text{ kJ/m}^3\text{K}$, as well as the volume anisotropy that decreases by $(-0.68 \pm 0.04) \text{ kJ/m}^3\text{K}$.

4 Magnetisation behaviour of ultrathin magnetic films

Fig. 4.12 compares the $K_{\text{eff}} \cdot t(t)$ plots of both substrates. Blue represents the SiO_2 substrate, while red stands for the Si_3N_4 substrate. The red line is the fit of the higher thickness regime and the orange line is the fit of the lower thickness regime. The blue line is the fit of the SiO_2 data points.

The kink leads to different volume and interface anisotropies in the lower and higher thickness regimes. Similar behaviour in Co/Pt films has been found before by Winkler [27] and Neumann [114] and is usually linked to a relaxation of strain. Winkler investigated naturally oxidised silicon substrates Si_{ox} and thermally oxidised SiO_2 substrates. For the Si_{ox} he found a deviation from the linear behaviour at $t_{\text{Co}} \leq 1.1$ nm. SiO_2 remained linear. Neumann investigated Si_3N_4 substrates and finds a kink somewhere between $t_{\text{Co}} = 2 - 4$ nm. The deviation from the linear behaviour is usually explained by a relaxation of strain. The large difference in the lattice constants of fcc Co [115] and Pt leads to a mismatch of about 11 % in Co/Pt. A tensile strain is generated in the film plane. This tensile strain increases the out of plane contribution of the anisotropy [39, 40]. Eventually it becomes energetically favourable to decrease the strain by creating dislocations [116] and thereby reducing the out of plane anisotropy. The effect also occurs in Cu/Ni/Cu sandwiches [117].

To further elaborate the point, the change of strain $\Delta\epsilon_{ip}$ is calculated. By using the difference of the volume anisotropy between the lower and the higher thickness regime $\Delta K_V = K_{V,\text{low}} - K_{V,\text{high}}$, $\Delta\epsilon_{ip}$ can be calculated from eq. 2.19:

$$\Delta K_V = \Delta K_{\text{ME}} = B_2 \cdot 1.57 \Delta\epsilon_{ip} \quad (4.10)$$

$B_2 = 7.7 \text{ MJ/m}^3$ is given by Sander [40]. At room temperature this results in a reduction of strain by $\Delta\epsilon_{ip} = 2.6\%$ at room temperature.

In literature a kink is often observed at even smaller Co thickness ($t_{\text{Co}} \leq 1$ nm). A possible reason for such a kink can be found in Takahashi's [118] work about the magneto-strictive strain constants in CoPt alloys. The magneto-elastic coupling constant B_2 is linearly dependent on the magneto-strictive strain constant λ_{111} . Takahashi shows that λ_{111} is depending on the Co content x in the alloy. At $x = 100\%$ λ_{111} , approaches $-20 \cdot 10^{-6}$, which is the same number as given by Sander [40]. However, at $x = 20\%$ λ_{111} approaches zero and consequently the strain anisotropy vanishes. This might apply for samples, where the Co thickness

4.1 Temperature dependence of the anisotropy in ultrathin magnetic films

is smaller than the interdiffusion zone at the interfaces, which results in an alloy $\text{Co}_x\text{Pt}_{1-x}$. Because of this, the perpendicular anisotropy is weakened. However, this effect probably appears only at thinner films, where the Co thickness is smaller than the interdiffusion zone and does not apply to the samples that were investigated in this thesis.

The results for the volume anisotropy K_V on SiO_2 and the higher thickness regime of Si_3N_4 are too small for bulk hcp Co [108]. This is in accordance with the structural investigations of Winkler [27], who found a fcc(111) phase. Suzuki et al. [109] found magneto-crystalline anisotropy constants of $K_{1,cubic} = 62 \text{ kJm}^3$ and $K_{2,cubic} \approx 1 \text{ kJm}^3$ at 300 K for fcc Co film with a cubic anisotropy. Kobs [26] estimated an upper bound for an effectively acting uniaxial anisotropy of $K_V < \frac{1}{3}K_{1,cubic} + \frac{1}{27}K_{2,cubic}$. This gives an upper bound of the volume anisotropy of about 20 kJ/m^3 . This suits the SiO_2 substrate but is too small for the Si_3N_4 substrate. This either implies a mixture of fcc and hcp grains in the film or an additional contribution due to magneto-elastic anisotropy. The mixture of fcc and hcp is unlikely, because Winkler's [27] structural investigation showed otherwise. He performed X-ray diffraction scans of a 50 nm thick Co film and found no characteristics of the hcp phase in the scattering intensity. Therefore, strong magneto-elastic contributions are likely.

4 Magnetisation behaviour of ultrathin magnetic films

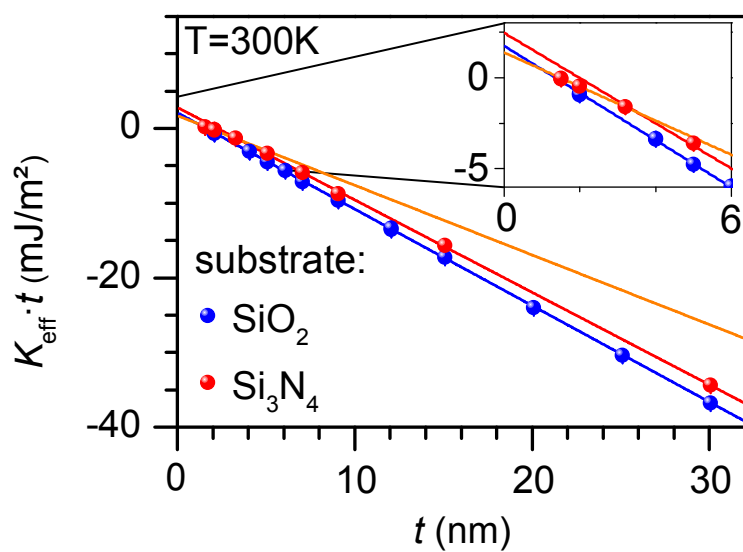


Figure 4.12: The $K_{\text{eff}} \cdot t(t)$ plots of both substrates are compared. Blue represents the SiO_2 substrate, while red stands for the Si_3N_4 substrate. The red line is the fit of the higher thickness regime and the orange line is the fit of the lower thickness regime. The blue line is the fit of the SiO_2 data points.

4.1 Temperature dependence of the anisotropy in ultrathin magnetic films

4.1.5 Discussion

In this chapter possible explanations for the found temperature dependence will be discussed. The decrease of the anisotropy in the thicker films is larger than what is expected from bulk hcp Co as well as fcc Co. The anisotropy at thick films is dominated by the volume anisotropy K_V . As was mentioned in the previous chapter, it is possible that K_V has not only magneto-crystalline contributions but also significant magneto-elastic contributions $K_V = K_{V,MC} + K_{V,ME}$. The change of the volume anisotropy is 114 kJ/m^3 for the SiO_2 substrate and 204 kJ/m^3 for the higher thickness regime of the Si_3N_4 substrate. Assuming the temperature dependence is completely determined by the magneto-elastic anisotropy, the corresponding change in strain can be determined by using eq. 4.10. This results in $\Delta\epsilon_{ip,\text{SiO}_2} = 0.94\%$ and $\Delta\epsilon_{ip,\text{Si}_3\text{N}_4} = 1.69\%$. Using the thermal expansion coefficients ($\alpha_{\text{Co}} = 13 \cdot 10^{-6} \mu\text{m}/(\text{m K}^{-1})$ and $\alpha_{\text{Pt}} = 8.8 \cdot 10^{-6} \mu\text{m}/(\text{m K}^{-1})$ [119]) of Co and Pt a thermally induced change of strain of 0.11% is expected. This is too small to explain the measured temperature dependence. This also rules out the strain as the reason for the increase of the interface anisotropy. This is in accordance to the literature.

Stamps and Louail [120, 121] et al. measured epitaxial grown Co/Pt multilayers with sixfold repetition. Each sample consists of six Co layers ($t_{\text{Co}} = 3.2 \text{ nm}$) that are each separated by a Pt layer. The authors varied the thickness of the Pt layer and found for $t_{\text{Pt}} = 1.5 \text{ nm}$ a decrease of the anisotropy of 170 kJ/m^3 between 20 K and 290 K , which is comparable to the results found in this thesis. Interestingly, for $t_{\text{Pt}} = 1.5 \text{ nm}$ the anisotropy increases between 20 K and 70 K by 110 kJ/m^3 . From 70 K and 290 K the anisotropy decreases by the same value of 110 kJ/m^3 . They explain this behaviour with the emergence and disappearance of cone states, where the magnetisation points neither in plane nor out of plane but lies at an angle in between. The peak of the cone angle overlaps with the peak of the anisotropy.

Other temperature dependent measurements of the anisotropy have been performed by Sugimoto et al. [122], Zhang et al. [123] and Shan et al. [124]. Shan et al. determined the anisotropy of Co/Pt film systems for Co thicknesses that vary between 3 nm and 20 nm . Contrary to the findings in this thesis, the anisotropy decreases with increasing temperature. Between 0.3 nm and 0.5 nm the anisotropy decreases strongly. Above 0.7 nm K_{eff} remains almost constant. They therefore

4 Magnetisation behaviour of ultrathin magnetic films

conclude that the interfaces are the major contribution behind the temperature dependence of the anisotropy.

Sugimoto et al. investigated Co/Pt film systems with a Co layer thickness of 0.4 nm and 0.6 nm. In both cases the anisotropy increases. For 0.6 nm K_{eff} the gain is about 100 kJ/m^3 . The sample exhibits a temperature driven spin-reorientation transition at 150 K. They suggest an increase of the Pt polarisation at low temperatures. Zhang et al. measured Co/Pt film systems where the Co thickness ranges from $t_{\text{Co}} = 0.3 \text{ nm}$ to $t_{\text{Co}} = 2 \text{ nm}$. Above $t_{\text{Co}} = 0.4 \text{ nm}$ the anisotropy increases (or almost stays constant) with increasing temperature. They also determined the temperature dependence of the interface anisotropy. K_{S} increases, which is in accordance to the findings in this thesis. Strain is a possible explanation discussed by the authors. However, there are strong indications that the strain anisotropy is not the mechanism behind the temperature dependence. First, Zhang not only investigated Co/Pt, but also Co/Au film systems. The measurements of Co/Au films do not reveal an increase of the anisotropy. Co/Au poses a comparable strain to Co/Pt. The lattice constant of fcc Co [115] is smaller than of Pt and Au, leading to a lattice mismatch of 11 % for Co/Pt and 14 % for Co/Au. Both systems are almost equally strained, but show an opposite sign of the temperature dependence of the interface anisotropy. This indicates that the strain anisotropy is not an explanation for the increase of the anisotropy. Another look at the thermal expansion coefficients of all materials strengthens this point. The thermal expansion coefficients of Co and Pt $\alpha_{\text{Co}} = 13 \cdot 10^{-6} \mu\text{m}/(\text{m K}^{-1})$ and $\alpha_{\text{Pt}} = 8.8 \cdot 10^{-6} \mu\text{m}/(\text{m K}^{-1})$ [119] evoke a reduction of the strain with rising temperature of about 0.11 %, because Co has a smaller lattice constant than Pt, but a larger expansion factor. A reduction in strain should weaken the perpendicular anisotropy. The thermal expansion coefficient of Au $\alpha_{\text{Au}} = 14.2 \cdot 10^{-6} \mu\text{m}/(\text{m K}^{-1})$ is bigger than of Co, implying an increase of strain in Co/Au with temperature. This contradicts the findings of Zhang et al. [123], who showed that the anisotropy decreases. Therefore, the strain is likely not the cause of the found temperature behaviour.

Without the strain as an explanation, the increase of the anisotropy for small Co layer thickness is counter-intuitive and seems to contradict the laws of thermodynamics. Increasing the temperature destroys the alignment of the magnetic moments and weakens the magnetisation, see eq. 4.1 and 4.2. Consistently, the

4.1 Temperature dependence of the anisotropy in ultrathin magnetic films

bulk anisotropy in hcp Co as well as in fcc Co decreases with rising temperature. However, the decrease of the saturation magnetisation affects not only the crystalline anisotropy but also the shape anisotropy $K_{\text{shape}} = -\frac{1}{2}\mu_0 M_S^2$. Since K_{shape} is an in plane contribution of the anisotropy, a decrease will strengthen the out of plane anisotropy. This is a relatively strong effect, despite the small relative change of M_S , which is about 1%. It stems from the quadratic- M_S dependence of the shape anisotropy. This is contrary to eq. 4.3, that was used to experimentally determine the anisotropy. The found anisotropies as well as the shape of the temperature dependence are relatively unaffected by $M_S(T)$. In fact, the results do not fundamentally differ even when doing the analysis with a constant M_S . Using $M_S(T)$ given by Kuz'min (eq. 4.2), the difference between the shape anisotropy at 2.5 K and 300 K is determined. It follows $\Delta K_{\text{shape}} = K_{\text{shape}}(2.5 \text{ K}) - K_{\text{shape}}(300 \text{ K}) = 27 \text{ kJ/m}^3$. However, for $t_{\text{Co}} = 2 \text{ nm}$ grown on SiO_2 the effective anisotropy is increased by $\Delta K_{\text{eff}} = 77 \text{ kJ/m}^3$. The thermally induced decrease of the shape anisotropy is too small to explain the increase of the effective anisotropy.

For a possible explanation, a closer look at the composition of the samples must be made. The transition between the Pt and Co occurs not stepwise but is smeared out. An interdiffusion zone arises, where the Pt and Co form a $\text{Co}_x\text{Pt}_{1-x}$ alloy. The conventional method to determine the anisotropy assumes perfect interfaces. The Co thickness is equivalent to the nominal Co thickness t_{nom} , that is defined by the deposited material. However, it will be shown that the ferromagnetic effective Co thickness is smaller, due to the alloying at the interfaces. To simplify the model both intermixing zones are summed up to one interface and it is assumed that the Co concentration is distributed linearly along the length of the interface. The model is shown and explained in fig. 4.13.

Both intermixing zones were found to have a thickness of 0.7 nm, making it $t_{\text{int}} = 1.4 \text{ nm}$ in total [27]. The pure Co thickness that is not affected by the interface is given by $t_{\text{nom}} - t_{\text{int}}/2$, where t_{nom} is the nominal Co thickness, that was expected from the deposited material. For the case of a nominal Co thickness of $t_{\text{nom}} = 2 \text{ nm}$ the pure Co thickness would be given by $t_{\text{nom}} - t_{\text{int}}/2 = 1.3 \text{ nm}$. The remaining 0.7 nm of Co are linearly distributed among the 1.4 nm of the interdiffusion zone and form an alloy with Pt.

The thickness of the interdiffusion zone proved to be independent of the nominal Co thickness, thus the importance of the interface decreases with higher nominal

4 Magnetisation behaviour of ultrathin magnetic films

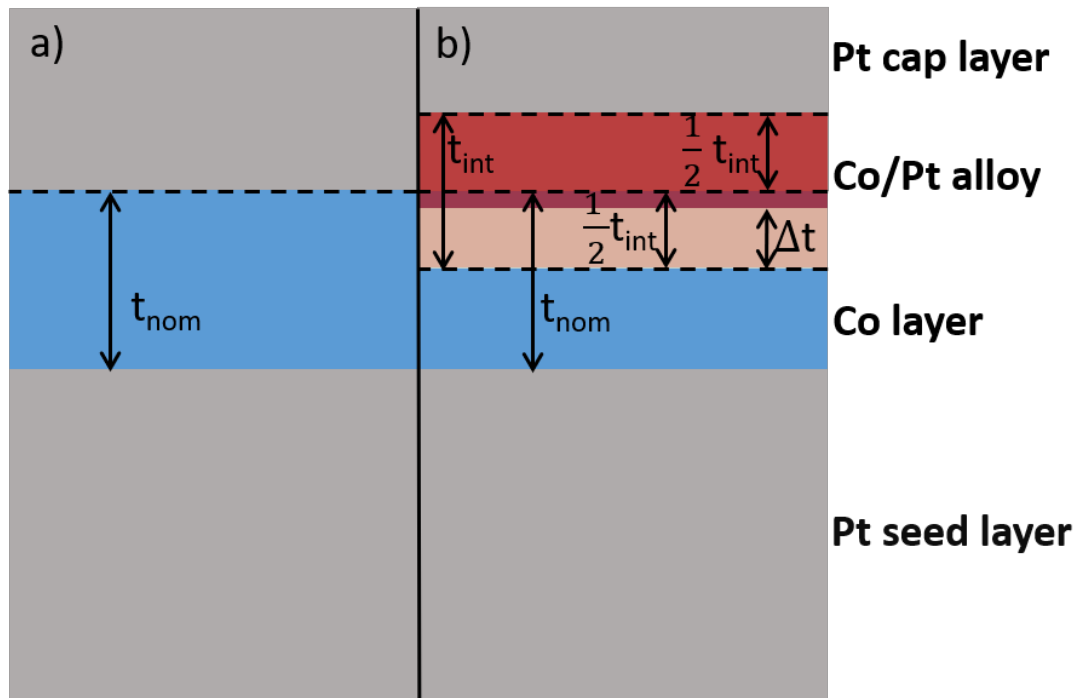


Figure 4.13: The model of the interdiffusion zone in ultrathin films is shown. a) A film with perfect interfaces. The blue box represents the Co layer and the silver boxes the Pt seed and cap layer. The nominal Co thickness t_{nom} is determined by the sputtering rate. b) Instead of perfect interfaces an interdiffusion zone (thickness t_{int}) emerges, where Co and Pt form an alloy. For simplification both interfaces are treated as one and it is assumed that the $t_{\text{nom}} - \frac{1}{2}t_{\text{int}}$ of Co are distributed linearly over the interdiffusion zone. At the interface between the Co layer and Co/Pt alloy the Co concentration is 100% and at the interface between the Co/Pt alloy and the Pt cap layer the Co concentration is 0%. Below a threshold Co concentration, the alloy will not be ferromagnetic, which leads to an effective Co thickness that is given by $t_{\text{nom}} - \frac{1}{2}t_{\text{int}} + \Delta t$.

4.1 Temperature dependence of the anisotropy in ultrathin magnetic films

Co thickness. As is mentioned above, it is assumed that the concentration of Co x grows linearly along the interface. x will be 0 at the interface between the Pt cap layer and the $\text{Co}_x\text{Pt}_{1-x}$ alloy and 100% at the interface between the $\text{Co}_x\text{Pt}_{1-x}$ alloy and the Co layer. As the Co concentration is reduced, so will be the Curie temperature T_C . Below a threshold Co concentration x_L , the alloy will not be ferromagnetic, because T_C is smaller than the temperature at which the experiment is conducted. This leads to an effective Co thickness $t_{\text{nom}} - \frac{1}{2}t_{\text{int}} + \Delta t(T)$. The latter is the part of the interdiffusion zone, that is ferromagnetic at the temperature T . Taking these considerations into account, a new anisotropy model can be defined:

$$K_{\text{eff}} \cdot t_{\text{nom}} = K_V^I \left(t_{\text{nom}} - \frac{t_{\text{int}}}{2} \right) + K_V^* \cdot \Delta t + K_{\text{shape}} \left(\frac{t_{\text{nom}} - \frac{t_{\text{int}}}{2} + \Delta t}{t_{\text{nom}}} \right)^2 \cdot t_{\text{nom}} + 2K_S^I \quad (4.11)$$

K_V^I and K_S^I are the volume and surface anisotropy in the model and K_V^* is the volume anisotropy of the CoPt alloy in the interdiffusion zone. The terms K_V and K_S , that were determined with the conventional method in the previous chapter, are actually composed of K_V^I respectively K_S^I and additional terms. To use the model, $\Delta t(T)$ needs to be determined. Therefore, $T_C(x)$ needs to be discussed. For bulk Co T_C has a value of 1385 K [96]. The values of the alloys are given by Crangle and Parsons [125] as well as Crangle and Scott [126] and Sanchez [127]. At a Co concentration of 85.2%, T_C is reduced to 1261 K [125] and at 10.2% T_C falls below room temperature to 218 K. Fig. 4.14 (b) shows the Curie temperature $T_C(x)/T_{C,\text{bulk}}$ over the Co content. When measuring at 300 K every part of the interface, where the Co content is less than $x_L = 14.3\%$, will not be ferromagnetic, because T_C lies below 300 K.

Due to $T_C(x)$, Δt will increase at lower temperatures, because more parts of the interface are ferromagnetic. For example at 50 K the threshold for ferromagnetism lies at a Co content of 2.9%. Importantly Δt is not only temperature dependent, but also the saturation magnetisation is reduced. Fig. 4.14 (c) shows the reduced magnetisation M/M_S over the Co content. At 100% the reduced magnetisation is at a maximum of 1. For 15% it lies at 0.27 and for 5% at 0.1. Due to the distribution of the $t_{\text{int}}/2 = 0.7$ nm Co over the interface, the saturation magnetisation of Δt Co is smaller than that of the pure Co ($t_{\text{Co,pure}} = t_{\text{nom}} - t_{\text{int}}/2$). Taking this into account a model is developed to calculate the magnetisation of Δt in dependence of the temperature.

4 Magnetisation behaviour of ultrathin magnetic films

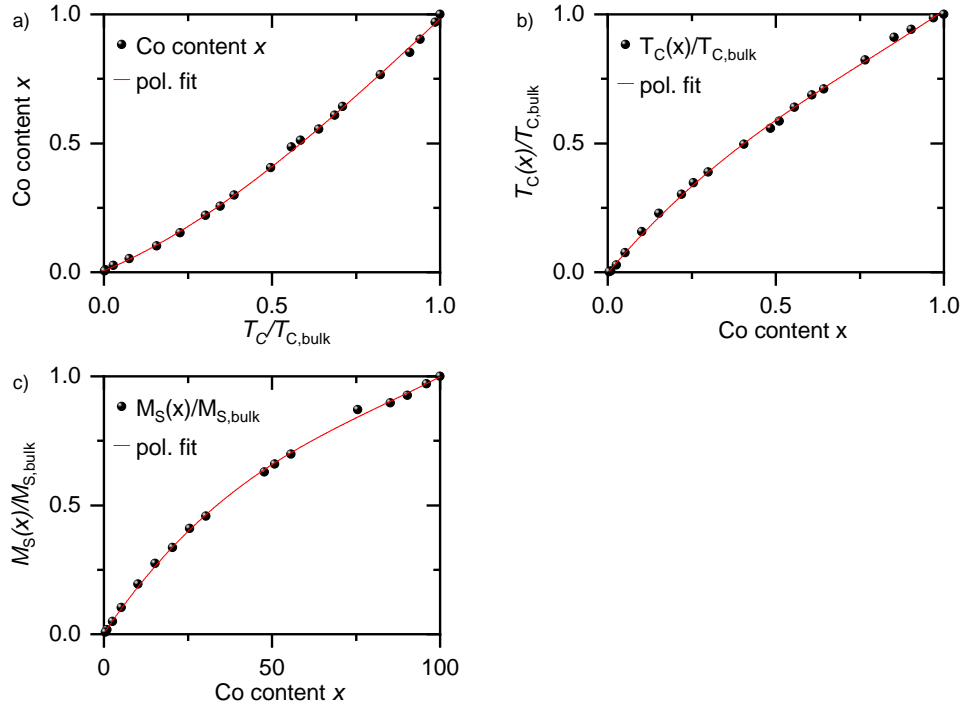


Figure 4.14: a) shows the Co content x over $T_C/T_{C,bulk}$, b) the opposite plot $T_C(x)/T_{C,bulk}$ and c) $\frac{M_S(x,T)}{M_{S,bulk}}$. The data points are taken from [125–127]. T_C and M_S are dependent on the Co content and decrease with decreasing x . The red lines are polynomial fits that are shown in eq. 4.17, eq. 4.15 and eq. 4.16.

4.1 Temperature dependence of the anisotropy in ultrathin magnetic films

The saturation magnetisation $M_S(x, T)$ is dependent on the Co concentration x and the the temperature T . This can be separated into a temperature independent term $M_S(x, 0\text{K})$ and a temperature dependent term $f\left(\frac{T}{T_C(x)}\right)$:

$$M_S(x, T) = M_S(x, 0\text{K}) \cdot f\left(\frac{T}{T_C(x)}\right) \quad (4.12)$$

The term $T_C(x)$ is the Curie temperature, that is also dependent on the Co concentration x . For convenience the expression above, will be rescaled by the saturation magnetisation of bulk Co $M_{S,\text{bulk}}$:

$$\frac{M_S(x, T)}{M_{S,\text{bulk}}} = \frac{M_S(x, 0\text{K})}{M_{S,\text{bulk}}} \cdot f\left(\frac{T}{T_C(x)}\right) \quad (4.13)$$

For the temperature dependence of the magnetisation $f\left(\frac{T}{T_C(x)}\right)$, the expression given by Kuz'min [96] is used (see eq. 4.2):

$$f\left(\frac{T}{T_C(x)}\right) = \frac{M_S(x, T)}{M_S(x, 0\text{K})} = \left[1 - 0.11 \cdot \left(\frac{T}{T_C(x)}\right)^{3/2} - (1 - 0.11) \cdot \left(\frac{T}{T_C(x)}\right)^{5/2} \right]^{1/3} \quad (4.14)$$

The terms $\frac{T_C(x)}{T_{C,\text{bulk}}}$ and $\frac{M_S(x)}{M_{S,\text{bulk}}}$ are obtained by fitting polynomial functions to the data seen in fig. 4.14. Polynomial functions of the third order are fitted to the data points and scaled over the bulk values $T_{C,\text{bulk}}$ and $M_{S,\text{bulk}}$:

$$\frac{T_C(x)}{T_{C,\text{bulk}}} = -0.003 + 1.6 \cdot x - 0.9 \cdot x^2 + 0.4 \cdot x^3 \quad (4.15)$$

$$\frac{M_S(x)}{M_{S,\text{bulk}}} = 0.003 + 1.9 \cdot x - 1.5 \cdot x^2 + 0.6 \cdot x^3 \quad (4.16)$$

$M = \frac{M_S(x, T)}{M_{S,\text{bulk}}}$ is plotted in fig 4.15 for 300 K and 10 K against the Co content x . The magnetisation is reduced with lower Co content. At a threshold concentration x_L the magnetisation disappears, because T_C is below the temperature at which the experiment was conducted. This threshold is 12.5 % at 300 K and below 2% at 10 K.

In Fig. 4.14 (a) the reverse of Fig. 4.14 (b) is shown, which is the Co concentration x in dependence of the Curie temperature. By fitting a polynomial function,

4 Magnetisation behaviour of ultrathin magnetic films

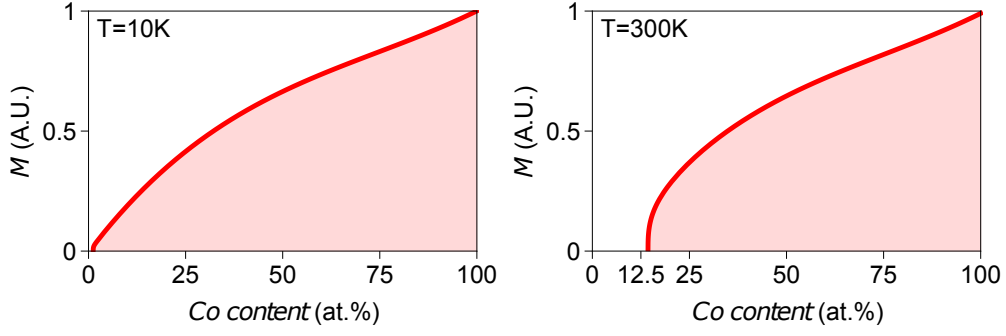


Figure 4.15: The plot shows $M = \frac{M_S(x,T)}{M_{S,\text{bulk}}}$ for 10 K and 300 K. The magnetisation decreases with decreasing Co content. At 300 K the magnetisation is cut off slightly above $x = 12.5\%$. This stems from the fact that T_C is smaller than 300 K at this point. The alloy is no longer ferromagnetic. The amount of magnetic moments that are active in the interdiffusion zone can be determined by integrating both plots.

$x(T_C)$ can be obtained. At low Co concentrations x , the Curie temperature T_C may fall beneath the experimental temperature, hence the temperature at which the measurements are performed. Above T_C the sample becomes paramagnetic. This will define a lower limit x_L of Co concentration that is still ferromagnetic at the measured temperature. This lower limit is given by the polynomial fit mentioned above and results in:

$$x_L(T) = 0.8 + 0.04 \cdot T + 0.8 \cdot 10^{-5} \cdot T^2 + 10 \cdot 10^{-9} \cdot T^3 \quad (4.17)$$

x_L is plotted in fig. 4.16, on the left hand side.

With the above mentioned expressions, the factor $r(T)$ can be determined, which gives the number of magnetic moments, that are active in the interdiffusion zone. It is given by the following integral:

$$r(T) = \int_{x_L}^1 \frac{M_S(x, 0 \text{ K})}{M_{S,\text{bulk}}} \cdot f\left(\frac{T}{T_C(x)}\right) dx \quad (4.18)$$

The factor r is plotted in fig. 4.16, on the right hand side. Under the assumption, that the magnetic moments are distributed linearly over the interdiffusion zone, the ferromagnetic part of the interdiffusion zone $\Delta t(T)$ can be determined by $\Delta t(T) = r(T) \cdot t_{\text{int}}/2$. The reduction of the magnetisation is given by:

$$M_S(T) = \left(\frac{t_{\text{nom}} - t_{\text{int}}/2 + \Delta t(T)}{t_{\text{nom}}} \right) \cdot M_{S,\text{bulk}} \quad (4.19)$$

4.1 Temperature dependence of the anisotropy in ultrathin magnetic films

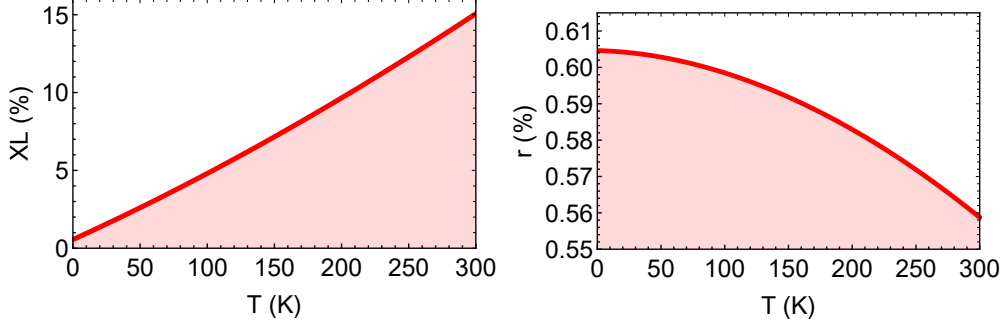


Figure 4.16: The left graph, shows $x_L(T)$, which is the threshold Co content. Above x_L the alloy is ferromagnetic. The right graph, shows the factor r , that is the amount of active magnetic moments in the alloy in respect to the bulk value. r can be used to determine the effective ferromagnetic thickness of the interdiffusion zone, which is given by $\Delta t = r \cdot t_{\text{int}}/2$.

Considering a nominal Co thickness of $t_{\text{nom}} = 2 \text{ nm}$ and $t_{\text{int}}/2 = 0.7 \text{ nm}$, the expression $\left(1 - \frac{0.7 - \Delta t(T)}{t_{\text{nom}}}\right)$ amounts to 0.862 at 10 K and 0.846 at 300 K. This difference between the two temperatures magnifies when looking at the shape anisotropy:

$$\frac{\mu_0}{2} \cdot M_S^2(T) = \left(1 - \frac{0.7 - \Delta t(T)}{t_{\text{nom}}}\right)^2 \cdot \frac{\mu_0}{2} \cdot M_{S,\text{bulk}}^2 \quad (4.20)$$

The shape anisotropy is reduced to 0.743 of the bulk shape anisotropy at 10 K and to 0.716 at 300 K. The shape anisotropy is reduced by $\Delta K_{\text{shape}} = 37 \text{ kJ/m}^3$ from 10 K to 300 K. Since the shape anisotropy is an in-plane contribution, a reduction strengthens the out-of-plane contribution of the effective anisotropy, thus giving another reason why the effective anisotropy increases with rising temperatures. The term $g^2 = \left(1 - \frac{0.7 - \Delta t(T)}{t_{\text{nom}}}\right)^2$ is plotted against the temperature in fig. 4.17 a). The nominal Co thickness is varied, to visualise the decreasing strength of the effect with a higher thickness. At 20 nm the line is almost horizontally, while at 0.7 nm a steep decrease is visible. This amounts to a reduction of K_{shape} of $\Delta K_{\text{shape},20 \text{ nm}} = 8 \text{ kJ/m}^3$, $\Delta K_{\text{shape},5 \text{ nm}} = 16.5 \text{ kJ/m}^3$, $\Delta K_{\text{shape},2 \text{ nm}} = 37 \text{ kJ/m}^3$ and $\Delta K_{\text{shape},0.7 \text{ nm}} = 71 \text{ kJ/m}^3$. To further stress the point the anisotropy model is further discussed.

The anisotropy model (eq. 4.11) can be rewritten as:

4 Magnetisation behaviour of ultrathin magnetic films

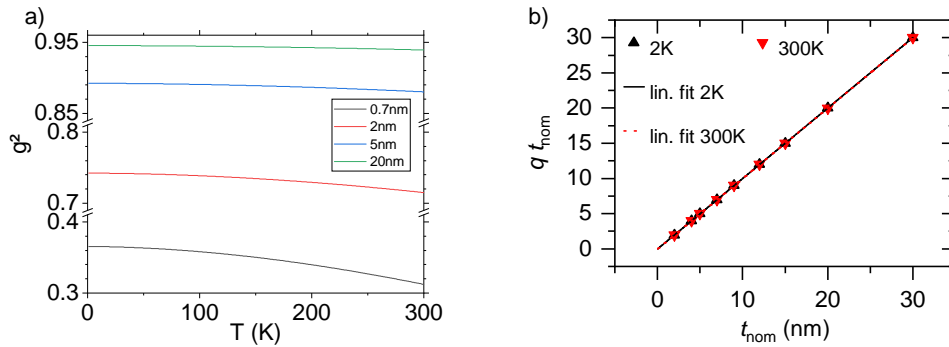


Figure 4.17: a) shows the factor $g^2 = \left(\frac{t_{\text{nom}} - t_{\text{int}}/2 + \Delta t(T)}{t_{\text{nom}}} \right)^2$ for different Co thickness. g^2 gives the reduction and temperature dependence of the saturation magnetisation. With increasing thickness, the temperature dependence vanishes and bulk properties are approached. For smaller thickness the reduction of M_S increases as well as the temperature dependence. The change of shape anisotropy is K_{shape} of $\Delta K_{\text{shape},20\text{nm}} = 8\text{ kJ/m}^3$, $\Delta K_{\text{shape},5\text{nm}} = 16.5\text{ kJ/m}^3$, $\Delta K_{\text{shape},2\text{nm}} = 37\text{ kJ/m}^3$ and $\Delta K_{\text{shape},0.7\text{nm}} = 71\text{ kJ/m}^3$. b) shows the correction factor $q = \left(1 + \left[\frac{0.7 - \Delta t}{t_{\text{nom}}} \right]^2 \right)$ of the shape anisotropy, when determining the volume anisotropy from the $K_{\text{eff}} \cdot t(t)$ plot. Both temperatures yield almost the same result and the temperature dependence is negligible. By fitting linear equations, the correction of the shape can be determined from the slopes. This amounts to 1.0009 at 2 K and 1.0011 at 300 K, which is below 0.1%. Therefore, the influence of the alloying at the interfaces on the determination of the volume anisotropy is negligible.

4.1 Temperature dependence of the anisotropy in ultrathin magnetic films

$$K_{\text{eff}} \cdot t_{\text{nom}} = \left(K_V^I + K_{\text{shape}} \left[1 + \frac{\left(\frac{t_{\text{int}}}{2} + \Delta t \right)^2}{t_{\text{nom}}^2} \right] \right) \cdot t_{\text{nom}} - \left(2K_{\text{shape}} + K_V^I \right) \cdot \frac{t_{\text{int}}}{2} + (2K_{\text{shape}} + K_V^*) \Delta t + 2K_S^I \quad (4.21)$$

Compared to the conventional model, that assumes sharp interfaces and that is given by $K_{\text{eff}} \cdot t = (K_V + K_{\text{shape}}) \cdot t + 2K_S$, two additional contributions appear. The first part in the upper line, can be understood as the slope in the $K_{\text{eff}} \cdot t(t)$ plot. The shape anisotropy is corrected by an additional factor. The second part in the lower line, is the intercept in the $K_{\text{eff}} \cdot t(t)$ plot. Both parts are dependent on $\Delta t(T)$. For simplification, the volume anisotropy of Co and the $\text{Co}_x\text{Pt}_{1-x}$ alloy will be treated as equally $K_V^I = K_V^*$.

The term $\left(1 + \left[\frac{0.7 - \Delta t}{t_{\text{nom}}} \right]^2 \right) \cdot t_{\text{nom}}(t_{\text{nom}}) = q \cdot t_{\text{nom}}(t_{\text{nom}})$ is plotted in fig. 4.17 b) for 2 K and 300 K. The data points are almost undistinguishable and fits of linear equations yield almost identical results. The slope of the linear equations are 1.0009 at 2 K and 1.0011 at 300 K, which shows that the correction of K_{shape} is smaller than 0.1%. The temperature dependence is even smaller. Therefore, the effect of the interface on the slope and hence on the determination of the volume anisotropy is negligible and the usual approach, that has been used in this thesis, is sufficient. It follows $K_V \approx K_V^I$

The second part of eq. 4.21 is the intercept, where an additional contribution appears. It follows $2K_S = (2K_{\text{shape}} + K_V) \cdot \left(-\frac{t_{\text{int}}}{2} + \Delta t \right) + 2K_S^I$. However, the effect is not big enough to fully explain the temperature dependence of the interface anisotropy. In fig. 4.18, K_S , the correction term $K_S^C = 0.5 \cdot (2K_{\text{shape}} + K_V) \cdot \left(-\frac{t_{\text{int}}}{2} + \Delta t \right)$ and K_S^I are plotted and linear equations are fitted to the data points. Slopes of 500 mJ/(Km²), 170 mJ/(Km²) and 330 mJ/(Km²) are found. Though the model cannot fully explain the complete temperature dependence of the interface anisotropy, it could be shown that the alloying at the interfaces has a strong contribution and that the conventionally determined interface anisotropy K_S is strongly overestimated.

According to the model, a further reduction of the Co thickness should manifest in an even stronger slope of the temperature dependence. In the next chapter measurements of a film with a nominal thickness of 0.7 nm will be presented. At this thickness the magnetisation points out of the film plane. In this case, the method that is used so far is no longer feasible.

4 Magnetisation behaviour of ultrathin magnetic films

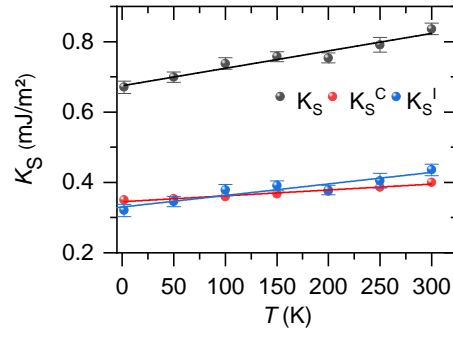


Figure 4.18: The graph shows the interface anisotropy K_S that was determined for SiO_2 . Under the consideration of the alloying at the interfaces, the true interface anisotropy K_S^I is determined. The correction term K_S^C is an offset in the intercept. Due to this the interface anisotropy is overestimated when sharp interfaces are assumed. The lines are fits of linear equations. The slopes amount to $500 \text{ mJ}/(\text{Km}^2)$, $170 \text{ mJ}/(\text{Km}^2)$ and $330 \text{ mJ}/(\text{Km}^2)$ for K_S , K_S^C and K_S^I . However, the temperature dependence of the interface anisotropy cannot be fully explained by the model.

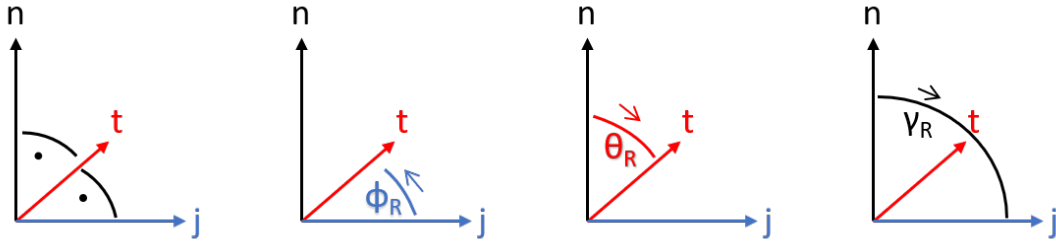


Figure 4.19: An explanation of the measurement geometry. n is the film normal, j is the direction of the applied current and t is the axis perpendicular to both. Magnetic field sweeps in the direction of n are called polar sweeps, in the direction of j longitudinal sweeps and in the direction of t transversal sweeps. The angles between the axes are defined as $\phi_R \angle(j, t)$, $\theta_R \angle(n, t)$ and $\gamma_R \angle(n, j)$. Rotational measurements in respect to the different angles can be performed by rotating the sample.

4.2 Magneto-transport measurements

So far relatively simple measurements of the transversal resistance have been made to determine the anisotropy. The method is only feasible in magnetic films that possess an in-plane magnetisation, where the easy axis of magnetisation is perpendicular to the film normal. In this chapter a sample with an out-of-plane magnetisation is investigated, needing more complex measurements of the longitudinal resistance. The measurement geometry (see fig. 4.19) is defined by the film normal n , which is also the easy axis of magnetisation, the applied electric current j and the axis that is perpendicular to both $t \perp (j, n)$. Magnetic field sweeps in the direction of n are called polar sweeps, in the direction of j longitudinal sweeps and in the direction of t transversal sweeps. By applying strong magnetic fields, the magnetisation will be rotated parallel to the field direction until it is aligned at technical saturation. The angles between the axes are defined as $\phi_R \angle(j, t)$, $\theta_R \angle(n, t)$ and $\gamma_R \angle(n, j)$. The response of the resistance to the different angles can be probed, by rotating the sample inside a static magnetic field. The strength of the magnetic field is set to a point, where the sample is in technical saturation. Usually 6 T are used.

4.2.1 Anisotropy in films with perpendicular magnetic anisotropy

To further understand the influence of the intermixing zone, the Co thickness is decreased to a point where the intermixing zone is larger than the Co layer

4 Magnetisation behaviour of ultrathin magnetic films

itself, thus creating effectively an alloy. The easy axis of magnetisation now lies perpendicular to the film plane. The determination of the anisotropy in films with an out of plane easy axis turns out to be more difficult, as the above measurements are not hard axis field sweeps but easy axis field sweeps. Therefore the longitudinal resistance is measured instead of the Hall resistance with the magnetic field in the plane of the film. Unfortunately the longitudinal resistance will not mirror the rotation of the magnetisation, because of magnetoresistance effects, namely the anisotropic MR (AMR). This effect is dependent on the angle ϕ_{AMR} between the direction of the magnetisation and the electric current in the film and is described by $R = R_{\perp} + (R_{\parallel} - R_{\perp}) \cos^2(\Phi)$.

$R_{\parallel} - R_{\perp} = \Delta R_{AMR}$ is also called the AMR-ratio. To determine the anisotropy, a relation between the AMR and the anisotropy needs to be defined. This relation can be derived from the energy potential of the uniaxial anisotropy (eq. 2.21) with $\phi = 90^\circ$. The angle $\theta \angle(E.A., M)$ can be substituted with $90^\circ - \Phi \angle(M, j)$. This is possible, because the easy axis of magnetisation is parallel to the film normal and the electric current is perpendicular to the film normal. With the substitution $\sin(\theta) = \cos(\Phi) = \frac{M_{\parallel}}{M_S} = \frac{\mu_0 M_S H}{2K}$ can be determined. The new expression links the AMR to the anisotropy:

$$R = R_{\perp} + \Delta R_{AMR} \left(\frac{M_S}{2K} \right)^2 (\mu_0 H)^2 \quad (4.22)$$

An exemplary measurement can be seen on the left hand side of fig. 4.20. The magneto-resistance is plotted against the magnetic field. The measurement was performed at 290 K. The sample is sputtered on a SiO₂ substrate with a nominal Co thickness of 0.7 nm. The inset shows the raw measurement. Above technical saturation at ± 1 , T a linear decrease of the magneto-resistance signal appears. This behaviour is caused by the spin disorder magneto-resistance (SMR) and needs to be corrected in order to correctly determine the anisotropy. The corrected measurement is the main part of the figure. Additionally to the elimination of the linear response, the offset has been subtracted from the magneto-resistance. Due to this, ΔR_{xx} becomes zero above technical saturation, thus simplifying the determination of the anisotropy. Likewise to the previous chapter, the saturation magnetisation $M_S = 1.458$ kA/m given by Crangle [48] is used in combination with the temperature dependence described by Kuz'min [96]. For the depicted

4.2 Magneto-transport measurements

measurement an anisotropy constant of $(300 \pm 1) \text{ kJ/m}^3$ is found.

The anisotropy is determined for a broad temperature window, ranging from 2.5 K to 300 K. The result is displayed on the right hand side of fig. 4.20. The results verify the findings of the previous chapter. The anisotropy increases with rising temperatures. Between 2.5 K and 250 K a linear behaviour can be seen. From the fit of a linear equation $\frac{dK_{\text{eff}}}{dT} = (550 \pm 16) \frac{\text{J}}{\text{m}^3\text{K}}$. This is higher than what was found in the previous chapter by almost a factor of two. However, the Co layer thickness (0.7 nm) is significantly smaller than in the previous chapter. The thinnest Co layer of the previous chapter is 1.5 nm. Above 250 K the anisotropy reaches a plateau and remains constant. Like the interface anisotropy, the anisotropy increases with increasing temperature. This could imply that the found temperature dependence of the anisotropy mirrors the temperature dependence of the interface anisotropy. This makes sense, as the thickness of the Co layer is smaller than the intermixing zone. The sample is basically an CoPt alloy and the temperature dependence is unaffected by the volume anisotropy.

In a second sample the method to determine the anisotropy failed, as an unexpected behaviour appeared in the longitudinal field sweeps. The sample is sputtered on a SiO_2 substrate and has a 5 nm Pt seed layer, a nominal Co thickness of 1 nm and a 3 nm Pt cap layer. Four measurements at different temperatures are shown in fig. 4.21. The behaviour will be discussed in the following chapter.

4 Magnetisation behaviour of ultrathin magnetic films

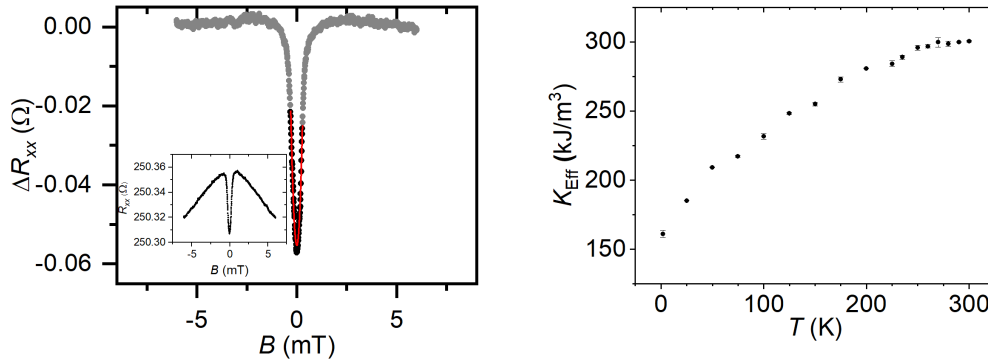


Figure 4.20: The temperature dependence of the anisotropy is determined for a Pt/Co/Pt film sputtered on a SiO₂ substrate. The Pt seed layer has a thickness of 7 nm, the nominal Co thickness is 0.7 nm and the Pt cap layer is 3 nm.

On the left hand side, a longitudinal sweep measurement of the magneto-resistance is shown. In the inset the raw measurement is shown. Between roughly 1 T and -1 T the parabola shape of the AMR can be seen. Above technical saturation, the SMR becomes dominant, resulting in a linear decrease of the magneto-resistance. For the fit the SMR is corrected and the offset is subtracted from the data, as can be seen in the main graph. The red line depicts the fit to determine the anisotropy. The measurement of this particular measurement were performed at 290 K. A broad temperature range has been investigated.

On the right hand side, the determined anisotropy is plotted against the temperature. Between 2.5 K and 250 K a linear increase can be observed. From 250 K onwards a plateau is reached and the anisotropy remains almost constant. The slope of the temperature dependence is $(550 \pm 16) \frac{\text{J}}{\text{m}^3\text{K}}$ between 2.5 K and 250 K.

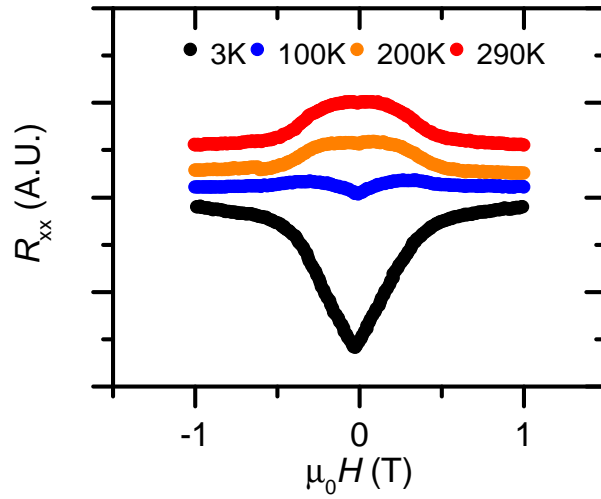


Figure 4.21: A second sample has been investigated. The Pt/Co/Pt film sputtered on a SiO₂ substrate. The Pt seed layer has a thickness of 5 nm, the nominal Co thickness is 1 nm and the Pt cap layer is 3 nm. Longitudinal magnetic field sweeps have been performed. The graph shows the obtained magneto-resistance curves. Four temperatures can be seen 3 K, 100 K, 200 K and 290 K. The abscissa is set to range from -1 T to 1 T in order to focus on effect occurring close to zero field. Originally, the behaviour seen in fig. 4.20 is expected. With rising field strength the magnetisation rotates from the film normal (the easy axis of magnetisation) into the film plane. While doing so the anisotropic magneto-resistance occurs and a parabola like shape can be observed in the magneto-resistance curve. This is only the case at 3 K. At 100 K only a very small effect is visible. At 200 K and 290 K another parabola like shape appears, however with the opposite sign. This unexpected behaviour will be discussed in the next chapter, see sec. 4.2.2. The behaviour makes it impossible to determine the anisotropy from longitudinal sweeps. Instead transversal sweeps are performed.

4.2.2 Change of longitudinal resistance

Due to the behaviour found in fig. 4.21, the sample with a nominal Co thickness of 1 nm has been further investigated. Longitudinal, transversal and polar field sweeps were performed at 3 K, 100 K, 200 K and 290 K. The results are shown in fig. 4.22. All measurements can be separated into two parts: A high field behaviour above technical saturation and a low field behaviour, where the magnetisation is rotated due to the external magnetic field. The high field behaviour is dominated by two effects, the ordinary (Lorentz) magnetoresistance at 3 K and the spin wave disorder magnetoresistance at higher temperatures. The Lorentz magnetoresistance results in an increase with higher magnetic fields. In literature

4 Magnetisation behaviour of ultrathin magnetic films

one can also find an increase due to the spin wave disorder magnetoresistance at low temperatures.

Above 3 K the resistance decreases due to the annihilation of spin wave and therefore less electron magnon scattering. Below technical saturation the behaviour is dependent on the measurement geometry. In the polar geometry the magnetisation lies parallel to the magnetic field and the magnetoresistance remains constant except for the SMR. In the transversal geometry parabolic behaviour is found. With increasing field strength the magnetisation is rotated into the film plane. Due to the anisotropic interface magnetoresistance a parabolic behaviour emerges in the longitudinal resistance. In the longitudinal geometry the aforementioned unexpected behaviour is found. At 3 K a parabolic behaviour is found, analogous to the transversal geometry but with an opposite sign of the opening. At 200 K and 290 K the parabola has a different sign than at 3 K. Also the parabola is broader and the magnitude is smaller. 100 K seems to be an intermediate case. To better understand this unexpected behaviour, rotational measurements have been made. These are shown in fig. 4.23 and were done at the same temperatures as the previous measurements. Two geometries were used. The red curves show the θ -rotation, which is the out of plane rotation from the film normal to the film plane. In this case the rotation axis is perpendicular to the direction of the current. The blue curves show the ϕ_R -rotation. This is the in-plane rotation, where the magnetic field is rotated from a parallel alignment to a perpendicular alignment in respect to the current direction. The θ_R -rotation is sensitive to the anisotropic interface magnetoresistance (AIMR) and the ϕ_R -rotation to the regular anisotropic magnetoresistance (AMR). At 3 K the magnitude of the AMR is significant higher than the AIMR, which fits to the behaviour found in previous works [26]. This changes already at 100 K, where both AMR and AIMR have roughly the same magnitude. At 200 K the AMR is smaller than the AIMR, which becomes even more pronounced at 290 K. The AMR can be described by a $\cos^2(\phi_R)$ -fit, which is represented by the blue lines in fig. 4.23. As can be seen, the fit represents very well the measurement data. The dashed red lines show a $\cos^2(\theta_R)$ -fit to AIMR, which does not fit very well. This is the result of higher orders that are prominent in the AIMR. Due to this, the red line shows a fit, that includes also the second and third order, which than fits very well. A quantitative analysis of the magnitude of the AMR and AIMR can be found in fig. 4.24. Here the change

4.2 Magneto-transport measurements

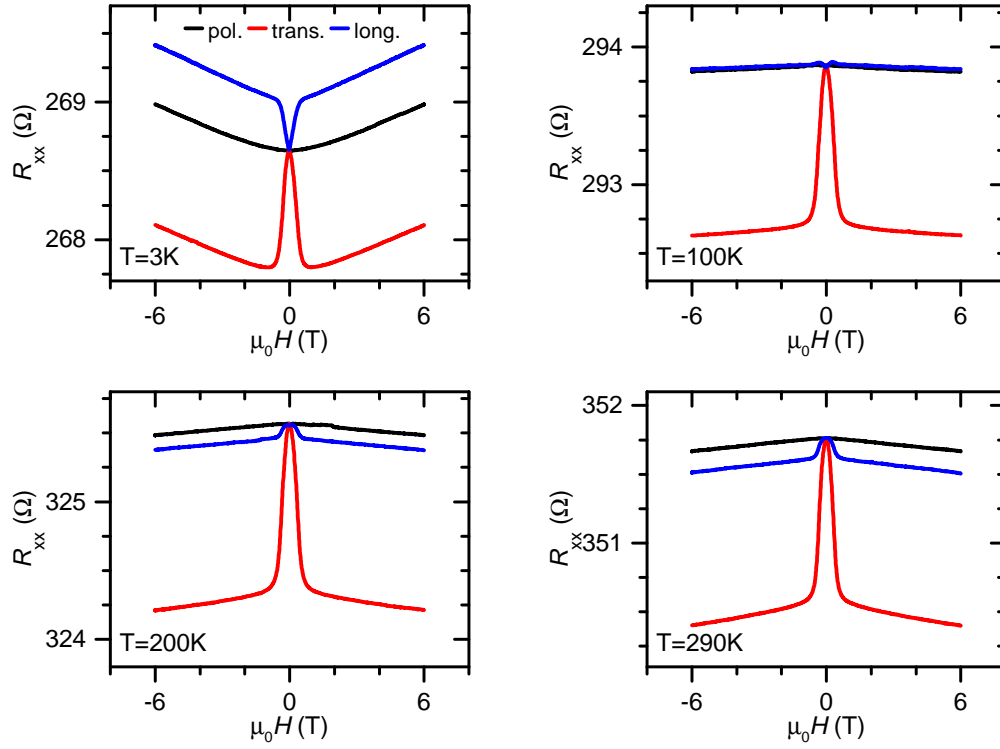


Figure 4.22: Polar, longitudinal and transversal field sweeps are shown at different temperatures. The behaviour at 3 K is in accordance with results of previous investigations [26]. At 100 K the parabola in the longitudinal sweep disappears. Above 200 K a new parabola emerges. However, the opening has a different sign. The polar and transversal sweep are not altered by the temperature, except above technical saturation, where the SMR can be seen.

4 Magnetisation behaviour of ultrathin magnetic films

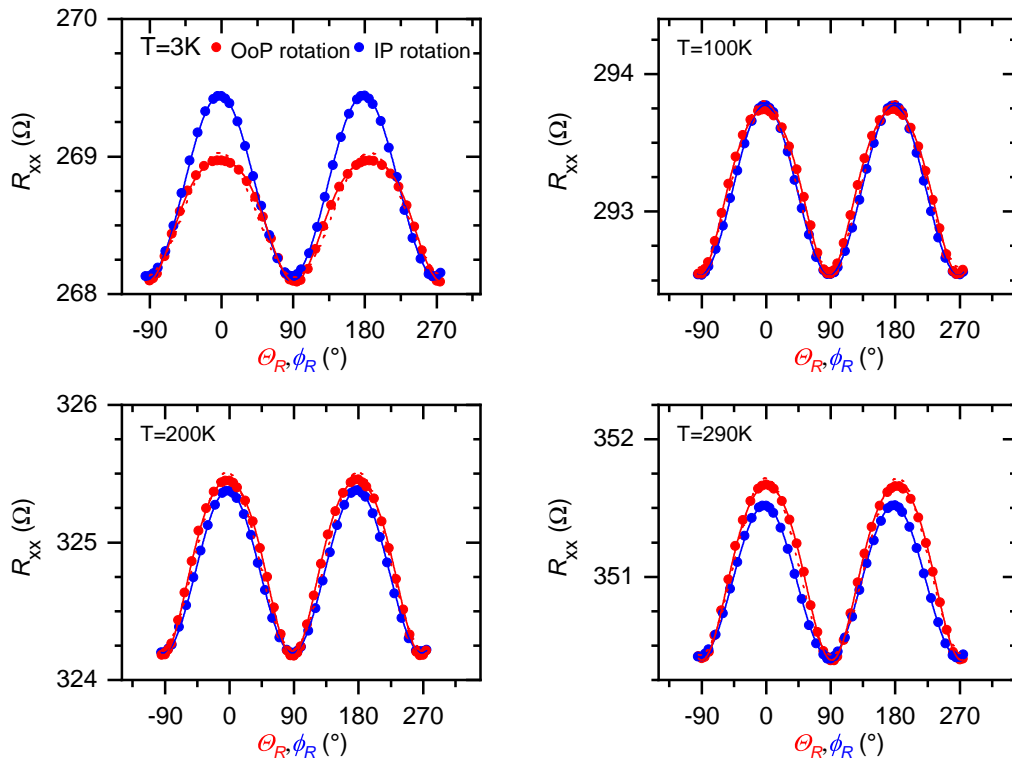


Figure 4.23: Rotational measurements with a magnetic field of 6T applied in the plane (ip) and out of the plane (oop) of the film at different temperatures. While the magnitude of the in-plane rotation decreases, the out-of-plane rotation increases.

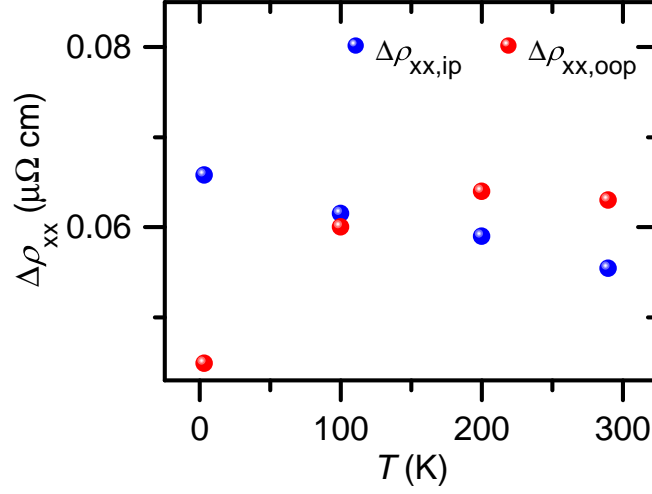


Figure 4.24: The figure shows the magnitude of the rotational measurements $\Delta\rho_{xx}$. The in-plane rotation decreases linearly and the out-of-plane rotation increases. At 100 K they are of almost the same magnitude. Between 100 K and 200 K, the opening of the parabola changes the sign. Also at 100 K additional features appear in the curve, that are similar to what is found in fig. 4.21

in conductivity $\Delta\rho_{xx,ip}$ for the AMR and $\Delta\rho_{xx,oop}$ have been calculated. $\Delta\rho_{xx,ip}$ decreases linearly from $0.065 \mu\Omega \cdot \text{cm}$ at 3 K to $0.055 \mu\Omega \cdot \text{cm}$ at 290 K. Contrary, $\Delta\rho_{xx,oop}$ increases strongly from $0.045 \mu\Omega \cdot \text{cm}$ at 3 K to $0.064 \mu\Omega \cdot \text{cm}$ at 200 K, where it remains constant. This opposite sign in the temperature dependence leads to a crossing point at roughly 100 K, where the AMR becomes smaller than the AIMR. The behaviour of the AIMR is unexpected and not in accordance to the results of Kobs [26]. So far the reason for this behaviour is not known. Clearly the two opposing temperature dependencies of the AMR and AIMR are the key to understand the unexpected behaviour in the longitudinal sweeps. The longitudinal geometry can be understood as the superposition of the θ_R - and the ϕ_R -rotation. For a first approximation the relation $\text{Rot}_\gamma \approx \Delta R_{xx,\theta\phi} = R_{xx,\theta} - R_{xx,\phi}$ is assumed. At 3 K the AMR dominates, hence the sweep exhibits a parabolic behaviour. At 200 K and 290 K the AIMR dominates. For this reason the parabolic behaviour has the opposite sign. At 100 K both AMR and AIMR are roughly the same. In this case the parabolic behaviour of both rotational measurements, this means the first order, cancel one another. Only the second and third order remain, resulting in the non-parabolic behaviour seen in fig. 4.21. To further investigate this point,

4 Magnetisation behaviour of ultrathin magnetic films

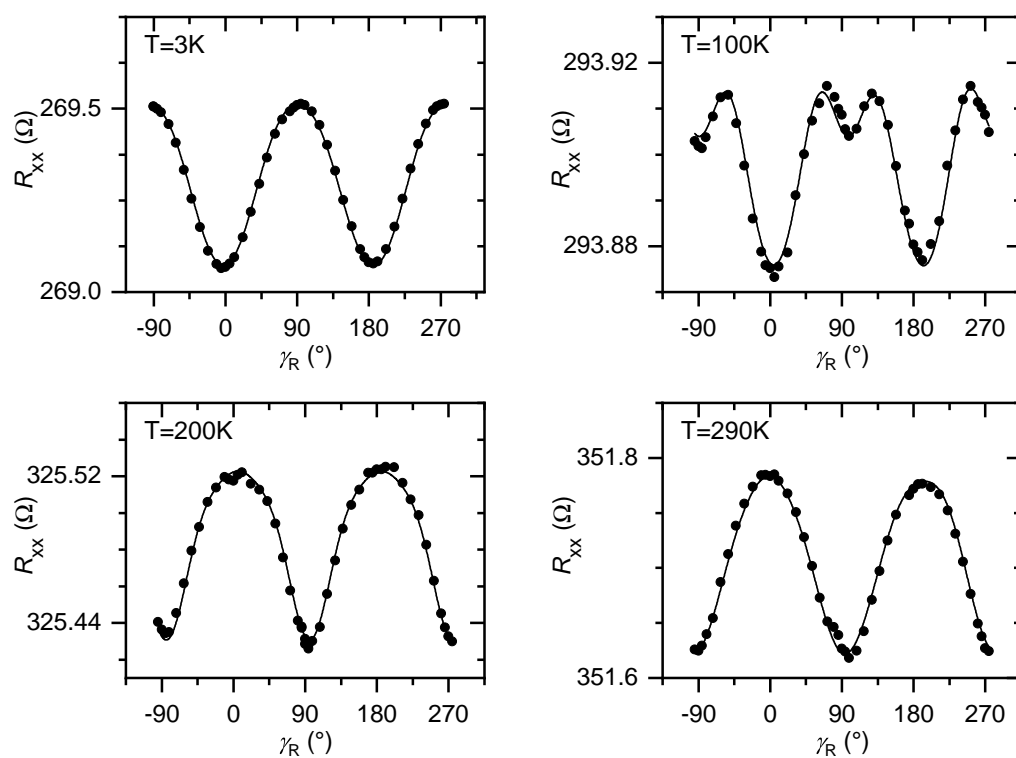


Figure 4.25: Rotational measurements with a magnetic field of 6T applied out of the plane (oop) of the film at different temperatures. Contrary to fig. 4.23 the γ angle is varied.

4.2 Magneto-transport measurements

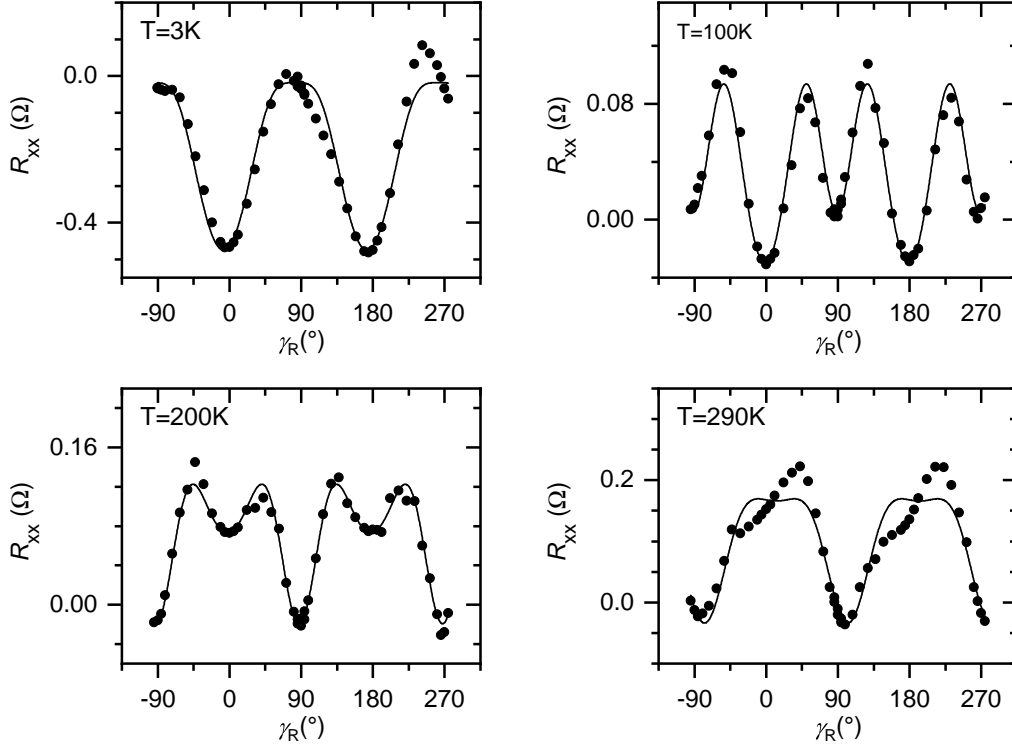


Figure 4.26: Subtraction of the two measurements from fig. 4.23. Counterintuitively the subtraction is not identically to the rotational measurements in dependence of the γ -angle shown in fig. 4.25.

the actual γ_R -rotation R_{xx,γ_R} has been measured and compared to $\Delta R_{xx,\theta\phi}$, which are shown in fig. 4.25 and 4.26. The rotational measurements show the behaviour found in the longitudinal sweeps in fig. 4.21. At 3 K there is a parabola with a positive sign. At 100 K the magnitude of the effect is reduced drastically and higher orders are observable. At 200 K a parabolic behaviour emerges again, but with a much smaller magnitude and a negative sign. The $\Delta R_{xx,\theta\phi_R}$ show a comparable behaviour, though it is not exactly the same. The higher orders at 100 K are a lot more pronounced than in the actual measurement. Also at 200 K higher orders appear that are not present in R_{xx,γ_R} . In conclusion the γ -rotation can not be exactly determined from the θ_R - and the ϕ_R -rotation.

Finally, fig. 4.27 shows the first, second and third order for both out of plane rotations. On the left hand side are the results for the θ_R -rotation. The first order is always positive and roughly double in size as the second order, which has a negative sign. The third order is very close to zero. No temperature dependence

4 Magnetisation behaviour of ultrathin magnetic films

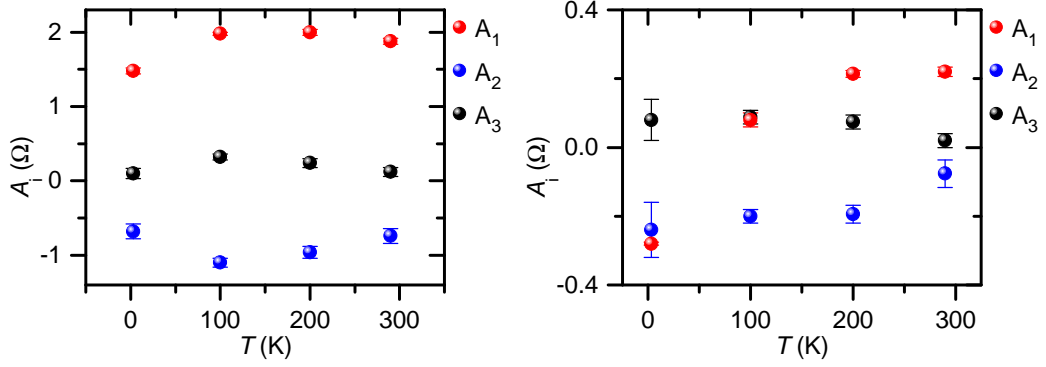


Figure 4.27: First, second and third orders of the fits to θ_R and γ_R rotational measurements shown in fig. 4.23 and 4.25. For the θ_R rotation on the left hand side, A_1 , A_2 and A_3 remain almost constant and $A_1 > A_2$. On the right hand side, the orders of the γ_R -rotation are shown. At 100 K A_1 is almost zero and $A_2 > A_1$, explaining the additional features found before. A_1 disappears because the AMR and AIMR are of the same magnitude at 100 K, since the effects have an opposing sign.

can be concluded. On the right hand side, the first, second and third order of the γ_R -rotation are presented. Contrary to before, the first and second order are of the same magnitude. Additionally, the first order changes drastically with temperature. At 3 K the sign is negative. At 100 K the sign changes to positive, but the magnitude of the first order is decreased resulting in a value that is smaller than the second order. At 200 K and above the magnitude of the first order increases again and is of the same size as the second order. This behaviour is the result of the different temperature dependencies of the AMR and the AIMR, since the γ_R -rotation is some kind of superposition of AMR and AIMR.

Comparing the change of $\Delta\rho_{xx,oop}$ and K_{eff} , it is obvious that both quantities behave similar. Both quantities increase with rising temperature. The change of the electronic properties might be an indicator for a change of the spin-orbit coupling, which is linked to the volume anisotropy.

5 Investigation of single magnetic nanostructures

So far magnetic films have been investigated. In this chapter the investigation of magnetic nanostructures are presented. In this thesis three different nanostructures have been investigated, that are shown in fig. 5.1. The diameter of the nanodots ranges from 16 nm to 45 nm. For every nanodot we assume the model of coherent rotation, which is backed up by theoretical considerations.

Sample overview

The measurement technique is based on the anomalous Hall effect, which connects the Hall voltage directly to the magnetisation and is explained in sec. 3.2. Three samples will be discussed in this thesis. Sample (a) has been used to investigate the temperature dependent magnetisation behaviour. Temperature dependent measurements of the switching field and frequency are performed. Furthermore the magnetic moment and the magnetic anisotropy are determined. Sample (b) has been used to perform three dimensional measurements of the switching field. Sample (c) consists of a particularly small nanodot and pushes the measurement principle to its limits. Since the measurement technique allows to measure in a broad temperature range, the samples can be investigated in the blocked as well as in the superparamagnetic regime. Depending on the regime, different measurement methods are used, that are discussed in the following. In the blocked regime magnetic field sweeps are applied, leading to hysteresis measurements. In the superparamagnetic regime the spontaneous magnetisation reversal is determined by probing the Hall voltage over time. And also in the blocked regime, so called destabilisation measurements are performed where spontaneous magnetisation reversal is induced by manipulating the energy barrier.

5 Investigation of single magnetic nanostructures

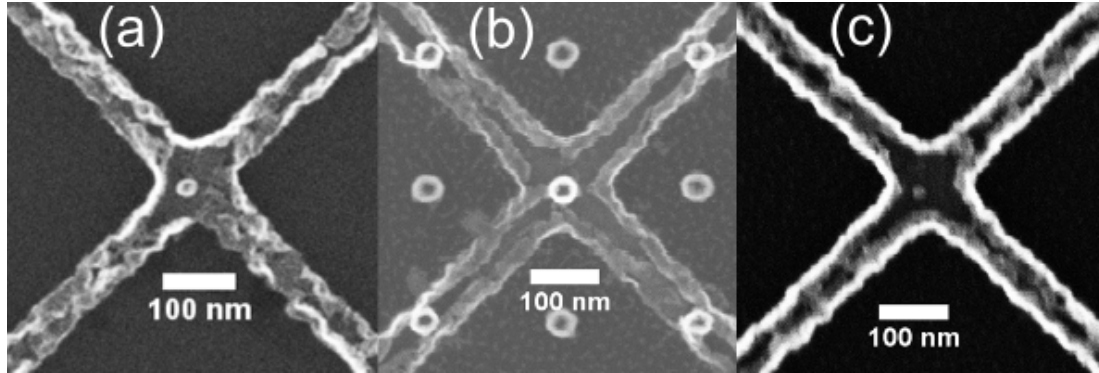


Figure 5.1: Overview of the samples, that are investigated in this thesis. Sample a) ($d = 32$ nm and $t_{Co} = 0.7$ nm) will be discussed in sec. 5.2 and was used to investigate the temperature dependent magnetisation behaviour. Temperature dependent measurements of the switching field and frequency are performed. Furthermore the magnetic moment and the magnetic anisotropy are determined.

Sample b) ($d = 45$ nm and $t_{Co} = 1$ nm) is discussed in sec. 5.1.1. The three dimensional switching surface is measured for this sample. Strong deviations to the Stoner-Wohlfarth model are found. A model is shown to explain the behaviour.

Sample c) ($d = 16$ nm and $t_{Co} = 0.7$ nm) is shown in sec. 5.1.3. The nanodot is comparably small and shows the limit of the measurement technique.

Hysteresis measurements

Below the blocking temperature, in the blocked regime, magnetic field sweeps are made. If the field is strong enough the magnetisation will align itself to the field. When sweeping the field between a high positive and negative field strength, typical hysteresis loops can be measured. From these hysteresis measurements switching fields H_{Sw} can be determined. The angle ϕ between the field and the film normal can be varied. This makes it possible to determine the angular dependence of the switching field, which is discussed in chapter 5.1.1. A typical hysteresis curve is shown in fig. 5.2 and the measurement geometry is explained. The angle β is the angle between the x-axis and the projection of the magnetic field in the xy-plane. β can be varied to determine the three dimensional switching behaviour. If not stated otherwise $\beta = 0^\circ$.

Random telegraph noise measurement

Above the blocking temperature the nanodot will be superparamagnetic. The thermal energy $k_B T$ is high enough to induce spontaneous magnetisation reversal

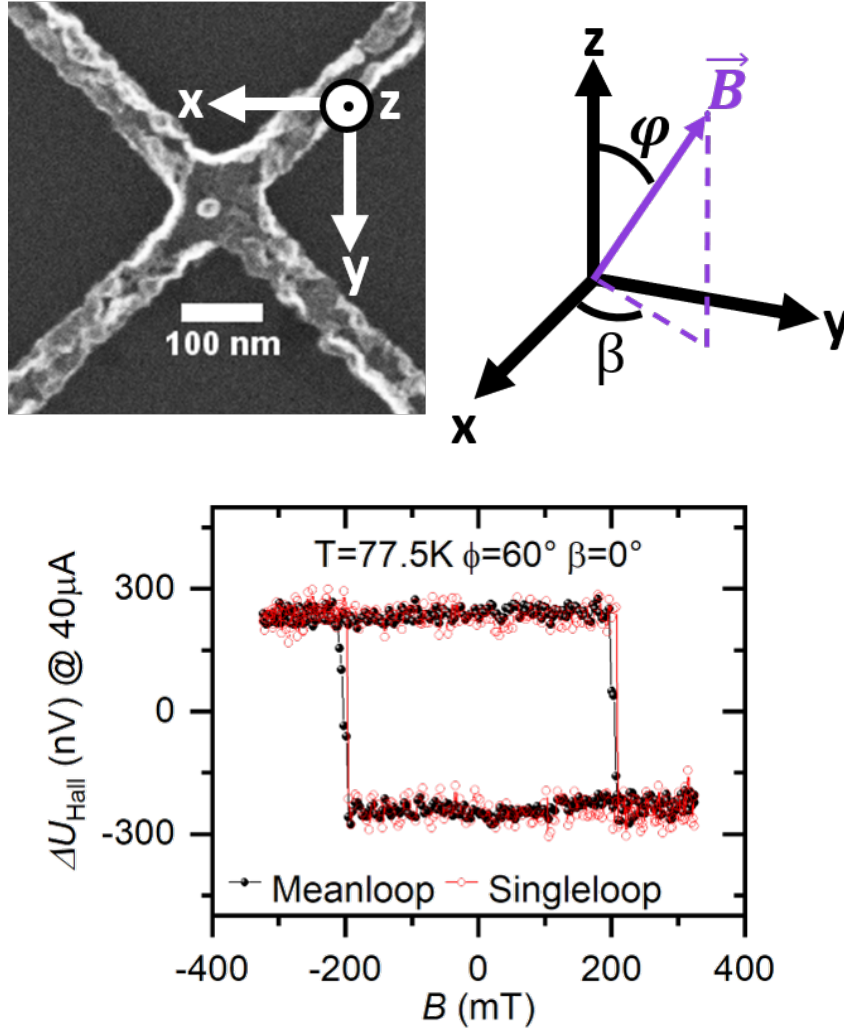


Figure 5.2: The figure shows a hysteresis loop of sample a). The measurement has been performed at $T = 77.5 \text{ K}$ with an applied current of $40 \mu\text{A}$. The red dots show one individual measurement, called single loop. The black curve shows a mean loop, that is averaged over ten individual measurement. This is done to reduce the noise. To perform a magnetic field sweep a field B needs to be applied. The direction of B is defined by the two angles ϕ and β , that can be seen in the coordinate system. To measure the angular dependence of the switching field, the angle ϕ is varied, while β is constant. If not stated otherwise, $\beta = 0^\circ$. The jump in the hysteresis curve defines the switching field $\mu_0 H_{\text{Sw}}$.

5 Investigation of single magnetic nanostructures

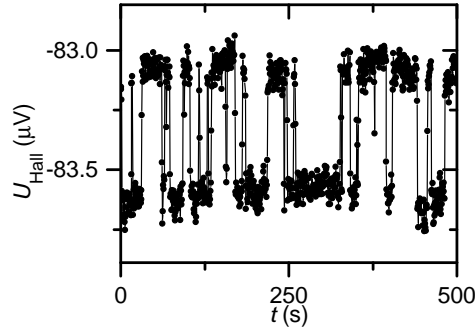


Figure 5.3: The figure shows the measurement of the random telegraph noise of sample a). The Hall voltage is simply measured over a time interval. The signal jumps between two plateaus, that are the two states of magnetisation. From the measurement the average switching time can be determined.

between the two possible states of magnetisation. Since the Hall voltage is dependent on the state of magnetisation, two plateaus can be observed in the measurement signal, that correspond to one of the two states. This kind of measurement is called random telegraph noise measurement (RTM) and is made by measuring the Hall voltage over a time interval. The average time that it takes to switch between the two states of magnetisation is called average switching time τ . The inverse of the switching time is called the switching frequency $f = 1/\tau$. Usually τ will be used in this thesis, though f might appear occasionally, when referring to other papers. The superparamagnetic behaviour is described by the Néel-Arrhenius law:

$$\tau = \tau_0 \exp\left(\frac{KV}{k_B T}\right) \quad (5.1)$$

τ_0 is the pre-exponential factor of the Néel-Arrhenius law. It is the inverse of the often used attempt frequency $f_0 = 1/\tau_0$.

Overview of single nanostructures in literature

Magnetic nanostructures have been investigated by multiple researchers over the years, using many different measuring techniques. Most often ensemble measurements are performed, which is often done by magnetic force microscopy (MFM) [128–140]. Krause et al. [141–143] uses spin-polarised STM to probe single Fe/W(110) nanoislands. Wernsdorfer [144] used micro-squids to investigate single magnetic nanostructures. Wernsdorfer et al. performed a multitude of

measurements [145–166] from switching times measurements to the measurements of three dimensional switching surface, which will be later discussed. Compared to Hall magnetometry, the technique is limited in temperature and the strength of the magnetic field, because the squid needs to be superconducting. On the positive side, due to a higher sensitivity smaller particles have been investigated for example 3 nm Co cluster.

An alternative to micro-squids is Hall magnetometry. This can be either based on the normal Hall effect [167–176] or like in this thesis the anomalous Hall effect. The AHE is not limited in the temperature range or the magnetic field and has also been utilised by Kikuchi et al. [177–181], who was able to measure single structures down to 40 nm. The group has also performed ensemble measurements of dots with a diameter of 10 nm [182]. In this thesis a single nanodots as small as 16 nm has been measured.

5 Investigation of single magnetic nanostructures

5.1 Magnetisation behaviour of single magnetic nanostructures

5.1.1 Three dimensional switching curve

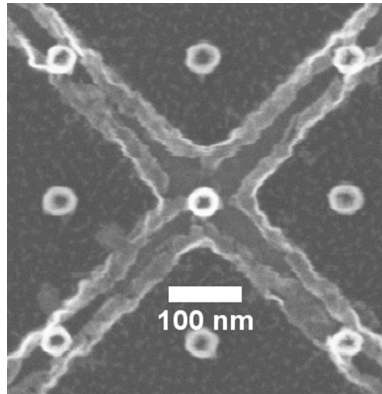


Figure 5.4: A SEM micrograph of a Hall bar with a nanodot in the crossing area of the leads. The nanodot ($d = 45$ nm and $t_{\text{Co}} = 1$ nm) is used to determine the three dimensional switching field surface. The motivation is to gain knowledge about the anisotropy potential of the nanodot.

This section deals with the angular dependence of the switching field in three dimensions. The three dimensional switching surface is investigated for the sample shown in fig. 5.4, which is a Pt/Co/Pt nanodot with a diameter of 45 nm and a Co thickness of 1 nm. The underlying idea behind the measurement was to determine the energy potential from the switching behaviour. The measurements were done in a cryostat containing a three dimensional vector magnet, that allowed to apply magnetic fields in all spatial angles. The switching fields are determined as a function of two angles called ϕ and β . The two angles are defined in fig. 5.4. The switching field has been measured in dependence of ϕ at fixed angles β , ranging between $\beta = 0^\circ$ and $\beta = 180^\circ$ in steps of $\Delta\beta = 22.5^\circ$. The angular dependence of the switching field in respect to the angle ϕ for different angles β are shown in fig. 5.5. The curves differ quite a lot, but some overall similarities can be seen in all measurements. There is always a maximum in the hard axis of magnetisation at roughly $\phi = 90^\circ$ (respectively $\phi = -90^\circ$). The exact position of the hard axis seems to change by a few degree for the different curves. Another peak arises close to $\phi = 0^\circ$, which can be understood as the easy axis of magnetisation.

5.1 Magnetisation behaviour of single magnetic nanostructures

The strength of the peak in the hard axis of magnetisation varies drastically for different β , while the one at the easy axis of magnetisation remains unchanged. For $\beta = 0^\circ, 22.5^\circ$ and 157.5° the switching field in the easy axis is higher than in the hard axis, while at $\beta = 90^\circ, 67.5^\circ$ and 112.5° it is the opposite. Compared to the Stoner-Wohlfarth model (see fig. 2.2), the switching field in the easy axis is squeezed at those angles. Also, the peak in direction of the easy axis is broader than in the model. Between the peaks are two local minima at roughly $\phi = 45^\circ$ and $\phi = -45^\circ$. Interestingly the curve is not axial symmetric in all cases. For $\beta = 90^\circ$ the magnitude of the two minima differs strongly. For a better visualisation, the three dimensional switching surface will be determined and compared to the Stoner-Wohlfarth model. The three dimensional switching surface of the Stoner-Wohlfarth (see fig. 2.3) is axis symmetric with a circular hard axis plane. The switching surface has a distinct easy axis point. The switching field in hard and easy axis are of identical magnitude and the connecting lines between the hard axis and the easy axis are axial symmetric. It is clear from fig. 5.5, that the measured data set will look different. The experimental switching field surface can be determined from the measurements by using spherical coordinates:

$$\begin{pmatrix} B_x \\ B_y \\ B_z \end{pmatrix} = \begin{pmatrix} B_{Sw} \cdot \sin(\phi) \sin(\beta) \\ B_{Sw} \cdot \sin(\phi) \cos(\beta) \\ B_{Sw} \cdot \cos(\phi) \end{pmatrix} \quad (5.2)$$

The result can be seen in fig. 5.6. Comparing this to the Stoner-Wohlfarth switching surface, several distinctions are seen in the experimental data. Most of all, the symmetry is broken and the switching surface cannot be created by rotating a two dimensional switching field astroid. The hard axis plane of the surface is not circular but ellipsoidal (see fig. 5.6 top view). The switching field of the easy axis is squeezed compared to the long axis of the ellipse and the easy axis peak is broader. The connecting lines between hard and easy axis are not axis symmetric. Furthermore, the switching field surface is tilted with respect to the laboratory reference of frame. Obviously, the question arises how the assumption of a uniaxial anisotropy is still justified considering the aforementioned results. Kronmüller [183] as well as Chang and Fredkin [184] looked at the influence of the second order of the anisotropy on the switching field astroid. While the second order can explain the squeezing of the switching field in the easy axis,

5 Investigation of single magnetic nanostructures

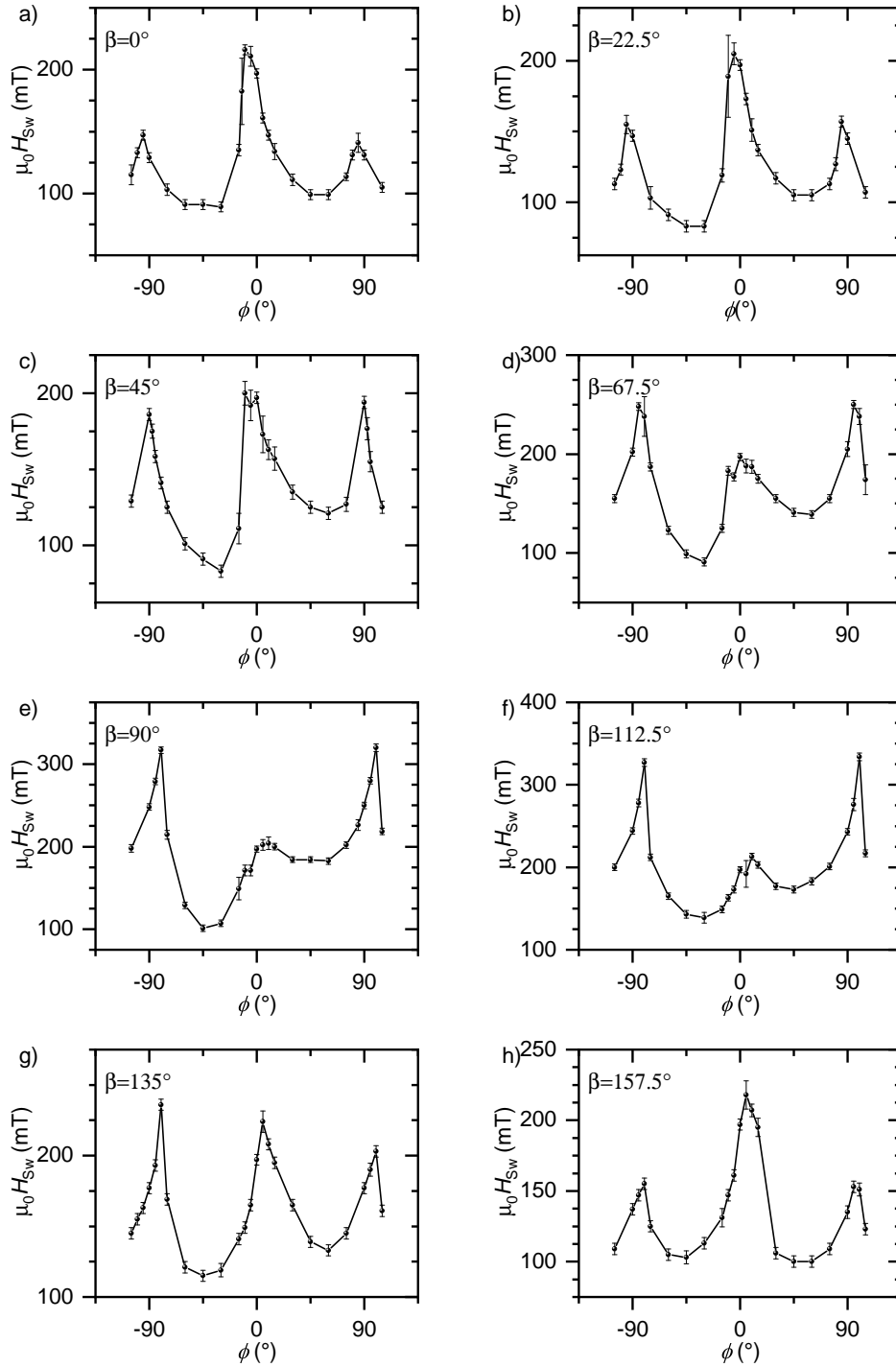


Figure 5.5: The figure shows all measured angular dependences of the switching field. The curves are distinguished by the spatial angle β , which has been varied. The peak at the hard axis of magnetisation ($\approx \pm 90^\circ$), differs strongly in strength and changes the position by a few degree. The peak at the easy axis of magnetisation ($\approx 0^\circ$) remains of the same magnitude. Overall, the found curves show a strong deviation from the Stoner-Wohlfarth model (see fig. 2.2).

5.1 Magnetisation behaviour of single magnetic nanostructures

all other features are missing. Fulmek and Hauser [185] calculated the angular dependence of the switching field for $\gamma\text{Fe}_2\text{O}_3$ particles under the consideration of the demagnetisation field and compared their results to the unaltered Stoner-Wohlfarth model. They found a reduction of the coercive field, but not the kind of deviation that can be seen in fig. 5.1.1. Due to this, in the next part a method developed by A. Thiaville [186, 187] is presented, that enables the opportunity to calculate the switching field surface for any given energy potential. Afterwards simulations that were made by Staeck in his PhD thesis [1] are shown. He modified the uniaxial energy potential based on the knowledge of the structural properties of the initial Co/Pt film system.

5 Investigation of single magnetic nanostructures

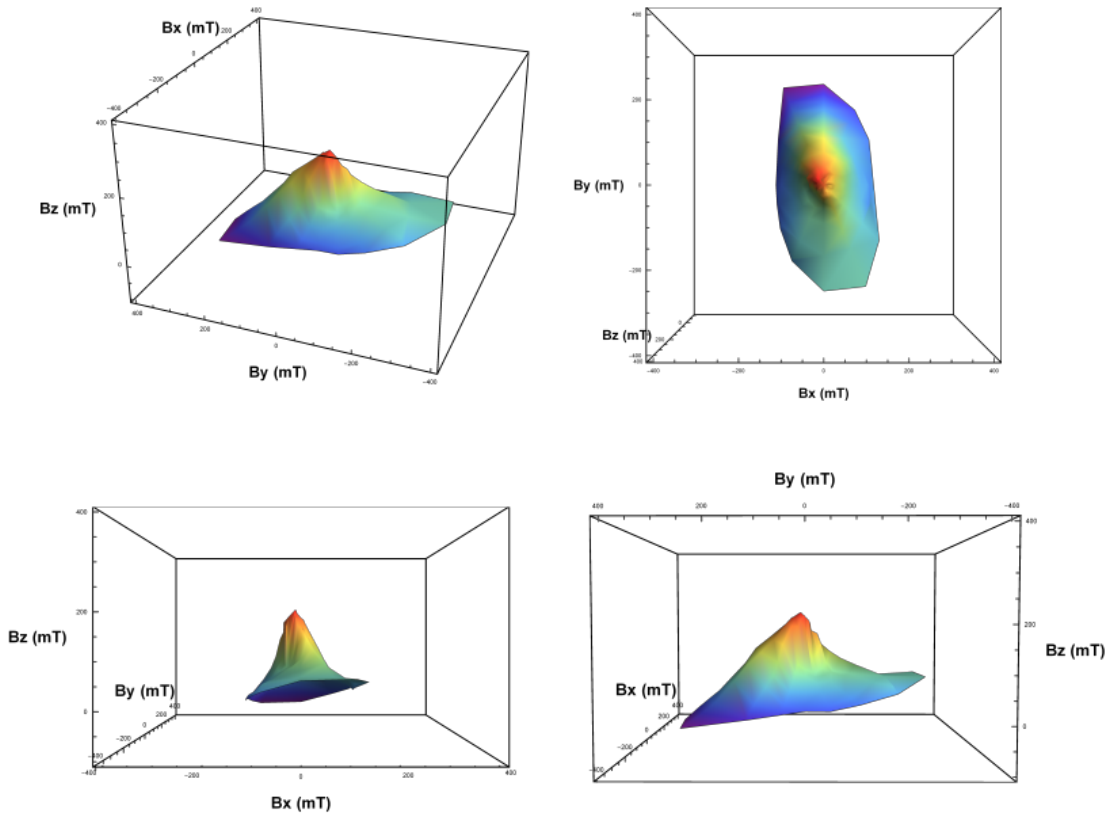


Figure 5.6: The three dimensional switching surface of a Co/Pt nanodot ($d = 45$ nm and $t_{Co} = 1$ nm). Only the upper half of the surface has been measured. For a better visualisation, four different view points are shown. The experimental data deviate strongly from the Stoner-Wohlfarth model. The hard axis plane is ellipsoidal in shape. The easy axis point is replaced by a cusp. The switching field is squeezed in the direction of the easy axis and the connecting lines running from the hard axis to the easy axis are not axis symmetric. The whole surface is tilted with respect to the laboratory reference of frame.

5.1 Magnetisation behaviour of single magnetic nanostructures

5.1.2 Thiaville method to determine three dimensional switching curves

A. Thiaville derived a method to determine the three-dimensional switching field astroid for an arbitrary energy potential E_{Ani} [186, 187]. The switching field is given by:

$$\mu_0 \vec{H}_{\text{Sw}} = \frac{2}{M_S V} \left(\frac{1}{2} \frac{\partial E_{\text{Ani}}}{\partial \theta} \cdot \vec{e}_\theta + \frac{1}{2 \sin(\theta)} \frac{\partial E_{\text{Ani}}}{\partial \phi} \cdot \vec{e}_\phi + \lambda \vec{m} \right) \quad (5.3)$$

λ is given by:

$$\lambda = \frac{1}{4V} \left(- \left(\frac{1}{\sin^2(\theta)} \frac{\partial^2 E_{\text{Ani}}}{\partial \phi^2} + \frac{\cos(\theta)}{\sin(\theta)} \frac{\partial E_{\text{Ani}}}{\partial \theta} + \frac{\partial^2 E_{\text{Ani}}}{\partial \theta^2} \right) + \sqrt{\left(\frac{1}{\sin^2(\theta)} \frac{\partial^2 E_{\text{Ani}}}{\partial \phi^2} + \frac{\cos(\theta)}{\sin(\theta)} \frac{\partial E_{\text{Ani}}}{\partial \theta} - \frac{\partial^2 E_{\text{Ani}}}{\partial \theta^2} \right)^2 + 4 \left[\frac{\partial}{\partial \theta} \left(\frac{1}{\sin(\theta)} \frac{\partial E_{\text{Ani}}}{\partial \phi} \right) \right]^2} \right) \quad (5.4)$$

This method was used by P. Staeck in his PhD thesis [1] to simulate switching field surfaces based on modified anisotropy potentials. His work will be shortly summarised. The idea was based on the poly-crystalline nature of the initial magnetic films. The film consists of grains, that have a diameter of 16 nm and may be tilted in respect to the film plane by a maximum angle of 23° . The tilting of the grains can be described by a Gaussian distribution, that has a peak in direction of the film normal and is isotrop in all spatial angles. Therefore, in a film the tilting disappears on average and all effects that arise from such tilted grains can be neglected. The investigated nanodot has a diameter of 45nm, meaning it consists only of a few grains and the tilting of the grains is not negligible. The underlying idea is, that the tilting of the grains results in a tilted volume and interface anisotropy. However, the shape anisotropy, which is determined by the shape of the nanodot, is not tilted. The uniaxial energy potential $E/V = \left(K_{1,V} + \frac{2K_S}{t} - K_{\text{shape}} \right) \sin^2(\theta)$ can then be modified to:

$$E/V = \left(K_{1,V} + \frac{2K_S}{t} \right) \cdot \sin^2(\theta - \theta_0) - K_{\text{shape}} \cdot \Delta N \cdot \sin^2(\theta) \quad (5.5)$$

ΔN describes the modification of the shape anisotropy for a cylindrical shaped nanostructure given by Millev et al. [37]. θ_0 is the tilting of the volume and

5 Investigation of single magnetic nanostructures

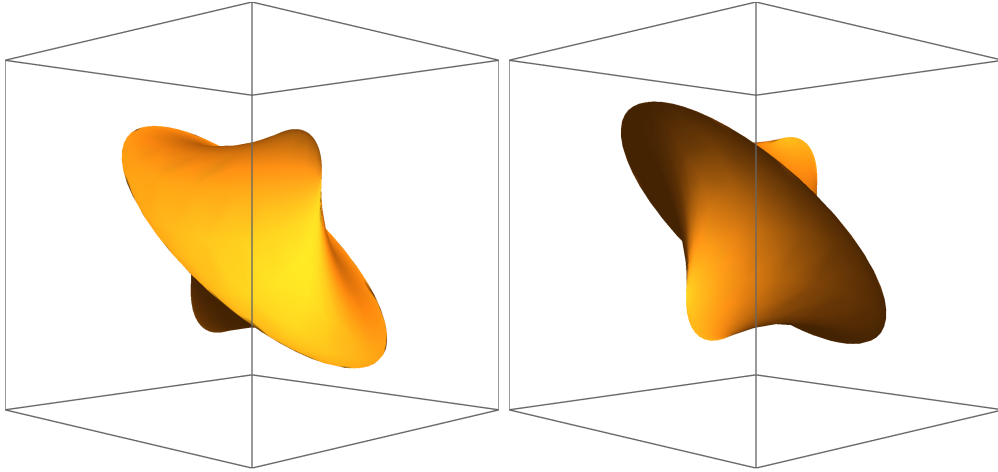


Figure 5.7: The figure shows a simulation made by Staeck (taken from [1]) by using the method of Thiaville [187]. Staeck used a modified energy potential $E/V = \left(K_{1,v} + \frac{2K_s}{t}\right) \cdot \sin^2(\theta - \theta_0) - K_{\text{shape}} \cdot \Delta N \cdot \sin^2(\theta)$, that is based on the structural properties of the initial, polycrystalline Co/Pt film system. The individual grains may be tilted in respect to the film normal. This may result in a tilting of the volume and interface anisotropy. The shape anisotropy is not tilted. The found switching field surface fits well to the experimental data. As in the measurement, the hard plane axis is ellipsoidal and the easy axis point is replaced by a cusp. The switching field in the easy axis is squeezed. Furthermore, the surface is tilted in respect to the reference of frame.

interface anisotropy in respect to the shape anisotropy. Using the aforementioned method of Thiaville, Staeck was able to model the three dimensional switching surface for this energy potential. The results are shown in fig. 5.7 and are taken from [1]. The model shows a good agreement to the experimentally found switching field surface seen in fig. 5.6. Especially the ellipsoid form of the hard axis plane and the tilting of the three dimensional astroid are reproduced well. The easy axis point is replaced by broad peak and the switching field in the easy axis is squeezed. Staeck also made two dimensional cut outs of the surface. These cut outs compare well to the two dimensional curves seen in fig. 5.5, that show the angular dependence of the switching field for different spatial angles. There is one feature that can be seen in the experimental data, but is missing in the simulation. The connecting lines between the hard axis to the easy axis are not symmetric. The experimental switching surface looks kind of buckled. Even more complex anisotropy terms, would be necessary for a complete description of the nanodot. Nevertheless, the model, that is based on the structural properties of the Co/Pt film, describes the experimental data well.

5.1 Magnetisation behaviour of single magnetic nanostructures

In literature similar investigations have been done by the group of Wernsdorfer, whose measurement technique is based on micro-squids [146, 166]. Wernsdorfer et al. [152] measured the switching field astroid of BaFeCoTiO nanoparticles. At a first look, a good agreement to the Stoner-Wohlfarth astroid is found. In detail it can be seen, that the easy axis is tilted by about 20° . Furthermore, the peak is round unlike the Stoner-Wohlfarth astroid, which has a sharp peak. Like in this thesis, their first explanatory ansatz is based on the work of Fulmek et al. [185] and Chang [54]. Fulmek et al. regarded the influence of the second order of the anisotropy, which leads to a quartic anisotropy $K_{\text{Uni}} = K_1 \sin^2(\theta) + K_2 \sin^4(\theta)$. Depending on the ratio of K_1/K_2 different shapes of the switching field astroid appear. The second order can explain a reduction of the switching field in the easy axis, but does not result in a tilt of the easy axis. The same conclusion can be drawn from Chang, who took the demagnetisation field under consideration. Similar deviations from the Stoner-Wohlfarth model are found in a Ni wire [149] and in a FeSi wire [154].

In a collaboration with Thiaville [187], they started to modify the anisotropy potential in order to reproduce their experimental switching field astroids. As an example they used Co particles, that were measured by Wernsdorfer [153]. Thiaville proposes a biaxial anisotropy constant in combination with higher order anisotropy terms of fcc origin. He finds a good agreement, to the data.

Bonet et al. [157] were the first to measure a three dimensional switching surface of a BaFeO nanoparticle. Similar to the findings in this thesis, their curve can not be created by rotating a two dimensional switching field astroid. They explain this deviation by adding the shape anisotropy and hexagonal anisotropy terms to the anisotropy potential.

A very similar result to the Co/Pt nanodots, has been published by Jamet et al. [161, 164], who measured 3 nm Co clusters. The switching field surface has the same ellipsoidal shape in the hard plane as the Co/Pt dots. Jamet et al. explain this by adding a fourth order anisotropy term to the anisotropy potential, which has a different coordinate system than the first and second order. The fourth order is tilted by 45° in respect to the z -axis of the first and second order coordinate system. They performed high resolution TEM of their cluster, gaining knowledge about the structural properties. Despite the different anisotropy potential, their model reproduces similar features, than the simulation shown in fig. 5.7.

5 Investigation of single magnetic nanostructures

In conclusion, the determination of the anisotropy potential from the switching field astroid can not be deemed unambiguous without knowledge of the structural properties of the film. Additional anisotropy terms can reproduce the experimental features, but the validity of the model might be questionable. In our case, the used model is backed by the knowledge of the structural properties of the initial thin film. Tilted grains result in an angle between K_{shape} and $K_V + \frac{2K_S}{t}$, which leads to an modified anisotropy potential. In consequence, the three dimensional switching surface can not be created by rotating a two dimensional astroid. Features like a ellipsoidal shape of the hard axis plane, a squeezing of the switching field in the easy axis as well as a replacement of the easy axis point by a broad peak can be modelled. More complicated anisotropy models might of course lead to even better agreement of model and measurement.

5.1.3 Limits of the measurement technique

This chapter shows the limits of the measurement technique and displays the smallest nanodot, that could be created by the setup used in this thesis. The dot is shown in fig. 5.8 and has a diameter of just 16 nm. The leads of the Hall bar are 80 nm wide. A relatively high current of $70 \mu\text{A}$ had to be applied to the sample to measure a signal (usually $20 - 40 \mu\text{A}$ are applied). A high current results in higher Joule heating, that might lead to changes in the crystal structure. This might alter the properties of the nanodot. In fig. 5.9 on the left hand side a hysteresis curve is shown. This is a mean loop that was averaged over seven single loops. The signal difference between the two plateaus is 100 nV, which is comparably small and results in a bad signal to noise ratio of 2. The signal to noise ratio could be improved, by decreasing the width of the Hall bar leads to 60 nm or 40 nm. A drawback could be a decrease in durability, as smaller leads might easier break due to small discharges. On the right hand side of fig. 5.9 temperature dependent measurements of the switching field have been performed. The blocking temperature of the nanodot lies approximately between 75 K and 85 K, which shrinks the possible temperature range for the investigations. Between 30 K and 60 K the switching field decreases almost linearly, witch is in accordance to the theories of temperature dependent switching fields that are given by Sharrock [188, 189], Chantrell [190, 191], El-Hilo [192] and Garg [60]. Between 2.5 K and 30 K the slope of the decrease is smaller. This behaviour deviates from

5.1 Magnetisation behaviour of single magnetic nanostructures

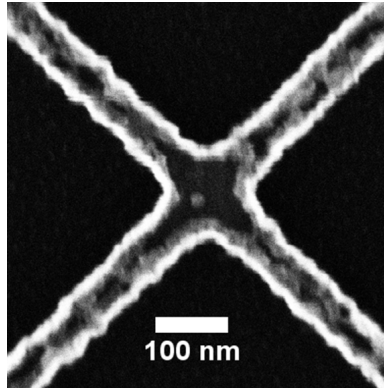


Figure 5.8: A SEM micrograph of a Hall bar containing a nanodot with a diameter of $d = 16$ nm. The leads of the cross have a width of 80 nm. The initial magnetic film was composed of a 7 nm Pt seed layer, a 0.7 nm Co layer and a 5 nm Pt cap layer. This results in magnetic volume of $V = 141$ nm³. This nanodot displays the smallest sample that was created by means of electron beam lithography.

the mentioned theories and was also found by A. Neumann [29] and Wilhelm [31] and is so far unexplained. Possible explanations are magnetic quantum tunnelling and Bose-Einstein condensation of magnons. In magnetic quantum tunnelling the magnetisation tunnels through the energy barrier instead of overcoming it due to thermal energy [193]. This has been measured by Wernsdorfer [152] in BaFeCoTiO nanoparticles containing $10^5 \mu_B$ at temperatures below 0.4 K. The high temperature used in the experiment ($T > 2.5$ K) makes it unlikely to be the reason for the decreasing switching field. Bose-Einstein condensation of magnons leads to a reduction of the saturation magnetisation below the condensation temperature [194–196], which could be a reason for the reduced switching field.

In fig. 5.10 the angular dependence of the switching field has been measured for 2.5 K, 45 K and 60 K. On the left hand side the switching field is plotted against the angle θ , hence the angle between the field and the easy axis of magnetisation, that is the film normal. The angular dependence deviates strongly from the expected behaviour of the Stoner-Wohlfarth model. These deviations are even stronger pronounced than seen in the previous chapter in fig. 5.5. First the maxima, that are attributed to the hard axis of magnetisation and lie at $\theta = 90^\circ$ and $\theta = -90^\circ$ in the Stoner-Wohlfarth model, are found at $\theta = -55^\circ$ and $\theta = 125^\circ$. The third maximum that is attributed to the easy axis of magnetisation lies at $\theta = -20^\circ$. This maximum is relatively weak and the position between the hard axis is not symmetric. On the right hand side in fig. 5.5 the data has

5 Investigation of single magnetic nanostructures

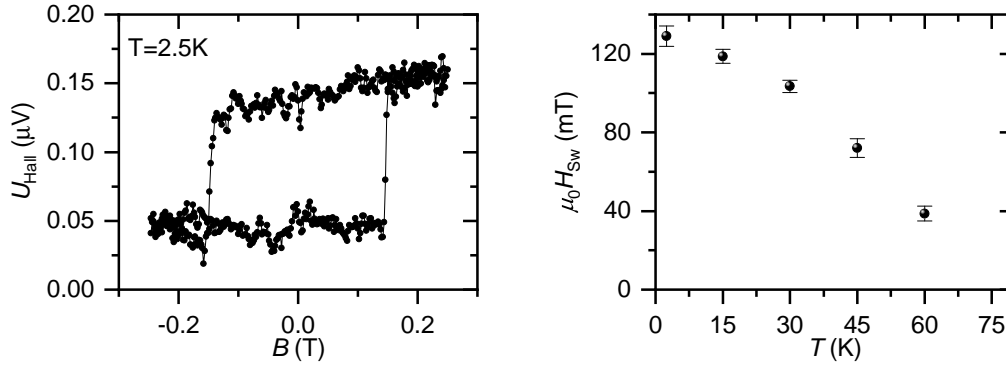


Figure 5.9: The left hand side shows a hysteresis loop of the Hall voltage at 2.5 K. The plot shows a mean loop that was averaged over seven single loops. This was necessary because of the bad signal to noise ratio. The noise of a single is 50 nV, while the signal difference between the plateaus of the hysteresis is about 100 nV. 70 μA has been applied to the Hall bar.

On the right hand side the temperature dependence of the switching field is plotted. The switching field was measured at an angle $\theta = 35^\circ$. The switching field decreases from 130 mT at 2.5 K to 40 mT at 60 K. The blocking temperatures lies approximately between 75 K and 85 K.

been plotted in astroid form. When comparing the different temperatures the decrease of the switching field appears to be uniform for most angles. This is in accordance to Jamet [161]. Like in fig. 5.6 and fig 5.7 a strong tilting can be seen. Compared to the previous measurement similar features are found albeit in a stronger manifestation. This can be understood by the fact, that the smaller nanodot contains fewer grains and the characteristics of the nanodot are dominated by possibly only one grain. When the crystal axis of this grain is strongly tilted, the effects described in the previous chapter found by Staeck [1] come into play. In a larger nanodot, that consists of more grains, the effect can be smaller. This stems from the fact, that the individual tilting angles of the different grains may cancel each other out in average to some extent. Also it must be mentioned that my colleague E.-S. Wilhelm [31] found similar results in larger nanodots.

Summarising, it is possible to create nanodots with a diameter as small as 16 nm. Due to reasons stemming from the measurement technique and the characteristics of the nanodot, drawbacks are found. A high current has to be applied leading to higher Joule heating. A bad signal to noise ratio of 2 is found. This could be improved by decreasing the diameter of the leads from 80 nm to 40 nm or 60 nm. This would lead to drawbacks in terms of durability of the Hall bar.

5.1 Magnetisation behaviour of single magnetic nanostructures

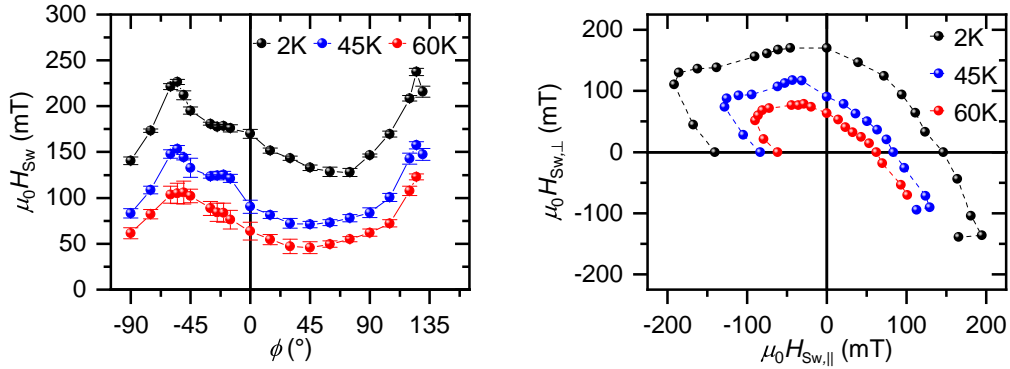


Figure 5.10: Both plots show the angular dependence of the switching field. On the left hand side the switching field is plotted against the angle between the magnetic field and the easy axis of magnetisation. Maxima are found at $\theta = -55^\circ$ and $\theta = 125^\circ$, which is a strong deviation from the Stoner-Wohlfarth model, that puts the maxima at $\theta = -90^\circ$ and $\theta = 90^\circ$. The maximum at $\theta = -20^\circ$ is relatively weak.

On the right hand side the x- and y- components of the switching field are plotted resulting in the astroid form. A strong tilting of the astroid can be seen, which is in accordance to the simulations performed by Staeck [1] that are shown in fig 5.7. The astroid shrinks uniformly with rising temperatures which is accordance to results found by [161].

The temperature range to perform investigations becomes much smaller, as the blocking temperature decreases because of the smaller magnetic volume. Finally, the nanodot might display a strong deviation from the Stoner-Wohlfarth model, which makes it difficult to model the measurement data. For this reasons, a larger nanodot was used in the following chapter, which continues the investigation of the temperature dependence of the anisotropy.

5.2 Temperature dependence of the anisotropy in single magnetic nanostructures

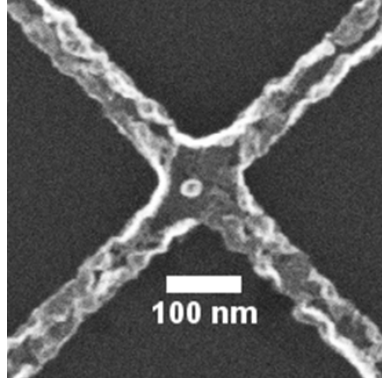


Figure 5.11: A hall bar containing a nanodot with a diameter of $d = 32$ nm. The leads of the cross have a width of 80 nm. The initial magnetic film was composed of a 7 nm Pt seed layer, a 0.7 nm Co layer and a 5 nm Pt cap layer. This gives a nominal magnetic volume of $V = 563$ nm³. The sample was used in the following investigation about the magnetic anisotropy.

In chap. 4.1 the temperature dependency of the anisotropy in thin magnetic films was investigated. The following chapter extends this investigation to magnetic nanostructures. Therefore a Hall bar containing a nanodot was prepared from a Pt/Co/Pt film (see ch. 3.3). The film was composed of a 7 nm Pt seed layer, a 0.7 nm Co layer and a 5 nm Pt cap layer. Fig. 5.11 shows a SEM image of the Hall bar geometry. The nanodot in the crossing area of the Hall bar has a diameter of 32 nm. Using the nominal Co thickness of 0.7 nm a magnetic volume of 563 nm³ arises. For a preliminary characterisation, the angular dependence of the switching field was determined at 77.5 K, which is shown in fig. 5.12. Though some of the characteristics found in ch. 5.1.1 can also be seen here, the angular dependence deviates significantly less from the Stoner-Wohlfarth model. The hard axis of magnetisation lies in the film plane, which is represented by the peak at $\pm 90^\circ$. The easy axis lies at 5° and two minima appear at 45° and -45° . The switching field in the hard axis is 300 mT and in the easy axis 250 mT. The peak in the easy axis is broadened. H_{sw} is 175 mT at 45° and 190 mT at -45° . The difference of 15 mT is much less than in other measurements (see again ch. 5.5). The right side of fig. 5.12 shows the switching field astroid. Overall, $H_{sw}(\phi)$ of the nanodot shows a much better agreement to the Stoner-

5.2 Temperature dependence of the anisotropy in single magnetic nanostructures

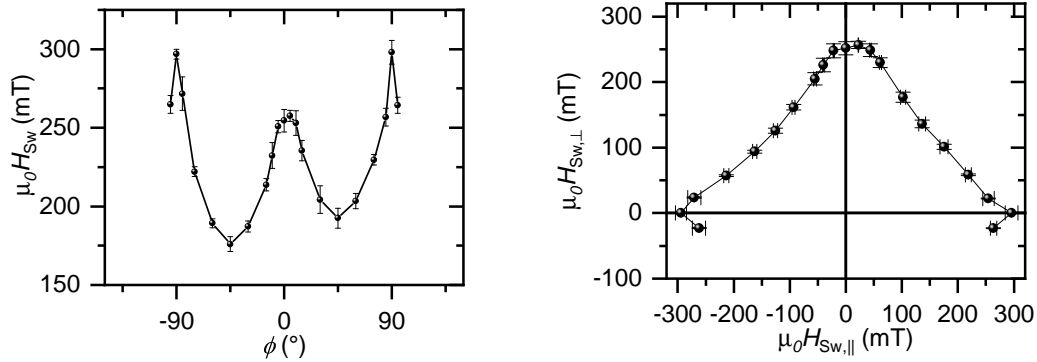


Figure 5.12: On the left hand side, the angular dependence of the switching field H_{Sw} measured at 77.5 K is shown. The hard axis of magnetisation lies at $\pm 90^\circ$ with a corresponding switching field of about 300 mT. The easy axis lies at 5° with $H_{\text{Sw}} = 250$ mT. At 45° and -45° two minima are located. At 45° the switching field lies at 175 mT and at -45° at 190 mT. Compared to the measurements in the previous chapter (see 5.1.1) the deviations from a perfect Stoner-Wohlfarth behaviour are relatively small, as the maximum in the easy axis of magnetisation is only tilted by a few degrees and only 50 mT smaller than in the hard axis. The minima at 45° and -45° only deviate by about 15 mT. The right hand side, shows the astroid representation.

Wohlfarth model than the previous samples. This makes the nanodot a good candidate for the investigation. Since there are only slight deviations from the Stoner-Wohlfarth model, it is assumed that the tilt between both the volume and interface anisotropy and the shape anisotropy is only small and the Stoner-Wohlfarth model is still suited to describe the nanodot.

5 Investigation of single magnetic nanostructures

5.2.1 Temperature dependence of switching field and superparamagnetic behaviour

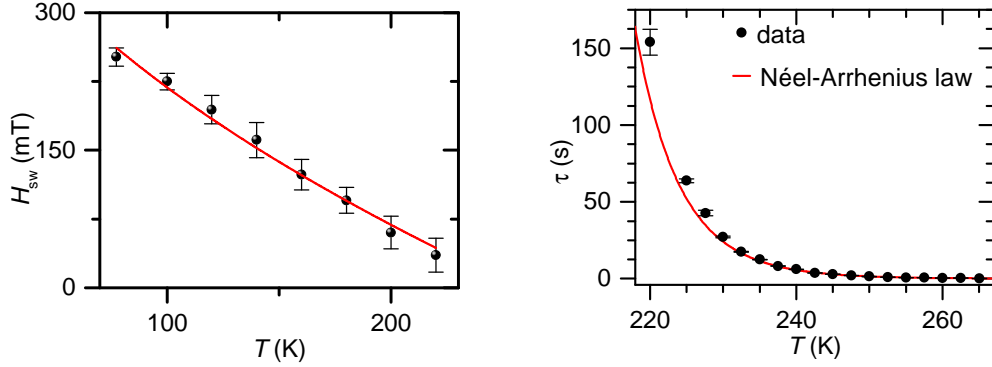


Figure 5.13: On the left, the switching fields of the blocked nanodot are shown with a fit of the Garg formula [60]. The switching field decreases with increasing temperature. The blocking temperature is around 220 K. On the right, switching times over temperature for the superparamagnetic nanodot. In red the Néel-Arrhenius law is fitted to the data. The pre-exponential factor τ_0 is determined as $2 \cdot 10^{-14}$ s, which is orders of magnitude lower than expected [7].

The experimental method allows for the investigation of a broad temperature range, meaning the nanostructures can be investigated in the blocked regime as well as in the superparamagnetic regime. Two kinds of measurements are performed: hysteresis loops in the blocked regime and switching frequencies in the superparamagnetic regime. The temperature dependence of the switching field and the switching times are plotted in fig. 5.13. The switching times can be well described by a Néel-Arrhenius law, as can be seen on the right hand side of fig. 5.13. The fit gives $KV = 1.1 \cdot 10^{-19}$ J. The pre-exponential factor τ_0 is determined as $2 \cdot 10^{-14}$ s, which is some orders of magnitude lower than expected from Brown's theory (10^{-9} s – 10^{-11} s) [7]. This is supported by temperature dependent measurements of the switching fields in the easy axis, that are determined from the hysteresis loops, which is plotted on the left hand side of fig. 5.13. The temperature dependent measurements yield a blocking temperature of $T_B = 220$ K. The formula of Garg (eq. 2.30) is fitted to the measurement data, resulting in a pre-exponential factor ($\approx 10^{-14}$ s) that is also well below the expected result. For KV the same value that was determined from the Néel-Arrhenius fit is used. Other works reported also high attempt frequencies in other systems [142, 197, 198].

5.2 Temperature dependence of the anisotropy in single magnetic nanostructures

Krause et al. reported about the switching behaviour of in-plane magnetised atomic-scale Fe/W(110) nanoislands, which were investigated with spin-polarised scanning tunneling microscopy [142]. Varying pre-exponential factors were found, ranging from 10^{-16} s up to 10^{-13} s. These factors strongly depend on the size and shape of the islands. The switching mechanism in the nanoislands is revealed to be domain wall nucleation and propagation. In [143] Krause et al. continue their investigation. Here, nanoislands are investigated in two different temperature regimes, that cannot be described by one single Néel-Arrhenius law, as the switching times in the higher temperature regime differ by orders of magnitude from the lower temperature regime. Using an analytical four-state hopping model, they explain this with a complex interplay between nucleation, annihilation and propagation. Rohart et al. [198] investigated two-dimensional Co nanodots on Au(111). Atomic scale simulations at finite temperatures (based on the Heisenberg Hamiltonian) found a deviation from the macrospin model, that can be explained by thermally excited spin-wave modes. The simulations show f_0 to depend on the number of atoms. Increasing the number of atoms from 1 to 1000 increases f_0 by one order of magnitude from 40 GHz to several hundred GHz. In [199] and [200] structural impacts were investigated, namely side wall damage in nanostructures due to the patterning process [199] and the influence of Pt capping on the magnetic properties of Co nanodots [200]. In both cases a strong influence on the anisotropy is found.

Beside these existing theories another approach is presented in this thesis, that might partially explain deviations of the pre-exponential factor (or attempt frequency) from Brown's theory. This approach (also discussed in [29] and [32]) is based on the temperature dependence of the anisotropy. This becomes evident when the Néel-Arrhenius law is rewritten to $\ln(\frac{\tau}{\tau_0}) \cdot k_B T = K V$. This form of presentation is shown in fig. 5.14. KV decreases with temperature, which can be roughly described by a linear fit. It is assumed that the volume remains constant over the small temperature range, implying a temperature dependent anisotropy, which was also found in thin magnetic films (see ch. 4.1). When a linear temperature dependence $K(T) = K_0 + \frac{dK}{dT} \cdot T$ is assumed, the Néel-Arrhenius law can be modified to $\tau = \tau_0 \exp\left(\frac{(K_0 + K_T T)V}{k_B T}\right)$, which is equivalent to:

$$\tau = \tau_0 \exp\left(\frac{K_T V}{k_B}\right) \exp\left(\frac{K_0 V}{k_B T}\right) \quad (5.6)$$

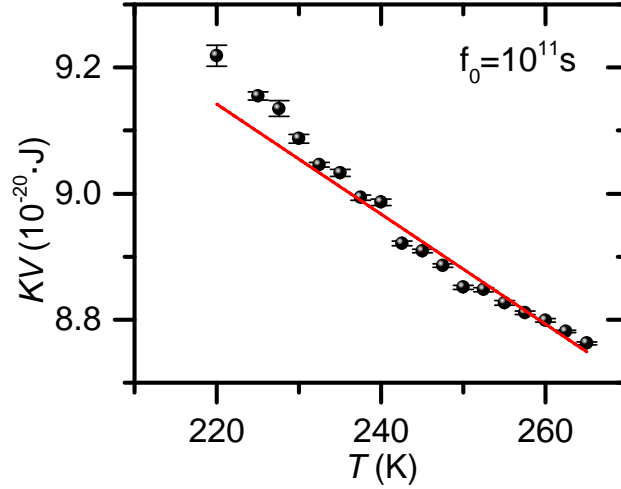


Figure 5.14: The energy barrier KV is calculated from the switching times by $KV = \ln\left(\frac{\tau}{\tau_0}\right) \cdot k_B T$. For the calculation a pre-exponential factor of $\tau_0 = 10^{-11}$ s is used. KV decreases and in red a linear fit is applied. Assuming that the volume remains constant over the temperature range, this indicates that the anisotropy decreases further motivating the idea that a temperature dependent anisotropy effects the pre-exponential factor of the Néel-Arrhenius law.

Compared to the classical Néel-Arrhenius law, an additional exponential term, $\exp\left(\frac{KV}{k_B T}\right)$, appears. When the Néel-Arrhenius law is fitted to measured switching times, the found pre-exponential factor τ'_0 will in fact be a product of τ_0 and the additional term: $\tau'_0 = \tau_0 \cdot \exp\left(\frac{KV}{k_B T}\right)$. As was already mentioned, a temperature dependent anisotropy can be observed in thin magnetic films (ch. 4.1), whereas small Co layer thickness ($t_{Co} = 2$ nm) shows a negative slope and large thickness ($t_{Co} > 5$ nm) a positive slope. Using the highest positive and negative slopes of the films found in sec. 4.1.5 an additional factor of 10^{-3} or 10^4 is possible, leading to an high uncertainty in the determination of τ_0 without exact knowledge of the anisotropy. Therefore, it will be investigated if the anisotropy of the film is passed on to the nanodot and if the temperature dependence of the anisotropy explains the pre-exponential factor. Stier et al. [201] published a general theoretical investigation about the impact of a temperature dependent anisotropy on the analysis of superparamagnetic behaviour, confirming the previously presented considerations. The publication emphasizes that the determined attempt frequencies need to be interpreted carefully, in particular when the investigated temperature interval is close to the Curie temperature. A fact that is especially important for the

5.2 Temperature dependence of the anisotropy in single magnetic nanostructures

investigation of nanoparticles, as alloying on the interfaces can drastically reduce the Curie temperature (see cha. 4.1).

This gave the motivation to experimentally investigate the temperature dependence of the anisotropy in nanodots as well. The biggest obstacle to determine the anisotropy is the missing knowledge of the saturation magnetisation M_S and the volume V of the nanodot. This problem is bypassed by determining the magnetic moment $m = M_S V$, which is explained in the next section.

5.2.2 Determination of the magnetic moment

The magnetic moment is a significant material property to understand the magnetic behaviour of a nanodot. It is also necessary to determine the magnetic anisotropy. The first approach would be to take the saturation magnetisation of Co from literature and measure the diameter of the nanodot by scanning electron microscopy to calculate the volume. The magnetic moment would then be given by $m = M_S V$. Unfortunately this magnetic moment yields unrealistic results, when used as a fit parameter for the measurements seen in sec. 5.2.1. Using a reverse approach and taking realistic values, leads to the finding, that the magnetic moment is significantly smaller by as much as a factor of 2.

The reduced magnetic moment might be the result of a reduced M_S , V or a combination of both. A reduced M_S and V might be the result of the interdiffusion, that is described in chap. 4.1.5. There is also good reason to assume that the active magnetic volume is smaller than the complete volume of the nanodot, that was determined from SEM micrographs. As was described in sec. 3.3, the nanodots are carved out of a thin film by argon ion milling. Therefore nanosized pillars are used as a shadow mask. These shadow masks are initially smaller in diameter than the resulting nanodots [202]. This observation might be explained by redeposition of sputtered material on the edges. The redeposited material is possibly a CoPt alloy, which reduces M_S . Another possibility is that the shadow mask expands during the ion milling process. The nanodot would then have the form of a truncated cone, explaining why the Co volume is smaller than for a cylinder.

Since the magnetic moment could not be quantified from the characteristics of the nanodot, an experimental method was developed to directly probe it. Therefore the nanodot is measured in the superparamagnetic regime, hence above the blocking

5 Investigation of single magnetic nanostructures

temperature. Telegraph noise data is recorded and the average switching time τ is determined. τ is described by the Néel-Arrhenius law $\tau = \tau_0 \exp(\frac{KV}{k_B T})$. When applying an external magnetic field parallel to the easy axis of magnetisation, one of the two states will be favoured and the average switching times of the upper state τ_+ and the lower state τ_- will differ. The Néel-Arrhenius law changes to $\tau_{\pm} = \tau_{0\pm} \exp(\frac{KV \pm mB}{k_B T})$ [203]. The logarithm of the ratio of τ_+ and τ_- is then calculated, which results in $\ln(\frac{\tau_+}{\tau_-}) = \ln(\frac{\tau_{0+}}{\tau_{0-}}) + \frac{2mB}{k_B T}$. $\frac{\tau_{0+}}{\tau_{0-}}$ is very close to 1 [1], so that $\ln(\frac{\tau_{0+}}{\tau_{0-}}) \approx 0$, which leads to the final equation

$$\ln\left(\frac{\tau_+}{\tau_-}\right) = \frac{2mB}{k_B T} \quad (5.7)$$

τ_+ and τ_- can be measured in the experiment, B and T are controlled by the experiment and k_B is a constant, thus m can be determined from a linear fit as is shown in fig. 5.15. Note that the measurement data had to be corrected, because of a residual field from the coils, which is about $100\mu\text{T}$. The measurement is performed at 245K and a magnetic moment $m = (2.3 \pm 0.2) \cdot 10^{-19} \text{ Am}^2$ is found. Using the magneton number of Co $1.75 \cdot \mu_B$ [48] a number of nearly 14000 free electrons in the nanodot can be estimated. Taking the literature value of $M_S = 1458 \text{ kA/m}$ [48] gives a diameter of 16.5 nm, nearly half the diameter measured by SEM (32 nm). On the other hand, the SEM radius gives a reduced M_S of about 500 kA/m, which is nearly one third of the literature value. This is also illustrated in fig. 5.16. The diameter of 16.5 nm can be understood as a lower limit of the nanodot, while the diameter found in the SEM (32 nm) is the upper limit. The anisotropy K and the volume V can not be determined separately from each other by the methods used in this thesis. Due to that, the product of both, KV , will be determined in the following investigations. Therefore the value of $m = (2.3 \pm 0.2) \cdot 10^{-19} \text{ Am}^2$ will be used.

5.2 Temperature dependence of the anisotropy in single magnetic nanostructures

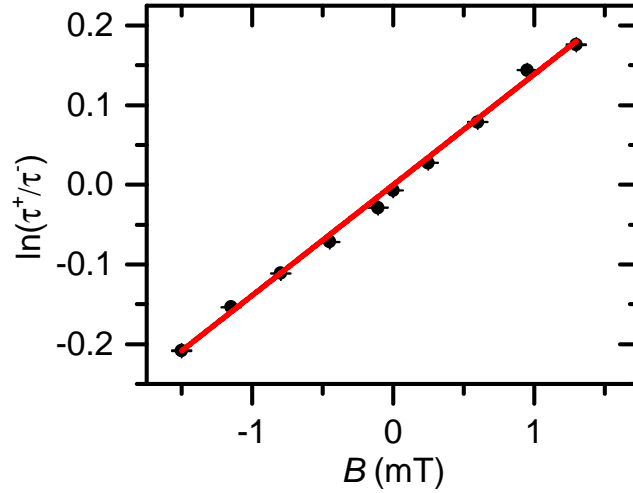


Figure 5.15: The magnetic moment m is determined. A magnetic field is applied in the easy axis of magnetisation of the superparamagnetic nanodot at 245 K. The occupation of the two states is altered with the external field and the average switching times are measured. With eq.5.7 the magnetic moment is determined from the natural logarithm of the ratio of τ_+ and τ_- . A magnetic moment of $m = (2.3 \pm 0.2) \cdot 10^{-19} \text{ Am}^2$ is determined.

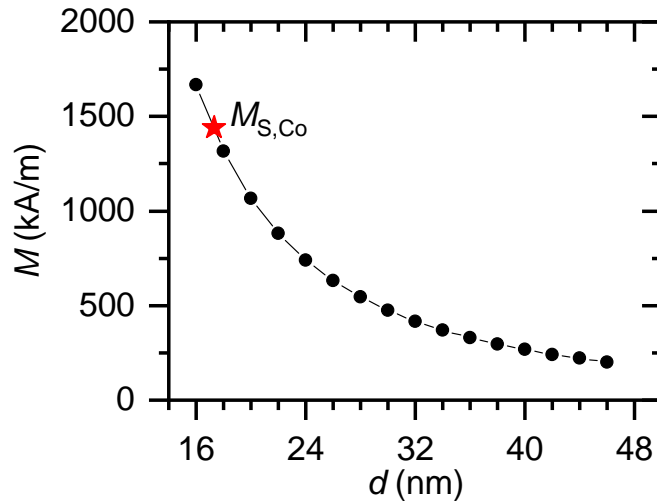


Figure 5.16: Using $M = m/V$, the magnetisation M is plotted over the diameter d of the nanodot. Under the assumption that the magnetisation is identical to the saturation magnetisation of Co a lower limit of the nanodot diameter can be determined, which is 16.5 nm. Otherwise the upper limit of the diameter, which is given by a SEM micrograph, results in a drastically reduced magnetisation.

5 Investigation of single magnetic nanostructures

5.2.3 Determination of anisotropy constants in nanostructures

The determination of the anisotropy in magnetic nanostructures is a difficult task. A method is used that induces spontaneous magnetisation reversal in an actually blocked nanodot. Therefore a magnetic field is applied in the hard axis of magnetisation. According to the Stoner-Wohlfarth model, the energy barrier, that is separating the two states of magnetisation, is reduced, while both states remain energetically equal, see fig. 5.17. Due to the reduction of the energy barrier a path for magnetisation reversal opens up in the blocked nanodot, allowing for spontaneous magnetisation reversal like in a superparamagnetic nanodot. In the Stoner-Wohlfarth model, when applying an external magnetic field parallel to the hard axis of magnetisation, the energy barrier of the nanodot is described by $\Delta E = KV(1 - H/H_K)^2$. This is inserted into the Néel-Arrhenius law, which leads to the expression:

$$\tau = \tau_0 \exp\left(\frac{KV}{k_B T} \left(1 - \frac{m \mu_0 H}{2KV}\right)^2\right) \quad (5.8)$$

Like in the superparamagnetic case, switching times can be determined that are in this case depending not only on the temperature but also on the magnetic field. The measurement data looks similar like in the case of a superparamagnetic nanodot. In the superparamagnetic case the occupation ratio is exactly at 50%. For the destabilisation measurement this is only true, when the field is applied exactly in the hard axis. Because of the inaccuracy of the experimental set-up, a small discrepancy occurs leading to a ratio of about 45 : 55. The effect on the switching time is negligible. This method makes it possible to measure field dependent switching times for a constant temperature.

Now, for a constant temperature the switching times can be determined for varying magnetic fields. To find the hard axis of magnetisation the angle between magnetic field and sample plane is altered until an equal occupation ratio is found. This is shown in fig. 5.18 for 150 K. The magnetic field is varied by about 10 mT from 164 mT to about 174 mT, which leads to a strong decrease of the average switching times from 1.04 s to 0.47 s, due to the exponential dependence from the magnetic field. For the pre-exponential factor τ_0 three values in accordance to Brown's theory were chosen. The fits are shown in fig. 5.18, where the different colors represent the different τ_0 . As can be seen all three fits give a satisfying

5.2 Temperature dependence of the anisotropy in single magnetic nanostructures

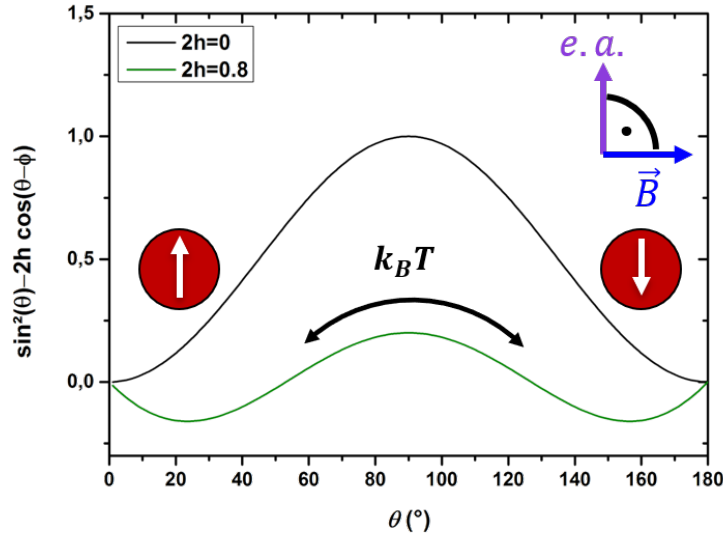


Figure 5.17: The change of the uniaxial energy landscape, when a magnetic field is applied in the hard axis of magnetisation. With increasing field, the energy barrier shrinks and the two minima move closer to another. Due to the change of the energy landscape less thermal energy is necessary to overcome the energy barrier. Thus, at temperatures, where the nanodot is supposed to be blocked, spontaneous magnetisation reversal like in the superparamagnetic regime can be induced. In the experiment, telegraph noise data is measured and average switching times can be determined in dependence of the applied magnetic field. The shrinking of the energy barrier in the Stoner-Wohlfarth model is given by $\Delta E(H) = KV \left(1 - \frac{H}{H_K}\right)^2$. This can be inserted in the Néel-Arrhenius law, giving a field dependent expression.

result, giving the following KV depending on τ_0 :

τ_0	KV
10^{-11} s	$8.6 \cdot 10^{-20}$ J
10^{-10} s	$8.1 \cdot 10^{-20}$ J
10^{-9} s	$7.6 \cdot 10^{-20}$ J

All values come with an error of $0.1 \cdot 10^{-20}$ J. Calculating $\frac{KV(150\text{K})}{k_B 150\text{K}}$ gives $\frac{KV}{k_B T} = 42$ for $\tau_0 = 10^{-11}$ s and $\frac{KV}{k_B T} = 37$ for $\tau_0 = 10^{-9}$ s. These values are in the expected range that was determined from the blocking temperature and also shows that the nanodot is well above the threshold of $\frac{KV}{k_B T} = 25$ for superparamagnetism at 150 K.

Since the aim is to determine the temperature dependency of KV , the measure-

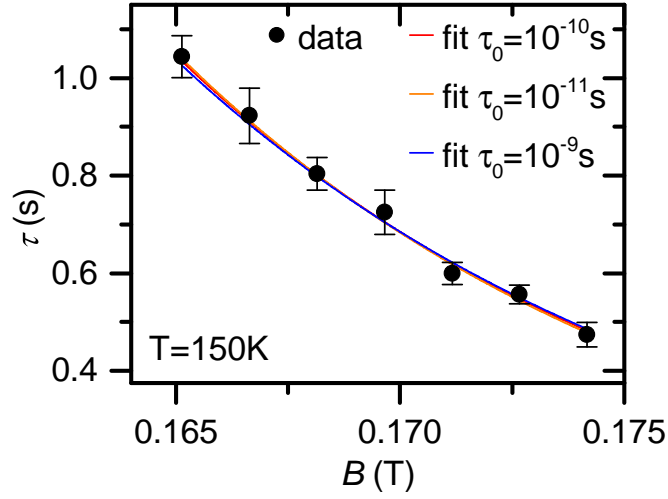


Figure 5.18: The average switching times are measured depending on the magnetic field for 150 K. To do this a magnetic field is applied in the hard axis of magnetisation inducing spontaneous magnetisation reversal. The magnetic field is increased from 165 mT to 174 mT. Despite the small field interval the switching time decreases by almost a factor of 2 from 1 s to 0.5 s. To determine KV , eq. 5.8 is fitted to the data using different τ_0 . The red line uses $\tau_0 = 10^{-10}$ s and the orange (blue) line $\tau_0 = 10^{-11}$ s ($\tau_0 = 10^{-9}$ s). All fits describe the data sufficiently.

ment is repeated over a broad temperature range from 80 K to 200 K, which can be seen in fig. 5.19. For each temperature the magnetic fields were chosen in a way, that the average switching times lie between 0.5 s and 1.5 s. As can also be seen in fig. 5.18 for 150 K the decrease of the switching times is very steep so that the magnetic field is only varied by about 10 mT. In fig. 5.19 only the fits for $\tau_0 = 10^{-10}$ s are shown for reasons of clarity, though also $\tau_0 = 10^{-11}$ s and $\tau_0 = 10^{-9}$ s were fitted.

The results are shown in fig. 5.20. The orange points represent the values obtained with a pre-exponential factor $\tau_0 = 10^{-11}$ s and the red (blue) points respective for $\tau_0 = 10^{-10}$ s ($\tau_0 = 10^{-9}$ s). The graphs show a similar albeit not identical behaviour. First the magnitude of KV is dependent on τ_0 , with smaller τ_0 resulting in higher values for KV . Second, all three graphs show that the magnetic anisotropy is in fact not constant over the temperature range, but overall exhibiting an increase with rising temperature. This increase seems to be almost linear from 77.5 K up to 175 K. Above 175 K the temperature dependence flattens for $\tau_0 = 10^{-11}$ s. For $\tau_0 = 10^{-10}$ s KV remains constant and for $\tau_0 = 10^{-9}$ s the slope changes sign.

5.2 Temperature dependence of the anisotropy in single magnetic nanostructures

Linear fits between 77.5 K and 175 K are applied resulting in the following slopes:

τ_0	KV_T
10^{-11} s	$1.4 \cdot 10^{-22}$ J/K
10^{-10} s	$1.1 \cdot 10^{-22}$ J/K
10^{-9} s	$0.8 \cdot 10^{-22}$ J/K

The error from the fit amounts to $0.1 \cdot 10^{-22}$ J/K for all slopes. The temperature dependence shows a good accordance to the results of ch. 4.1, where the temperature dependence of the anisotropy in thin films is investigated. In both cases an increase is found. For a better comparison the slopes are converted into an anisotropy K_T . The lower limit of the magnetic nanodot volume can be determined: $V = m/M_S = 160$ nm³. Using this volume, K_T is found to lie between 855 J/(Km³) ($\tau_0 = 10^{-11}$ s) and 507 J/(Km³) ($\tau_0 = 10^{-9}$ s). The upper limit is 460 nm³. This results in 304 J/(Km³) ($\tau_0 = 10^{-11}$ s) and 173 J/(Km³) ($\tau_0 = 10^{-9}$ s). This is of a similar magnitude as the slopes found in thin films in ch. 4.1. It can be concluded, that the sign and magnitude of the temperature dependence in the nanodot are in accordance to the films.

So far fixed τ_0 were used, based on general theoretical assumptions. Also the influence of the applied magnetic field on τ_0 has not been regarded. In order to account to τ_0 , the models developed by Coffey and Kalmykov [59] are utilized, which will be discussed in the next chapter.

5 Investigation of single magnetic nanostructures

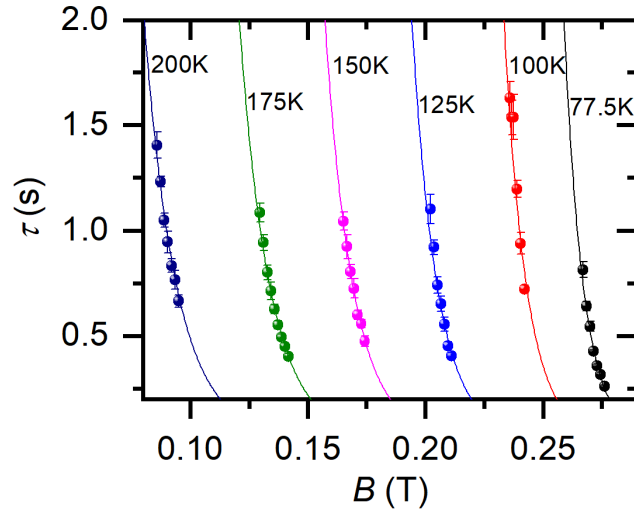


Figure 5.19: The average switching times depending on the magnetic field for six different temperatures between 77.5 K and 200 K. Eq. 5.8 is fitted to the data. For clarity reasons only the fits using $\tau_0 = 10^{-10}$ s are shown. Though fits using $\tau_0 = 10^{-11}$ s and $\tau_0 = 10^{-9}$ s were also performed. The determined KV are shown in fig. 5.20.

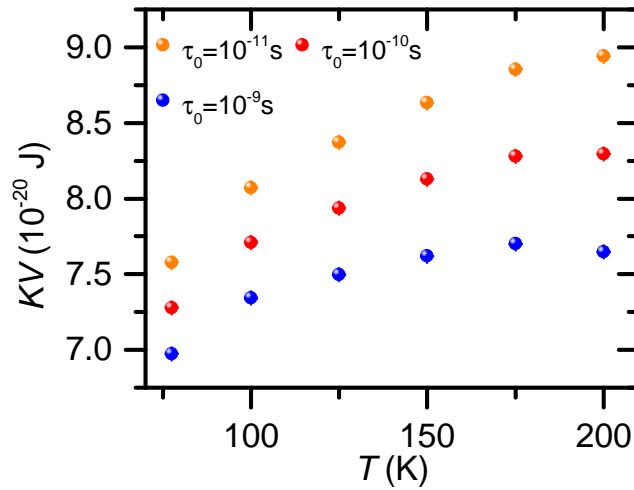


Figure 5.20: KV determined by fitting eq.5.8 to the measurement data shown in fig. 5.18 and 5.19. The red dots correspond to a pre-exponential factor of $\tau_0 = 10^{-10}$ s and the orange (blue) dots to $\tau_0 = 10^{-11}$ s ($\tau_0 = 10^{-9}$ s). KV increases with rising temperature showing that KV is not constant over temperature

5.2 Temperature dependence of the anisotropy in single magnetic nanostructures

5.2.4 Field dependent switching times based on Coffey and Kalmykov

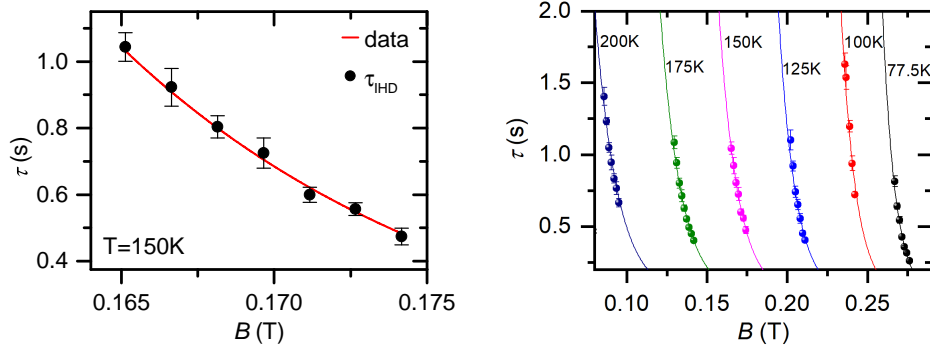


Figure 5.21: The average switching times depending on the magnetic field for 150 K and six different temperatures between 77.5 K and 200 K. This time eq. 2.29 by Kalmykov in the case of intermediate high damping is fitted to the data, which also fits well.

So far the influence of the magnetic field on the attempt frequency $f_0 = 1/\tau_0$ has been neglected. To investigate this issue, the field dependent formula given by Coffey and Kalmykov [59] are used. The authors described two cases, the intermediate high damping (IHD) for $\alpha > 1$ and the very low damping (VLD) $\alpha \ll 1$. For Co/Pt a damping constant of $\alpha = 0.3$ has been found by Metaxas et al. [204] and is assumed for our samples, which lies between IHD and VLD. In this case the authors give a general solution for the problem.

$$\tau = \tau_{\text{IHD}} \frac{A(\alpha S_1 + \alpha S_2)}{A(\alpha S_1)A(\alpha S_2)} \quad (5.9)$$

Since we assume that both potential wells are equivalent, $\frac{A(\alpha S_1 + \alpha S_2)}{A(\alpha S_1)A(\alpha S_2)} = \frac{A(2\alpha S)}{A(\alpha S)^2}$. For $\alpha = 0.3$ this results in $\frac{A(2\alpha S)}{A(\alpha S)^2} \approx 1$ [30]. For this reason the IHD case will be used further on, as it is a good approximation. Despite the complicated form of eq. 2.29, the model shows a good agreement to the measured data. Compared to a constant τ_0 , the same temperature dependence is found. The values lie between the values that were found for $\tau_0 = 10^{-10}\text{s}$ and $\tau_0 = 10^{-11}\text{s}$. In fig. 5.22 τ_0 is plotted over temperature. τ_0 lies between $2.8 \cdot 10^{-11}\text{s}$ at 77.5 K and $1.6 \cdot 10^{-11}\text{s}$ at 200 K. The determined τ_0 are within the same order of magnitude that is expected from Brown's theory. τ_0 is not constant, but decreases by almost a factor of 2. So far it was shown, that the anisotropy in a nanodot is not constant over temperature but increases, which is comparable to the behaviour in thin magnetic

5 Investigation of single magnetic nanostructures

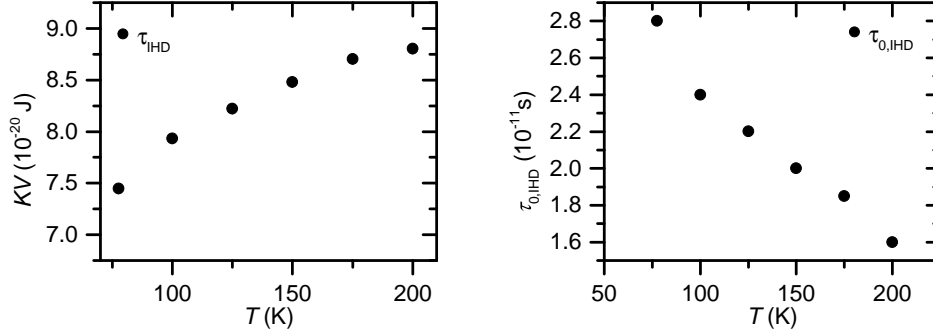


Figure 5.22: KV as determined from the equation for intermediate high damping. The temperature dependence of KV is in accordance as when using a constant τ_0 . The pre-exponential factor $\tau_{0,\text{IHD}}$, that was determined from the fit, is plotted over temperature. It is of the magnitude of 10^{-11} s and decreases with temperature.

films (see chap. 4.1). Nevertheless the question remains, how exactly the anisotropy in thin films and nanodots (that are carved out via ion milling from those films) are related. The nanostructure presented in this chapter was sputtered at the same time as the magnetic film, that was discussed in chap. 4.2.1. Therefore, both samples can be compared.

5.2.5 Comparing film and dot

The anisotropy of the Pt/Co/Pt film is determined by performing magnetoresistance measurements. This is the same method discussed in chap. 4.2.1. The film is investigated from 2 K up to 300 K. The anisotropy overall increases from 160 kJ/m³ at 2 K to 295 kJ/m³ at 250 K. Above this temperature the anisotropy becomes constant up to 300 K. Between 2 K and 250 K the increase can be described by linear relation, resulting in $K_T = (550 \pm 17) \frac{\text{K}}{\text{m}^3 \text{K}}$. For a better comparison between film and nanodot, the change in shape anisotropy is calculated. Therefore the model given by Millev et al. [37] is used. The model is shown in ch. 2.2 and applies well to magnetic nanodots. It assumes a cylindrical form of the nanodots. Though the exact geometrical shape of the nanodots is not known, Neumann et al. [114] proved the model to be sufficient, as other models using a truncated cone [205] or a truncated sphere give the same results. This comes from the fact that the film thickness t is significantly smaller than the nanodot diameter d . The change in shape anisotropy is dependent on the film thickness $t = 0.7$ nm and the

5.2 Temperature dependence of the anisotropy in single magnetic nanostructures

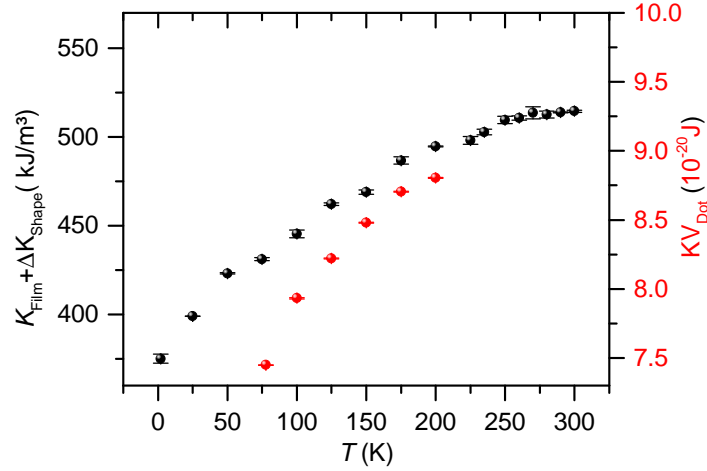


Figure 5.23: Comparing the anisotropy K of the film with KV of the nanodot. In both cases the anisotropy increases with temperature which is in accordance to the results found in sec. 4.1. Starting at 250 K the anisotropy of the film stops increasing. KV of the nanodot could not be determined up to that point, but it is likely to assume that it would behave similar.

diameter of the nanodot. In the previous chapter, a lower limit of the diameter is estimated from the measured magnetic moment m , which gives $d = 16.5$ nm. This results in a change of shape anisotropy between nanodot and film of maximal $\Delta K_{\text{Shape}} = 214$ kJ/m³.

Finally comparing film and nanodot overall a good agreement is found, which is shown in fig. 5.23. In both cases the anisotropy is increasing with temperature. The anisotropy increases linear in both film and dot up to 200 K. The anisotropy of the film reaches a plateau and remains constant above 250 K. This might also be the case for the nanodot though it was not possible to measure up to that point, because the nanodot becomes superparamagnetic at 220 K. The temperature dependence of the film is determined as $K_{T,\text{film}} = (550 \pm 17) \frac{\text{J}}{\text{m}^3\text{K}}$. For the nanodot $KV_{T,\text{dot}} = (1.34 \pm 0.08) \cdot 10^{-22} \frac{\text{J}}{\text{K}}$ is found. Using the lower limit for the diameter this gives $K_{T,\text{dot}} = (848 \pm 50) \frac{\text{J}}{\text{m}^3\text{K}}$. With the upper limit $K_{T,\text{dot}} = (291 \pm 50) \frac{\text{J}}{\text{m}^3\text{K}}$ can be determined. Both values are very close to the value of the film.

The found temperature dependence $KV_{T,\text{dot}} = (1.34 \pm 0.08) \cdot 10^{-22} \frac{\text{J}}{\text{K}}$ yields a variation in the Néel-Arrhenius law of $\exp(KV/k_B) = 1.6 \cdot 10^4$. The temperature dependence of the anisotropy is probably not the only explanation of the unexpected values of the pre-exponential factor τ_0 . In our case, K_T has a positive sign,

5 Investigation of single magnetic nanostructures

which would further increase the discrepancy between the experimental determined pre-exponential factor and Brown's theory. Nevertheless, the findings prove that the anisotropy is not constant and thus a temperature dependent anisotropy needs to be considered, when applying the Néel-Arrhenius law to magnetic nanodots and nanoparticles.

6 Conclusion

The main focus of this thesis is the temperature dependence of magnetic properties in thin magnetic Pt/Co/Pt films and single nanodots. The film systems were fabricated by a combination of electron cyclotron resonance sputtering and DC magnetron sputtering techniques under ultra-high vacuum condition. To fabricate the nanostructures distinguished lithography techniques were used and further developed. Nanodots with a diameter below 20 nm were created via electron beam lithography. Before such small diameters could only be achieved by nanosphere lithography, which has the disadvantage of a random arrangement of the nanodots on the Hall bar. Furthermore, nanostructuring on ultra-thin silicon nitride membranes has been done. This is necessary for measurement techniques utilising x-ray transmission. A checkerboard with alternating magnetic hard and soft nanodots was created, as well as a stacked Kagome lattice of nanodots, which was used for magnetic x-ray holography.

For ultra-thin magnetic Pt/Co/Pt film systems a thorough investigation of the temperature dependence of magnetic anisotropy constants has been made for various layer thickness of the magnetic material, ranging from 1.5 nm and up to 30 nm, which is getting close to bulk behaviour. In this thickness regime the easy axis of the magnetisation lies within in the film plane. To investigate the impact of the substrate on the anisotropy constant, the magnetic films were prepared on silicon oxide and silicon nitride substrates. On both substrates the temperature dependence of the anisotropy behaves similar. At higher Co thickness the anisotropy decreases with an increase of temperature, which is in accordance to the behaviour of bulk Co. At a smaller thickness of the Co layer, the anisotropy increases with increasing temperature.

For a better understanding $K_{\text{eff}} \cdot t(t)$ plots have been made for different temperatures. By fitting linear equations to the data, the effective volume anisotropy $K_{V,\text{eff}}$ and the interface anisotropy K_S can be obtained from the slope and the

6 Conclusion

intercept. On the silicon nitride substrate two regimes emerged, that are called lower thickness regime and higher thickness regime. These regimes are the result of strain relaxation. Contrary, there is only one regime on the silicon oxide substrate. From the fits the individual temperature dependence of K_S and $K_{V,\text{eff}}$ could be determined. For both substrates the temperature dependence of K_S and $K_{V,\text{eff}}$ behave linear. K_S has a positive slope and $K_{V,\text{eff}}$ has a negative slope.

A model has been presented to explain the increase of the anisotropy. The conventional method that was used to determine the anisotropy constants, assumes sharp interfaces. However, at the two interfaces between Pt and Co and Co and Pt an interdiffusion zone emerges. In the intermixing zone a $\text{Co}_x\text{Pt}_{1-x}$ alloy is present. Due to the interdiffusion zone, the slope and the interface are not equivalent to the volume and interface anisotropy, but are superimposed with additional contributions. At lower Co concentration the Curie temperature T_C is reduced, which might be beneath the temperature at which the experiment is conducted. Thus the amount of ferromagnetic material is smaller than initially expected. This leads to a temperature dependent reduction of the saturation magnetisation. It was found that the saturation magnetisation of a nominal Co layer of $t_{\text{nom}} = 2 \text{ nm}$ is reduced by a factor of 0.8616 at 10 K and by a factor of 0.8456 at 300 K. This amounts to a difference of the shape anisotropy of 37 kJ/m^3 . Since the shape anisotropy is an in-plane contribution, this difference will result in an increase of the effective anisotropy.

The model proves that the assumption of sharp interfaces is problematic. Therefore, the conventional approach to determine the anisotropy of sputtered multilayers may result in wrong numbers. While the effect on the volume anisotropy is negligible, the interface anisotropy, which is determined by the intercept, differs strongly. The conventional approach yields too high numbers and overestimates K_S , as the interdiffusion zone leads to an offset in the intercept.

To further investigate the influence of the intermixing zone, films with a Co layer of $t \leq 1 \text{ nm}$ were prepared. These films exhibit an easy axis of magnetisation that is perpendicular to the film plane. It could be shown that the temperature dependence of the anisotropy is indeed positive and thus stems from the interfaces. During the investigation of the out-of-plane films an unexpected behaviour was found. Longitudinal field sweeps were applied. While the magnetisation is rotated into the plane of the film, a parabolic response becomes visible in the magneto-

resistance, which is the result of the magneto-resistance effects AMR and AIMR. Unlike previous measurements [26], the opening of the parabola changes the sign, when the temperature is increased. This is caused by an opposing temperature dependence of the magnetoresistance effects AMR and AIMR. At low temperatures the AMR dominates and at higher temperatures the AIMR. It is unclear where this behaviour stems from. The increase of the AIMR is similar to the increase of K_{eff} . This indicates a change of the electronic properties of the alloy, which influences the spin-orbit coupling. This also affects the magnetic volume anisotropy.

In the second part of the thesis, the magnetisation behaviour of single magnetic nanodots was investigated by using nanosized Hall bar magnetometry. First the angular dependence of the switching field has been measured in three dimensions. A strong deviation from the Stoner-Wohlfarth model was found. The three dimensional switching surface exhibits an ellipsoidal shape as well as no overall symmetry. A possible explanation was given by Staeck [1]. Due to the polycrystalline nature of the initial films, a single nanodot consists of a few grains. The crystal axis of the grains may be tilted in respect to the film normal. A possible result can be a tilted volume and interface anisotropy in respect to the shape anisotropy. Staeck set up a modified energy potential and used the method given by Thiaville [186, 187] to simulate the switching field surface. The simulation fits well to the experimental results and reproduces features like the ellipsoidal shape or the lack of symmetry. A very small nanodot has been created, whose diameter (16 nm) approaches the mean diameter of the grains (16 nm). The small size of the nanodot pointed out the limits of the measuring technique. A bad signal to noise ratio has been obtained, that could have been improved by reducing the size of the leads of the Hall bar. However a decreased durability of the Hall bar would be the consequence. Also the temperature range for the investigation becomes smaller, as superparamagnetic behaviour emerges at lower temperatures.

Finally a nanodot has been thoroughly investigated with the goal of determining the temperature dependence of the anisotropy. The angular dependence of the switching field shows a much better agreement to the Stoner-Wohlfarth model, making the sample a good candidate for the investigation. The nanodot was investigated in the superparamagnetic regime. The average switching times were determined for varying temperatures. The Néel-Arrhenius law was applied to the data and the pre-exponential factor was found to be in the range of $\tau_0 = 10^{14}$ s,

6 Conclusion

that deviates by orders of magnitude from the usually assumed GHz regime [7]. The temperature dependence of the switching field was measured. Fitting the theoretical equation given by Garg [60] revealed a pre-exponential factor in the range of $\tau_0 = 10^{14}$ s. Taking into account a temperature dependent anisotropy, as was found in the initial films, it is shown that this would alter the Néel-Arrhenius law. An additional exponential factor emerges that could explain the deviations of the pre-exponential factor from theoretical values. A big obstacle proved to be the exact knowledge of the magnetic moment. This was determined by applying an external field parallel to the easy axis of magnetisation, which alters the occupation probability of the two states of magnetisation. Using this method a value of the magnetic moment $m = (2.3 \pm 0.2) \cdot 10^{-19}$ Am² was found at 245 K. A lower and upper limit of the nanodot volume could be estimated. To determine the magnetic anisotropy, the nanodot was investigated in the blocked regime. By applying a magnetic field parallel to the hard axis of magnetisation, the energy barrier is lowered and spontaneous magnetisation reversal is induced, that is similar to the magnetisation reversal in the superparamagnetic regime. By using a field dependent Néel-Arrhenius law, the temperature dependence of the anisotropy in a nanodot is determined to be $K_{T,\text{dot}} = (848 \pm 50) \frac{\text{J}}{\text{m}^3\text{K}}$ in the lower limit and $K_{T,\text{dot}} = (291 \pm 50) \frac{\text{J}}{\text{m}^3\text{K}}$. This is in accordance to the value obtained for the initial film that lies at $K_{T,\text{film}} = (550 \pm 17) \frac{\text{J}}{\text{m}^3\text{K}}$, which shows that the temperature dependence of the anisotropy is passed on from the initial film to the nanodot. The proposed idea that the temperature dependent anisotropy fixes the value of the pre-exponential factor does not hold up for the nanodot, as the temperature dependence has the wrong sign. Nevertheless it was shown that the anisotropy in the nanodot is inherited from the magnetic film and is not constant.

Future investigations of single nanostructures can be performed in mono-crystalline structures, that do not consist of grains. These could be made by molecular-beam epitaxy. The occurrence of grains makes the description of single nanodots very difficult, as complicated energy terms may arise. Mono-crystalline structures would simplify the theoretical description of the nanodots. Also, the influence of the grains should be further investigated.

Future investigations of magnetic films should further elaborate on the effects that occur in the interfaces. Bulk behaviour can not be transferred to ultra thin systems, that are dominated by the interfaces. Further theoretical investigation

should be performed for a better understanding of the effect at interfaces. The proposed model is only a simplification of the real structure. The model can be extended to distinguish between both interfaces. Finally, the found behaviour of the AIMR should be investigated in more detail. So far only the SiO_2 substrate was measured. The measurements should also be made for a Si_3N_4 substrate.

In conclusion, the thesis proves that often overlooked properties, like the interfaces in metallic multilayers or the tilting of the grain structure, can have a significant influence on the magnetic properties of films and nanostructures and should not be neglected.

Bibliography

- [1] P. Staeck, *Untersuchungen zur Wechselwirkung von magnetischen Nanostrukturen mittels Magnetotransport*, Ph.D. thesis (2018) (cit. on pp. [iii](#), [v](#), [3](#), [87](#), [89](#), [90](#), [94](#), [95](#), [102](#), [115](#)).
- [2] A. Moser, K. Takano, D. T. Margulies, M. Albrecht, Y. Sonobe, Y. Ikeda, S. Sun, and E. E. Fullerton, «Magnetic recording: advancing into the future», *J. Phys. D: Appl. Phys.* **35**, R157 (2002) (cit. on p. [1](#)).
- [3] M. N. Baibich, J. M. Broto, A. Fert, F. Nguyen Van Dau, F. Petroff, P. Eitenne, G. Creuzet, A. Friederich, and J. Chazelas, «Giant magnetoresistance of (001)Fe/(001)Cr magnetic superlattices», *Phys. Rev. Lett.* **61**, 2472 (1988) (cit. on p. [1](#)).
- [4] G. Binasch, P. Grünberg, F. Saurenbach, and W. Zinn, «Enhanced Magnetoresistance In Layered Magnetic-Structures With Antiferromagnetic Interlayer Exchange», *Phys. Rev. B* **39**, 4828 (1989) (cit. on p. [1](#)).
- [5] S. Iwasaki and Y. Nakamura, «An analysis for the magnetization mode for high density magnetic recording», *IEEE Transactions on Magnetics* **Mag-13** (1977) (cit. on p. [1](#)).
- [6] M. Plumer, J. van Ek, and D. Weller (Eds.), *The Physics of Ultra-High-Density Magnetic Recording* (Springer-Verlag Berlin Heidelberg GmbH, 2001) (cit. on pp. [1](#), [2](#)).
- [7] C. P. Bean and J. D. Livingston, «Superparamagnetism», *J. Appl. Phys.* **30**, 120S (1959) (cit. on pp. [1](#), [98](#), [116](#)).
- [8] D. Weller and A. Moser, «Thermal effect limits in ultrahigh-density magnetic recording», *IEEE Trans. Magn.* **35**, 4423 (1999) (cit. on p. [2](#)).

Bibliography

- [9] J. R. Childress and R. E. Fontana Jr., «Magnetic recording read head sensor technology», *C. R. Phys.* **6**, 997 (2005) (cit. on p. 2).
- [10] D. Weller, G. Parker, O. Mosendz, E. Champion, B. Stipe, X. Wang, T. Klemmer, G. Ju, and A. Ajan, «A HAMR Media Technology Roadmap to an Areal Density of 4 Tb/in²», *IEEE Transactions on Magnetics* **50** (2014) (cit. on p. 2).
- [11] J. Zhu, X. Zhu, and Y. Tang, «Microwave assisted magnetic recording», *IEEE Transactions on Magnetics* **44** (2008) (cit. on p. 2).
- [12] S. Okamoto, N. Kikuchi, M. Furuta, O. Kitakami, and T. Shimatsu, «Microwave assisted magnetic recording technologies and related physics», *Journal of Physics D: Applied Physics* **48** (2015) (cit. on p. 2).
- [13] M. Günsch, «Neue Roadmap: Western Digital plant Jahre mit „ePMR“ vor MAMR oder HAMR», (2020) (cit. on p. 2).
- [14] D. Apalkov, B. Dieny, and J. M. Slaughter, «Magnetoresistive Random Access Memory», *Proc. of the IEEE* **104** (2016) (cit. on p. 2).
- [15] U. Gradman, «Struktur und Ferromagnetismus sehr dünner, epitaktischer Ni-Flächenschichten», *Ann. Phys. Lpz.* **17** (1966) (cit. on p. 2).
- [16] P. F. Carcia, A. D. Meinhold, and A. Suna, «Perpendicular magnetic anisotropy in Pd/Co thin film layered structures», *Appl. Phys. Lett.* **47** (cit. on p. 2).
- [17] P. Carcia, «Perpendicular magnetic anisotropy in Pd/Co and Pt/Co thin-film layered structures», *Journ. Appl. Phys.* **63** (1998) (cit. on p. 2).
- [18] F. den Broeder, D. Kuiper, A. P. van de Mosselaer, and W. Hoving, «Perpendicular Magnetic Anisotropy of Co-Au Multilayers Induced by Interface Sharpening», *Phys. Rev. Lett.* **60** (1988) (cit. on p. 2).
- [19] M. Sakurai, T. Takahata, and I. Moritani, «Magnetic and Magneto-Optical Properties of Co/Ru Multilayers», *J. Magn. Soc. Japan* **15**, 411 (1991) (cit. on p. 2).

- [20] F. den Broeder, W. Hoving, and P. Bloemen, «Magnetic anisotropy of multilayers», *Journal of Magnetism and Magnetic Materials* **93**, 562 (1991) (cit. on p. 2).
- [21] M. Wellhöfer, *Herstellung ultradünner magnetischer Co/Pt-Filme mit Hilfe der ECR-Ionenätztechnik und Charakterisierung*, Master's thesis, Universität Hamburg (2003) (cit. on pp. 2, 25, 37).
- [22] M. Wellhöfer, M. Weissenborn, R. Anton, S. Pütter, and H. P. Oepen, «Morphology and magnetic properties of ECR ion beam sputtered Co/Pt films», *J. Magn. Magn. Mater.* **292**, 345–358 (2005) (cit. on pp. 2, 25, 37).
- [23] H. Stillrich, *Magnetische Nanostrukturen basierend auf Co/Pt-Multilagern, hergestellt mittels selbstorganisierter Masken aus Blockcopolymer-Micellen*, Ph.D. thesis, Universität Hamburg (2007) (cit. on pp. 2, 25, 37).
- [24] H. Stillrich, C. Menk, R. Fromter, and H. P. Oepen, «Magnetic anisotropy and the cone state in Co/Pt multilayer films», *J. Appl. Phys.* **105**, 07C308 (2009) (cit. on pp. 2, 25, 37).
- [25] H. Stillrich, C. Menk, R. Fromter, and H. P. Oepen, «Magnetic anisotropy and spin reorientation in Co/Pt multilayers: Influence of preparation», *J. Magn. Magn. Mater.* **322**, 1353–1356 (2010) (cit. on pp. 2, 25, 37).
- [26] A. Kobs, *Magnetogalvanic effects in ferromagnets of reduced dimensions*, Ph.D. thesis, Universität Hamburg (2013) (cit. on pp. 2, 3, 25, 37, 39, 48, 53, 72, 73, 75, 115).
- [27] G. Winkler, A. Kobs, A. Chuvillin, D. Lott, A. Schreyer, and H. Oepen, «On the variation of magnetic anisotropy in Co/Pt(111) on silicon oxide», *Journal of Applied Physics* **117**, 105306 (2015) (cit. on pp. 2, 25, 37, 39, 48, 52, 53, 57).
- [28] C. Ross, «Patterned magnetic recording media», *Annu. Rev. Mater. Res.* **31**, 203 (2001) (cit. on p. 3).
- [29] A. Neumann, *Magnetisierungsverhalten einzelner ferromagnetischer Nanostrukturen*, Ph.D. thesis, Universität Hamburg (2014) (cit. on pp. 3, 15, 19, 29, 93, 99).

Bibliography

- [30] C. Thoenissen, *Magnetische Eigenschaften von einzelnen Co/Pt- und Co-Nanostrukturen*, Ph.D. thesis (2019) (cit. on pp. 3, 29, 109).
- [31] E.-S. Wilhelm, «Influence of the local grain structure on the magnetization reversal behavior of ferromagnetic Co/Pt nanodots», (2020) (cit. on pp. 3, 27, 93, 94).
- [32] S. Freercks, S. Hesse, A. Neumann, P. Staeck, C. Thoenissen, E.-S. Wilhelm, and H. Oepen, «Magnetic Behavior of Single Nanostructures and Their Mutual Interactions in Small Ensembles», in *Atomic- and Nanoscale Magnetism*, edited by R. Wiesendanger (Springer, 2018) (cit. on pp. 3, 99).
- [33] R. C. O’Handley, *Modern Magnetic Materials: Principles and Applications* (John Wiley & Sons Inc., 2000) (cit. on p. 5).
- [34] S. Chikazumi, *Physics of Ferromagnetism* (Oxford Press, 2009) (cit. on p. 5).
- [35] S. Blundell, *Magnetism in Condensed Matter* (Oxford University Press Inc., New York, 2006) (cit. on p. 5).
- [36] E. Kneller, *Ferromagnetismus* (Springer-Verlag Berlin / Göttingen / Heidelberg, 1962) (cit. on p. 5).
- [37] Y. Millev, E. Vedmedenko, and H. Oepen, «Dipolar magnetic anisotropy energy of laterally confined ultrathin ferromagnets: multiplicative separation of discrete and continuum contributions», *J. Phys. D: Appl. Phys.* **36**, 2945 (2003) (cit. on pp. 8, 89, 110).
- [38] D. Sander, R. Skomski, A. Enders, C. Schmidhals, D. Reuter, and J. Kirschner, «The correlation between mechanical stress and magnetic properties of ultrathin films», *J. Phys. D: Appl. Phys.* **31**, 663 (1998) (cit. on p. 9).
- [39] D. Sander, A. Enders, and J. Kirschner, «Stress and magnetic properties of surfaces and ultrathin films», *J. Magn. Magn. Mater.* **200**, 439 (1999) (cit. on pp. 9, 52).

- [40] D. Sander, «The correlation between mechanical stress and magnetic anisotropy in ultrathin films», *Rep. Prog. Phys.* **62**, 809 (1999) (cit. on pp. 9, 10, 52).
- [41] D. Sander, H. Meyerheim, S. Ferrer, and J. Kirschner, «Stress, Strain and Magnetic Anisotropy: All Is Different in Nanometer Thin Films», in *Advances in Solid State Physics*, Vol. 43 of *Advances in Solid State Physics*, edited by B. Kramer, pp. 547–562 (Springer Berlin Heidelberg, 2003) (cit. on p. 9).
- [42] C. Kittel, «Physical Theory of Ferromagnetic Domains», *Rev. Mod. Phys.* **21**, 541 (1949) (cit. on p. 9).
- [43] E. W. Lee, «Magnetostriction and Magnetomechanical Effects», *Rep. Prog. Phys.* **18**, 184 (1955) (cit. on p. 9).
- [44] R. Becker and W. Döring, *Ferromagnetismus* (Springer, 1939) (cit. on p. 10).
- [45] W. J. Carr Jr., *Secondary Effects in Ferromagnetism* (Springer, 1966) (cit. on p. 10).
- [46] A. Hubert and R. Schäfer, *Magnetic Domains* (Springer-Verlag Berlin Heidelberg, 1998) (cit. on pp. 11, 12).
- [47] R. Skomski, H.-P. Oepen, and J. Kirschner, «Micromagnetics of ultrathin films with perpendicular magnetic anisotropy», *Phys. Rev. B* **58**, 3223 (1998) (cit. on p. 11).
- [48] J. Crangle, «LIX. The magnetic moments of cobalt-copper alloys», *Philos. Mag.* **46** (1955) (cit. on pp. 12, 38, 68, 102).
- [49] E. C. Stoner and E. P. Wohlfarth, «A Mechanism of Magnetic Hysteresis in Heterogeneous Alloys», *Philosophical Transactions of the Royal Society of London. Series A, Mathematical and Physical Sciences* **240**, 599 (1948) (cit. on p. 13).
- [50] E. Stoner and E. Wohlfarth, «A mechanism of magnetic hysteresis in heterogeneous alloys», *IEEE Trans. Magn.* **27**, 3475 (1991) (cit. on p. 13).

Bibliography

- [51] C. Tannous and J. Gieraltowski, «The Stoner-Wolfarth model of ferromagnetism», *Eur. J. Phys.* **29**, 475 (2008) (cit. on p. 13).
- [52] H. Pfeiffer, «Determination of anisotropy field distribution in particle assemblies taking into account thermal fluctuations», *Phys. Stat. Sol. (a)* **118**, 295 (1990) (cit. on p. 14).
- [53] H. Kronmüller, K.-D. Durst, and G. Martinek, «Angular dependence of the coercive field in sintered $\text{Fe}_{77}\text{Nd}_{15}\text{B}_8$ magnets», *J. Magn. Magn. Mater.* **69**, 149 (1987) (cit. on p. 15).
- [54] C.-R. Chang, «Micromagnetic studies of coherent rotation with quartic crystalline anisotropy», *J. Appl. Phys.* **69**, 2431 (1991) (cit. on pp. 15, 91).
- [55] E. Kondorsky, «On Hysteresis in Ferromagnetics», *J. Phys. (Moscow)* **II**, 161 (1940) (cit. on p. 17).
- [56] L. Néel, «Théorie du traînage magnétique des ferromagnétiques en grains fins avec applications aux terres cuites», *Ann. Géophys* **5**, 99 (1949) (cit. on p. 17).
- [57] J. W. F. Brown, «Relaxational Behavior of Fine Magnetic Particles», *J. Appl. Phys.* **30**, S130 (1959) (cit. on p. 17).
- [58] W. F. Brown, «Thermal Fluctuations of a Single-Domain Particle», *Phys. Rev.* **130**, 1677 (1963) (cit. on p. 17).
- [59] W. T. Coffey and Y. P. Kalmykov, «Thermal fluctuations of magnetic nanoparticles: Fifty years after Brown», *J. Appl. Phys.* **112**, 121301 (2012) (cit. on pp. 18, 107, 109).
- [60] A. Garg, «Escape-field distribution for escape from a metastable potential well subject to a steadily increasing bias field», *Phys. Rev. B* **51**, 15592 (1995) (cit. on pp. 19, 92, 98, 116).
- [61] W. Thomson, «On the electro-dynamic qualities of metals: Effects of magnetization on the electric conductivity of Nickel and of Iron», *Proceedings of the Royal Society of London* **8**, 546 (1856) (cit. on p. 21).

- [62] J. Smit, «Magnetoresistance of ferromagnetic metals and alloys at low temperatures», *Physica* **17**, 612 (1951) (cit. on p. 21).
- [63] L. Berger, «Influence of spin-orbit interaction on the transport processes in ferromagnetic nickel alloys, in the presence of a degeneracy of the 3d band», *Physica* **30**, 1141 (1964) (cit. on p. 21).
- [64] R. Potter, «Magnetoresistance anisotropy in ferromagnetic NiCu alloys», *Phys. Rev. B* **10**, 4626 (1974) (cit. on p. 21).
- [65] T. McGuire and R. Potter, «Anisotropic magnetoresistance in ferromagnetic 3d alloys», *IEEE Trans. Magn.* **11**, 1018 (1975) (cit. on p. 21).
- [66] A. Kobs and H. Oepen, «Disentangling interface and bulk contributions to the anisotropic magnetoresistance in Pt/Co/Pt sandwiches», *Phys. Rev. B* p. 014426 (2016) (cit. on p. 21).
- [67] A. Kobs, S. Hesse, W. Kreuzpainter, G. Winkler, D. Lott, P. Weinberger, A. Schreyer, and H. Oepen, «Anisotropic Interface Magnetoresistance in Pt/Co/Pt Sandwiches», *Phys. Rev. Lett.* **106**, 217207 (2011) (cit. on pp. 21, 22).
- [68] A. Kobs, A. Frauen, H. Oepen, and P. Weinberg, «Anisotropic interface magnetoresistances in Pt(111)/Co_n/Pt(111)», *Philos. Mag.* 92 p. 2385 (2012) (cit. on p. 21).
- [69] W. Gil, D. Görlitz, M. Horisberger, and J. Kötzler, «Magnetoresistance anisotropy of polycrystalline cobalt films: Geometrical-size and domain effects», *Phys. Rev. B* **72**, 134401 (2005) (cit. on p. 22).
- [70] J. L. Olsen, *Electron Transport in Metals - Interscience Tracts on Physics and Astronomy 12* (Interscience Publishers, a division of John Wiley & Sons, 1962) (cit. on p. 22).
- [71] C. M. Hurd, «Galvanomagnetic Effects In Anisotropic Metals», *Adv. Phys.* **23**, 315 (1974) (cit. on p. 22).
- [72] F. Bloch, «Zur Theorie des Ferromagnetismus», *Zeitschrift für Physik* **61**, 206 (1930) (cit. on pp. 22, 38).

Bibliography

- [73] M. Stearns, *Landolt-Börnstein - Group III: Condensed Matter, Numerical Data and Functional Relationships in Science and Technology, Vol 19a: 3d, 4d and 5d Elements, Alloys and Compounds*, chap. 1.1.2 Fe, Co, Ni, pp. 24–141 (Springer-Verlag Berlin, 1986) (cit. on pp. 22, 38).
- [74] L.-F. Liu, W.-Y. Zhou, S.-S. Xie, O. Albrecht, and K. Nielsch, «Microstructure and temperature-dependent magnetic properties of Co/Pt multilayered nanowires», *Chem. Phys. Lett.* **466**, 166 (2008) (cit. on p. 22).
- [75] D. Zhang, K. J. Klabunde, C. M. Sorensen, and G. Hadjipanayis, «Magnetization temperature dependence in iron nanoparticles», *Phys. Rev. B* **58**, 14167 (1998) (cit. on p. 22).
- [76] M. Zheng, L. Menon, H. Zeng, Y. Liu, S. Bandyopadhyay, R. Kirby, and D. Sellmyer, «Magnetic properties of Ni nanowires in self-assembled arrays», *Phys. Rev. B* **62**, 12282 (2000) (cit. on p. 22).
- [77] M. Wu, Y. Zhang, S. Hui, T. Xiao, G. Shihui, W. Hines, and J. Budnick, «Temperature dependence of magnetic properties of SiO₂-coated Co nanoparticles», *J. Magn. Magn. Mater.* **268**, 20 (2004) (cit. on p. 22).
- [78] P. Kapitza, «The change of electrical conductivity in strong magnetic fields. Part I. Experimental results», *Proc. R. Soc. A* **123**, 292 (1929) (cit. on p. 23).
- [79] A. Mihai, J. Attane, A. Marty, P. Warin, and Y. Samson, «Electron-magnon diffusion and magnetization reversal detection in FePt thin films», *Phys. Rev. B* **77**, 060401 (R) (2008) (cit. on p. 23).
- [80] E. H. Hall, «On a New Action of the Magnet on Electric Currents», *Amer. J. Math.* **2**, 287 (1879) (cit. on p. 23).
- [81] E. Hall, «XXXVIII. On the new action of magnetism on a permanent electric current», *Philosophical Magazine Series 5* **10**, 301 (1880) (cit. on p. 23).
- [82] E. Hall, «XXIX. On a new action of the magnet on electric currents», *Philosophical Magazine Series 5* **9**, 225 (1880) (cit. on p. 23).

- [83] E. Hall, «XVIII. On the "Rotational Coefficient" in nickel and cobalt», *Philosophical Magazine Series 5* **12**, 157 (1881) (cit. on p. 23).
- [84] C. M. Hurd, *The Hall Effect in Metals and Alloys* (Plenum Press, New York, 1972) (cit. on p. 24).
- [85] J. Wagner, *The magnetic properties of ultrathin Cobalt multilayers symmetrically and antisymmetrically sandwiched between layers of platinum and iridium*, Ph.D. thesis (2019) (cit. on pp. 33, 34).
- [86] N. Akulov, «Zur Quantentheorie der Temperaturabhängigkeit der Magnetisierungskurve», *Z. Physik* **100**, 197 (1936) (cit. on p. 38).
- [87] J. Van Vleck, «On the Anisotropy of Cubic Ferromagnetic Crystals», *Advanced Materials* **52** (1936) (cit. on p. 38).
- [88] C. Zener, «Classical Theory of the Temperature Dependence of Magnetic Anisotropy Energy*», *Physical Review* **96** (1954) (cit. on p. 38).
- [89] F. Keffer, «Temperature Dependence of Ferromagnetic Anisotropy in Cubic Crystals*», *Physical Review* **100** (1955) (cit. on p. 38).
- [90] W. J. Carr Jr., «Theory of Ferromagnetic Anisotropy», *Physical Review* **108** (1957) (cit. on p. 38).
- [91] W. J. Carr Jr., «Temperature Dependence of Ferromagnetic Anisotropy», *Phys. Rev.* **109** (1958) (cit. on p. 38).
- [92] C. Kittel and J. H. Van Vleck, «Theory of the Temperature Dependence of the Magnetoelastic Constants of Cubic Crystals», *Physical Review* **118** (1960) (cit. on p. 38).
- [93] H. Callen and E. Callen, «Magnetostriction, Forced Magnetostriction, and Anomalous Thermal Expansion in Ferromagnets*», *Phys. Rev.* **139** (1965) (cit. on p. 38).
- [94] H. Callen and E. Callen, «The present status of the temperature dependence of magnetocrystalline anisotropy, and the $l(l+1)2$ power law», *J. Phys. Chem. Solids* **27**, 1271 (1966) (cit. on p. 38).

Bibliography

- [95] P. J. Jensen and K. H. Bennemann, «Theoretical study of the temperature dependence of the width of magnetic domain walls», *Annalen der Physik* **2**, 475 (1993) (cit. on p. 38).
- [96] M. Kuz'min, «Shape of Temperature Dependence of Spontaneous Magnetization of Ferromagnets: Quantitative Analysis», *Phys. Rev. Lett.* **94**, 107204 (2005) (cit. on pp. 38, 59, 61, 68).
- [97] W. Sucksmith and J. E. Thompson, «The Magnetic Anisotropy of Cobalt», *Proc. R. Soc. Lond. A* **225**, 362 (1954) (cit. on p. 39).
- [98] R. Bozorth, «Magnetostriction and crystal anisotropy of single crystals of hexagonal cobalt», *Phys. Rev.* **96** (1954) (cit. on p. 39).
- [99] Y. Barnier, R. Pauthenet, and G. Rimet, «Study of the change of easy direction of magnetization in cobalt», *C.R. Acad. Sci.* **253** (1961) (cit. on p. 39).
- [100] J. Kouvel and C. Hartelius, «Effect of hydrostatic pressure on the magnetocrystalline anisotropy of cobalt», *J. Phys. Chem. Solids* **25** (1965) (cit. on p. 39).
- [101] Y. Kadena, «Temperature dependence of magnetocrystalline anisotropy in cobalt», *J. Sci. Hiroshima Univ. Ser. AII.* **31** (1967) (cit. on p. 39).
- [102] V. Sievert, J.D. and Zehler, «The magnetic anisotropy of silicon-iron», *Z. Angew. Phys.* **30** (1970) (cit. on p. 39).
- [103] J. Burd, M. Huq, and E. Lee, «The determination of magnetic anisotropy constants from torque curves», *J. Magn. Magn. Mat.* **135** (1977) (cit. on p. 39).
- [104] M. Takahashi, S. Kadowaki, T. Wakiyama, T. Anayama, and M. Takahashi, «Magnetocrystalline Anisotropy of Co and Co–Ni Alloys», *J. Phy. Soc. Japan* **44** (1978) (cit. on p. 39).
- [105] M. Takahashi and T. Suzuki, «Temperature dependence of magnetic domain structures in HCP cobalt single crystals», *Japan. J. Appl. Phys.* **18** (1979) (cit. on p. 39).

- [106] F. Ono and O. Yamada, «Temperature dependence of the uniaxial magnetocrystalline anisotropy energy of Co», *J. Phys. Soc. Japan* **46** (1978) (cit. on p. 39).
- [107] F. Ono, «Magnetic field dependence of the magnetocrystalline anisotropy energy in hcp Co», *J. Phys. Soc. Japan* **50** (1981) (cit. on p. 39).
- [108] D. Paige, B. Szpunar, and B. Tanner, «The magnetocrystalline anisotropy of cobalt», *Journ. Magn. Magn. Mat.* **44**, 239 (1984) (cit. on pp. 39, 53).
- [109] T. Suzuki, D. Weller, C.-A. Chang, R. Savoy, T. Huang, B. A. Gumez, and V. Speriosu, «Magnetic and magneto-optic-properties of thick face-centered-cubic Co single-crystal films», *Appl. Phys. Lett.* **64** (1994) (cit. on pp. 39, 53).
- [110] M. T. Johnson, P. J. H. Bloemen, F. J. A. den Broeder, and J. J. de Vries, «Magnetic anisotropy in metallic multilayers», *Rep. Prog. Phys.* **59**, 1409 (1996) (cit. on p. 49).
- [111] S. J. Greaves, A. K. Petford-Long, Y. Kim, R. J. Pollard, P. J. Grundy, and J. P. Jakubovics, «A magnetic and high-resolution structural investigation of Pt/Co multilayers», *J. Magn. Magn. Mat.* **113** (1992) (cit. on p. 49).
- [112] D. Weller, A. Carl, R. Savoy, T. Huang, M. Toney, and C. Chappert, «Structural transitions and magnetic-anisotropy in ultrathin Co wedges on Pt(111) investigated with the magneto-optical Kerr-effect», *Phys. Chem. Solids* **56** (1995) (cit. on p. 49).
- [113] T. Kingetsu, «“Molecular-beam-epitaxial growth and magnetic-properties of (111)Pt/Co/Ag, Pt/Co, and Ag/Co/Pt superlattices», *J. Appl. Phys.* **76** (1994) (cit. on p. 49).
- [114] A. Neumann, A. Frauen, J. Vollmers, A. MEyer, and H. Oepen, «Structure-induced spin reorientation in magnetic nanostructures», *Phys. Rev. B.* **94**, 23162 (2016) (cit. on pp. 52, 110).
- [115] P. M. Marcus and V. L. Moruzzi, «Equilibrium properties of the cubic phases of cobalt», *Solid State Communications* **55** (cit. on pp. 52, 56).

Bibliography

- [116] J. H. Van der Merwe, «Crystal Interfaces. Part II. Finite Overgrowths», *J. Appl. Phys.* **34** (1963) (cit. on p. 52).
- [117] R. Jungblut, M. T. Johnson, J. aan de Stegge, A. Reinders, and F. J. A. den Broder, «Orientational and structural dependence of magnetic anisotropy of Cu/Ni/Cu sandwiches: Misfit interface anisotropy», *J. Appl. Phys.* **75** (1994) (cit. on p. 52).
- [118] H. Takahashi, S. Tsunashima, S. Iwata, and S. Uchiyama, «Measurement of magnetostriction constants in polycrystalline alloy and multilayer films of PdCo and PtCo», *J. Magn. Magn. Mater.* **126**, 282 (1993) (cit. on p. 52).
- [119] Y. S. Touloukian, *Thermophysical properties of matter. Vol. 12, Thermal expansion : metallic elements and alloys* (IFI/Plenum, New York, 1975) (cit. on pp. 55, 56).
- [120] R. L. Stamps, L. Louail, M. Hehn, M. Gester, and K. Ounadjela, «Anisotropies, cone states, and stripe domains in Co/Pt multilayers», *J. Appl. Phys.* **81**, 4751 (1997) (cit. on p. 55).
- [121] L. Louail, K. Ounadjela, and R. Stamps, «Temperature-dependent thin-film cone states in epitaxial Co/Pt multilayers», *Journ. Magn. Magn. Mat.* **167**, L189 (1997) (cit. on p. 55).
- [122] T. Sugimoto, T. Katayama, Y. Suzuki, M. Hashimoto, Y. Nishihara, A. Ito, and K. Kawanishi, «Temperature dependence of perpendicular magnetic anisotropy in Co/Au and Co/Pt multilayers», *Journ. Magn. Magn. Mat.* **104-107**, 1845 (1992) (cit. on p. 55).
- [123] H. Zhang, Y. Wang, G. Zheng, J. Shen, Z. Shan, and D. Sellmyer, «The Temperature Dependence Of Perpendicular Anisotropy In Co/Pt And Co/Au Multilayer Films», *IEEE Transactions on Magnetism* **29** (1993) (cit. on pp. 55, 56).
- [124] Z. S. Shan, J. X. Shen, R. D. Kirby, and D. J. Sellmyer, «Temperature-dependent interface magnetism and magnetization reversal in Co/Pt multilayers», *Journ. Appl. Physics* **75** (1998) (cit. on p. 55).

- [125] J. Crangle and D. Parsons, «The magnetization of ferromagnetic binary alloys of cobalt or nickel with elements of the palladium and platinum groups», *Proceedings of the Royal Society A* **225**, 509 (1960) (cit. on pp. 59, 60).
- [126] J. Crangle and W. Scott, «Dilute Ferromagnetic Alloys», *Journal of Applied Physics* **36**, 921 (1965) (cit. on pp. 59, 60).
- [127] J. M. Sanchez, J. M. Moran-Lopez, C. Leroux, and M. C. Cadeville, «Magnetic properties and chemical ordering in Co-Pt», *Journ. of Phys.: Cond. Matt.* **1** (1989) (cit. on pp. 59, 60).
- [128] P. Imperia, W. Kandulski, A. Kosiorek, H. Glaczynska, H. Maletta, and M. Giersig, «Magnetic anisotropy study of triangular-shaped Co nanostructures», *J. Magn. Magn. Mater.* **320**, 2682 (2008) (cit. on p. 82).
- [129] S. Landis, B. Rodmacq, and B. Dieny, «Magnetic properties of Co/Pt multilayers deposited on silicon dot arrays», *Phys. Rev. B* **62**, 12271 (2000) (cit. on p. 82).
- [130] J. Lohau, S. Kirsch, A. Carl, and E. F. Wassermann, «Quantitative determination of the magnetization and stray field of a single domain Co/Pt dot with magnetic force microscopy», *Appl. Phys. Lett.* **76**, 3094 (2000) (cit. on p. 82).
- [131] A. Fernandez, P. Bedrossian, S. Baker, S. Vernon, and D. Kania, «Magnetic force microscopy of single-domain cobalt dots patterned using interference lithography», *IEEE Trans. Magn.* **32**, 4472 (1996) (cit. on p. 82).
- [132] M. A. M. Haast, J. R. Schuurhuis, L. Abelman, J. Lodder, and T. J. Popma, «Reversal mechanism of submicron patterned CoNi/Pt multilayers», *IEEE Trans. Magn.* **34**, 1006 (1998) (cit. on p. 82).
- [133] A. Lebib, S. Li, M. Natali, and Y. Chen, «Size and thickness dependencies of magnetization reversal in Co dot arrays», *J. Appl. Phys.* **89**, 3892 (2001) (cit. on p. 82).
- [134] L. Gao, S. Liou, M. Zheng, R. Skomski, M. Yan, D. Sellmyer, and N. Polushkin, «Magnetic force microscopy observations of the magnetic behavior in Co-C nanodot arrays», *J. Appl. Phys.* **91**, 7311 (2002) (cit. on p. 82).

Bibliography

- [135] V. Novosad, K. Guslienko, H. Shima, Y. Otani, S. Kim, K. Fukamichi, N. Kikuchi, O. Kitakami, and Y. Shimada, «Effect of interdot magnetostatic interaction on magnetization reversal in circular dot arrays», *Phys. Rev. B* **65**, 060402(R) (2002) (cit. on p. 82).
- [136] H. Takahoshi, H. Saito, and S. Ishio, «MFM analysis of magnetization process in CoPt dot-array», *J. Magn. Magn. Mater.* **272–276**, E1313 (2004) (cit. on p. 82).
- [137] X. Zhu and P. Grütter, «Imaging, Manipulation, and Spectroscopic Measurements of Nanomagnets by Magnetic Force Microscopy», *MRS Bull.* **2004**, 457 (2004) (cit. on p. 82).
- [138] B. D. Belle, F. Schedin, N. Pilet, T. V. Ashworth, E. W. Hill, P. W. Nutter, H. J. Hug, and J. J. Miles, «High resolution magnetic force microscopy study of e-beam lithography patterned Co/Pt nanodots», *J. Appl. Phys.* **101**, 09F517 (2007) (cit. on p. 82).
- [139] J. Chang, V. L. Mironov, B. A. Gribkov, A. A. Fraerman, S. A. Gusev, and S. N. Vdovichev, «Magnetic state control of ferromagnetic nanodots by magnetic force microscopy probe», *J. Appl. Phys.* **100**, 104304 (2006) (cit. on p. 82).
- [140] W. Pei, G. Qin, Y. Ren, S. Li, T. Wang, H. Hasegawa, S. Ishio, and H. Yamane, «Incoherent magnetization reversal in Co–Pt nanodots investigated by magnetic force microscopy», *Acta Mater.* **59**, 4818 (2011) (cit. on p. 82).
- [141] S. Krause, L. Berbil-Bautista, G. Herzog, M. Bode, and R. Wiesendanger, «Current-Induced Magnetization Switching with a Spin-Polarized Scanning Tunneling Microscope», *Science* **317**, 1537 (2007) (cit. on p. 82).
- [142] S. Krause, G. Herzog, T. Stapelfeldt, L. Berbil-Bautista, M. Bode, E. Y. Vedmedenko, and R. Wiesendanger, «Magnetization Reversal of Nanoscale Islands: How Size and Shape Affect the Arrhenius Prefactor», *Phys. Rev. Lett.* **103**, 127202 (2009) (cit. on pp. 82, 98, 99).
- [143] S. Krause, A. Sonntag, J. Hermenau, J. Friedlein, and R. Wiesendanger, «High-frequency magnetization dynamics of individual atomic-scale magnets», *Phys. Rev. B.* **93**, 064407 (2016) (cit. on pp. 82, 99).

- [144] W. Wernsdorfer, K. Hasselbach, D. Mailly, B. Barbara, A. Benoit, L. Thomas, and G. Suran, «DC-SQUID magnetization measurements of single magnetic particles», *J. Magn. Magn. Mater.* **145**, 33 (1995) (cit. on p. 82).
- [145] B. Barbara, W. Wernsdorfer, L. Sampaio, J. Park, C. Paulsen, M. Novak, R. Ferré, D. Mailly, R. Sessoli, A. Caneschi, K. Hasselbach, A. Benoit, and L. Thomas, «Mesoscopic quantum tunneling of the magnetization», *J. Magn. Magn. Mater.* **140–144**, 1825 (1995) (cit. on p. 83).
- [146] W. Wernsdorfer, K. Hasselbach, A. Benoit, W. Wernsdorfer, B. Barbara, D. Mailly, J. Tuaille, J. P. Perez, V. Dupuis, J. P. Dupin, G. Guiraud, and A. Perex, «High sensitivity magnetization measurements of nanoscale cobalt clusters», *J. Appl. Phys.* **78**, 7192 (1995) (cit. on pp. 83, 91).
- [147] W. Wernsdorfer, K. Hasselbach, D. Mailly, B. Barbara, A. Benoit, L. Thomas, and G. Suran, «Magnetization of single magnetic particles», *J. Magn. Magn. Mater.* **140–144**, 389 (1995) (cit. on p. 83).
- [148] W. Wernsdorfer, K. Hasselbach, A. Benoit, G. Cernicchiaro, D. Mailly, B. Barbara, and L. Thomas, «Measurement of the dynamics of the magnetization reversal in individual single-domain Co particles», *J. Magn. Magn. Mater.* **151**, 38 (1995) (cit. on p. 83).
- [149] K. Hasselbach, W. Wernsdorfer, D. Mailly, B. Barbara, and A. Benoit, «Magnetization reversal in single ferromagnetic Ni and Co particles», *Czech. J. Phys.* **46**, 2137 (1996) (cit. on pp. 83, 91).
- [150] B. Barbara and W. Wernsdorfer, «Quantum tunneling effect in magnetic particles», *Current Opinion in Solid State and Materials Science* **2**, 220 (1997) (cit. on p. 83).
- [151] B. Barbara, W. Wernsdorfer, E. B. Orozco, K. Hasselbach, A. Benoit, D. Mailly, N. Demoncy, H. Pascard, L. Francois, N. Duxin, and M. Pileni, «Submicron to Nanometer Size Single Particle Measurements», *Mat. Res. Soc. Symp. Proc.* **475**, 265 (1997) (cit. on p. 83).
- [152] W. Wernsdorfer, E. Bonet Orozco, K. Hasselbach, A. Benoit, D. Mailly, O. Kubo, H. Nakano, and B. Barbara, «Macroscopic Quantum Tunneling

Bibliography

- of Magnetization of Single Ferrimagnetic Nanoparticles of Barium Ferrite», *Phys. Rev. Lett.* **79**, 4014 (1997) (cit. on pp. 83, 91, 93).
- [153] W. Wernsdorfer, E. B. Orozco, K. Hasselbach, A. Benoit, B. Barbara, N. Demoncey, A. Loiseau, H. Pascard, and D. Mailly, «Experimental Evidence of the Néel-Brown Model of Magnetization Reversal», *Phys. Rev. Lett.* **78**, 1791 (1997) (cit. on pp. 83, 91).
- [154] W. Wernsdorfer, E. B. Orozco, B. Barbara, K. Hasselbach, A. Benoit, D. Mailly, B. Doudin, J. Meier, J. E. Wegrowe, J.-P. Ansermet, N. Demoncey, H. Pascard, N. Demoncey, A. Loiseau, L. Francois, N. Duxin, and M. P. Pileni, «Mesoscopic effects in magnetism: Submicron to nanometer size single particle measurements», *J. Appl. Phys.* **81**, 5543 (1997) (cit. on pp. 83, 91).
- [155] W. Wernsdorfer, E. Orozco, B. Barbara, A. Benoit, D. Mailly, N. Demoncey, H. Pascard, O. Kubo, and H. Nakano, «Magnetization reversal in individual nanoparticles - Macroscopic quantum tunneling of magnetization», *IEEE Trans. Magn.* **34**, 973 (1998) (cit. on p. 83).
- [156] W. Coffey, D. Crothers, J. Dormann, Y. Kalmykov, E. Kennedy, and W. Wernsdorfer, «Thermally activated relaxation time of a single domain ferromagnetic particle subjected to a uniform field at an oblique angle to the easy axis: Comparison with experimental observations», *Phys. Rev. Lett.* **80**, 5655 (1998) (cit. on p. 83).
- [157] E. Bonet, W. Wernsdorfer, B. Barbara, A. Benoit, D. Mailly, and A. Thiaville, «Three-dimensional magnetization reversal measurements in nanoparticles», *Phys. Rev. Lett.* **83**, 4188 (1999) (cit. on pp. 83, 91).
- [158] O. Fruchart, J. Nozieres, W. Wernsdorfer, D. Givord, F. Rousseaux, and D. Decanini, «Enhanced coercivity in submicrometer-sized ultrathin epitaxial dots with in-plane magnetization», *Phys. Rev. Lett.* **82**, 1305 (1999) (cit. on p. 83).
- [159] E. Bonet Orozco, W. Wernsdorfer, B. Barbara, A. Benoit, D. Mailly, and A. Thiaville, «Uniform rotation of magnetization measured in single nanometer-sized particles», *J. Appl. Phys.* **87**, 5097 (2000) (cit. on p. 83).

- [160] W. Wernsdorfer, D. Mailly, and A. Benoit, «Single nanoparticle measurement techniques», *J. Appl. Phys.* **87**, 5094 (2000) (cit. on p. 83).
- [161] M. Jamet, W. Wernsdorfer, C. Thirion, D. Mailly, V. Dupuis, P. Mélinon, and A. Pérez, «Magnetic Anisotropy of a Single Cobalt Nanocluster», *Phys. Rev. Lett.* **86**, 4676 (2001) (cit. on pp. 83, 91, 94, 95).
- [162] W. Wernsdorfer, C. Thirion, N. Demoncey, H. Pascard, and D. Mailly, «Magnetisation reversal by uniform rotation (Stoner-Wohlfarth model) in FCC cobalt nanoparticles», *J. Magn. Magn. Mater.* **242**, 132 (2002) (cit. on p. 83).
- [163] C. Thirion, W. Wernsdorfer, and D. Mailly, «Switching of magnetization by nonlinear resonance studied in single nanoparticles», *Nat. Mater.* **2**, 524 (2003) (cit. on p. 83).
- [164] M. Jamet, W. Wernsdorfer, C. Thirion, V. Dupuis, P. Melinon, A. Perez, and D. Mailly, «Magnetic anisotropy in single clusters», *Phys. Rev. B* **69**, 024401 (2004) (cit. on pp. 83, 91).
- [165] C. Thirion, W. Wernsdorfer, M. Klaui, C. A. F. Vaz, P. Lewis, H. Ahmed, J. A. C. Bland, and D. Mailly, «Anisotropy engineering in Co nanodiscs fabricated using prepatterned silicon pillars», *Nanotechnology* **17**, 1960 (2006) (cit. on p. 83).
- [166] W. Wernsdorfer, «From micro- to nano-SQUIDs: applications to nanomagnetism», *Supercond. Sci. Tech.* **22**, 064013 (2009) (cit. on pp. 83, 91).
- [167] D. Grundler, G. Meier, K. Brooks, C. Heyn, and D. Heitmann, «Magnetization of small arrays of interacting single-domain particles», *J. Appl. Phys.* **85**, 6175 (1999) (cit. on p. 83).
- [168] Y. Li, P. Xiong, S. von Molnár, Y. Ohno, and H. Ohno, «Magnetization reversal in elongated Fe nanoparticles», *Phys. Rev. B* **71**, 214425 (2005) (cit. on p. 83).
- [169] Z.-P. Li, O. Petravic, J. Eisenmenger, and I. Schuller, «Reversal behavior of exchange-biased submicron dots», *Appl. Phys. Lett.* **86**, 072501 (2005) (cit. on p. 83).

Bibliography

- [170] S. Wirth and S. von Molnár, «Hall cross size scaling and its application to measurements on nanometer-size iron particle arrays», *Appl. Phys. Lett.* **76**, 3283 (2000) (cit. on p. 83).
- [171] S. Wirth and S. von Molnár, «Magnetic interactions in nanometer-scale particle arrays grown onto permalloy films», *J. Appl. Phys.* **87**, 7010 (2000) (cit. on p. 83).
- [172] S. Wirth and S. Von Molnar, «Thermally and field driven magnetization processes in nanometer-scale particle arrays», *IEEE Trans. Magn.* **37**, 2182 (2001) (cit. on p. 83).
- [173] Y. Li, P. Xiong, S. von Molnar, S. Wirth, Y. Ohno, and H. Ohno, «Hall magnetometry on a single iron nanoparticle», *Appl. Phys. Lett.* **80**, 4644 (2002) (cit. on p. 83).
- [174] A. Candini, G. C. Gazzadi, A. Di Bona, M. Affronte, D. Ercolani, G. Biasiol, and L. Sorba, «Hall nano-probes fabricated by focused ion beam», *Nanotechnology* **17**, 2105 (2006) (cit. on p. 83).
- [175] G. Mihajlovic, P. Xiong, S. von Molnar, M. Field, G. Sullivan, K. Ohtani, and H. Ohno, «Submicrometer Hall Sensors for Superparamagnetic Nanoparticle Detection», *IEEE Trans. Magn.* **43**, 2400 (2007) (cit. on p. 83).
- [176] A. D. Kent, S. von Molnár, S. Gider, and D. D. Awschalom, «Properties and measurement of scanning tunneling microscope fabricated ferromagnetic particle arrays (invited)», *J. Appl. Phys.* **76**, 6656 (1994) (cit. on p. 83).
- [177] N. Kikuchi, S. Okamoto, O. Kitakami, Y. Shimada, and K. Fukamichi, «Sensitive detection of irreversible switching in a single FePt nanosized dot», *Appl. Phys. Lett.* **82**, 4313 (2003) (cit. on p. 83).
- [178] N. Kikuchi, R. Murillo, and J. Lodder, «AHE measurements of very thin films and nanosized dots», *J. Magn. Magn. Mater.* **287**, 320 (2005) (cit. on p. 83).
- [179] N. Kikuchi, R. Murillo, and J. Lodder, «Anomalous Hall-effect measurement study on Co/Pt nanosized dot», *J. Appl. Phys.* **97**, 10J713 (2005) (cit. on p. 83).

- [180] N. Kikuchi, T. Kato, S. Okamoto, O. Kitakami, N. Tezuka, and S. Sugimoto, «Magnetization reversal process and bistability of Co/Pt multilayer dot», *J. Appl. Phys.* **103**, 07C510 (2008) (cit. on p. 83).
- [181] S. Okamoto, T. Kato, N. Kikuchi, O. Kitakami, N. Tezuka, and S. Sugimoto, «Energy barrier and reversal mechanism in Co/Pt multilayer nanodot», *J. Appl. Phys.* **103**, 07C501 (2008) (cit. on p. 83).
- [182] T. Shimatsu, H. Kataoka, K. Mitsuzuka, H. Aoi, N. Kikuchi, and O. Kitakami, «Dry-etching damage to magnetic anisotropy of Co-Pt dot arrays characterized using anomalous Hall effect», *J. Appl. Phys.* **111**, 07B908 (2012) (cit. on p. 83).
- [183] H. Kronmüller, «The Nucleation Fields of Uniaxial Ferromagnetic Crystals», *Phys. Stat. Sol. (b)* **130**, 197 (1985) (cit. on p. 85).
- [184] C.-R. Chang and D. R. Fredkin, «The mechanism of nucleation in uniaxial ferromagnets», *J. Appl. Phys.* **63**, 3435 (1988) (cit. on p. 85).
- [185] P. L. Fulmek and H. Hauser, «Coercivity and switching field of single domain γ -Fe₂O₃ particles under consideration of the demagnetizing field», *J. Appl. Phys.* **76**, 6561 (1994) (cit. on pp. 87, 91).
- [186] A. Thiaville, «Extensions of the geometric solution of the two dimensional coherent magnetization rotation model», *Journal of Magnetism and Magnetic Materials* **182**, 5 (1998) (cit. on pp. 87, 89, 115).
- [187] A. Thiaville, «Coherent rotation of magnetization in three dimensions: A geometrical approach», *Phys. Rev. B* **61**, 12221 (2000) (cit. on pp. 87, 89, 90, 91, 115).
- [188] M. Sharrock and J. McKinney, «Kinetic effects in coercivity measurements», *IEEE Trans. Magn.* **17**, 3020 (1981) (cit. on p. 92).
- [189] M. Sharrock, «Time-dependent magnetic phenomena and particle-size effects in recording media», *IEEE Trans. Magn.* **26**, 193 (1990) (cit. on p. 92).
- [190] R. W. Chantrell, G. N. Coverdale, and K. O'Grady, «Time dependence and rate dependence of the coercivity of particulate recording media», *J. Phys. D: Appl. Phys.* **21**, 1469 (1988) (cit. on p. 92).

Bibliography

- [191] A. de Witte, M. El-Hilo, K. O'Grady, and R. Chantrell, «Sweep rate measurements of coercivity in particulate recording media», *J. Magn. Magn. Mater.* **120**, 184 (1993) (cit. on p. 92).
- [192] M. El-Hilo, A. de Witte, K. O'Grady, and R. Chantrell, «The sweep rate dependence of coercivity in recording media», *J. Magn. Magn. Mater.* **117**, L307 (1992) (cit. on p. 92).
- [193] D. J. Sellmyer and R. Skomski (Eds.), *Advanced Magnetic Nanostructures* (Springer Science+Business Media, Inc., 2006) (cit. on p. 93).
- [194] R. R. Rao and A. Ramanand, «Third-order elastic constants of uniaxial crystals», *Phys. Stat. Sol. (a)* **58**, 11 (1980) (cit. on p. 93).
- [195] E. Torre and F. Vajda, «The identification of the switching field distribution components», *IEEE Trans. Magn.* **31**, 2536 (1995) (cit. on p. 93).
- [196] V. V. Kruglyak, S. O. Demokritov, and D. Grundler, «Magnonics», *J. Phys. D: Appl. Phys.* **43**, 264001 (2010) (cit. on p. 93).
- [197] J. Dormann, D. Fiorani, and E. Tronc, «On the models for interparticle interactions in nanoparticle assemblies: comparison with experimental results», *J. Magn. Magn. Mater.* **202**, 251 (1999) (cit. on p. 98).
- [198] S. Rohart, P. Campiglio, V. Repain, Y. Nahas, C. Chacon, Y. Girard, J. Lagoute, A. Thiaville, and S. Rousset, «Spin-Wave-Assisted Thermal Reversal of Epitaxial Perpendicular Magnetic Nanodots», *Phys. Rev. Lett.* **104**, 137202 (2010) (cit. on pp. 98, 99).
- [199] J. Lee, C. Brombacher, J. Fidler, B. Dymerska, D. Suess, and M. Albrecht, «Contribution of the easy axis orientation, anisotropy distribution and dot size on the switching field distribution of bit patterned media», *Appl. Phys. Lett.* **99**, 062505 (2011) (cit. on p. 99).
- [200] P. Campiglio, N. Moreau, V. Repain, C. Chacon, Y. Girard, J. Klein, J. Lagoute, S. Rousset, H. Bulou, F. Scheurer, C. Goyhenex, P. Ohresser, E. Fonda, and H. Magnan, «Interplay between interfacial and structural properties on the magnetism of self-organized core-shell Co/Pt supported nanodots», *Phys. Rev. B* **84**, 235443 (2011) (cit. on p. 99).

- [201] M. Stier, A. Neumann, A. Philippi-Kobs, H. Oepen, and M. Thorwart, «Implications of a temperature-dependent magnetic anisotropy for superparamagnetic switching», *J. Magn. Magn. Mater.* **447** (2018) (cit. on p. 100).
- [202] S. Freercks, *Temperaturabhängigkeit der Anisotropie in ferromagnetischen Nanostrukturen*, Master's thesis (2015) (cit. on p. 101).
- [203] A. Hevroni, B. Tsukerman, and G. Markovich, «Probin magnetization dynamics in individual magnetite nanocrystals using magnetoresistive scanning tunneling microscopy», *Phys. Rev. B* **92** (2015) (cit. on p. 102).
- [204] P. J. Metaxas, J. P. Jamet, A. Mougin, M. Cormier, J. Ferré, V. Baltz, B. Rodmacq, B. Dieny, and R. L. Stamps, «Creep and Flow Regimes of Magnetic Domain-Wall Motion in Ultrathin Pt/Co/Pt Films with Perpendicular Anisotropy», *Phys. Rev. Lett.* **99**, 217208 (2007) (cit. on p. 109).
- [205] J. Kalezhi, J. Miles, and B. Belle, «Dependence of Switching Fields on Island Shape in Bit Patterned Media», *IEEE Trans. Magn.* **45**, 3531 (2009) (cit. on p. 110).

Publications

Articles

S. Freercks, S. Hesse, A. Neumann, P. Staeck, C. Thönnißen, E.-S. Wilhelm, and H.P. Oepen, «Magnetic Behavior of Single Nanostructures and Their Mutual Interactions in Small Ensembles », [Atomic- and Nanoscale Magnetism](#), Springer,2018

Conference Contributions

S. Freercks, A. Neumann, C. Thönnißen, A. Kobs, E.-S. Wilhelm, and H. P. Oepen, «The influence of a temperature dependent anisotropy on the attempt frequency of single superparamagnetic nanodots», Talk at the Spring-meeting of the German Physical Society (DPG) 2016, Regensburg (Germany)

J. Wagner, K. Bagschik, S. Freercks, A. Kobs, R. Frömter, L. Müller, M. H. Berntsen, G. Grübel, and H. P. Oepen, «Imaging of magnetic nanodots utilizing soft X-ray holographic microscopy», Talk at the Spring-meeting of the German Physical Society (DPG) 2016, Regensburg (Germany)

J. Wagner, K. Bagschik, S. Freercks, A. Kobs, R. Frömter, L. Müller, M. H. Berntsen, G. Grübel, and H. P. Oepen, «X-ray holographic imaging of magnetic nanostructures and spatial coherence determination», Talk at PETRA III P04 Users Meeting 2016, Hamburg (Germany)

J. Wagner, R. Frömter, K. Bagschik, S. Freercks, C. Thönnißen, B. Beyersdorff, L. Müller, S. Schleitzer, M. H. Berntsen, J. Viefhaus, G. Grübel, and H. P. Oepen, «Arrays of magnetic nanodots studied by X-ray holographic microscopy and scattering », Poster at MMM 2016, New Orleans (USA)

Publications

K. Bagschik, R. Frömter, J. Wagner, S. Freercks, C. Thönnißen, J. Bach, B. Beyersdorff, H. P. Oepen, L. Müller, S. Schleiter, G. Grübel, M. H. Berntsen, C. Weier, R. Adam, and C. M. Schneider, «Imaging of magnetic nanodots utilizing soft X-ray holographic microscopy», Poster at PETRA III Variable Polarization XUV Beamline P04 User Meeting 2016, Hamburg (Germany)

S. Freercks, C. Thönnißen, E.-S. Wilhelm, P. Staeck, and H. P. Oepen, «Determining anisotropy and magnetic moment of single nanodots from switching time measurements», Talk at the Spring-meeting of the German Physical Society (DPG) 2017, Dresden (Germany)

S. Freercks, P. Staeck, C. Thönnißen, E.-S. Wilhelm, A. Neumann, and H. P. Oepen, «Magnetization behavior and interactions of single magnetic nanodots», Poster at the Spring-meeting of the German Physical Society (DPG) 2017, Dresden (Germany)

J. Wagner, R. Frömter, K. Bagschik, S. Freercks, C. Thönnißen, B. Beyersdorff, L. Müller, S. Schleiter, M. H. Berntsen, J. Viefhaus, G. Grübel, and H. P. Oepen, «Arrays of magnetic nanodots studied by X-ray holographic microscopy and scattering», Poster at DESY Photon Science User Meeting 2017, Hamburg (Germany).

J. Wagner, R. Frömter, K. Bagschik, S. Freercks, C. Thönnißen, B. Beyersdorff, R. Buss, M. Riepp, A. Philippi-Kobs, L. Müller, S. Schleiter, M. H. Berntsen, J. Viefhaus, G. Grübel, and H. P. Oepen, «Arrays of magnetic Nanodots studied by X-ray holographic Microscopy and scattering», Poster at the Spring-meeting of the German Physical Society (DPG) 2017, Dresden (Germany)

E.-S. Wilhelm, S. Freercks, P. Staeck, C. Thönnißen, and H.P. Oepen, «Noncoherent reversal of magnetization in single Pt/Co/Pt nanodots with diameter below 100nm», Talk at the Spring-meeting of the German Physical Society (DPG) 2018, Dresden (Berlin)

S. Freercks E.-S. Wilhelm, C. Thönnißen, P. Staeck, and H. P. Oepen, «Temperature dependence of the magnetic anisotropy of Pt/Co/Pt nanodots», Talk at the Spring-meeting of the German Physical Society (DPG) 2018, Berlin (Germany)

Danksagung

Zuletzt möchte ich mich bei all denjenigen bedanken, die die Fertigstellung der Dissertation ermöglicht haben:

Prof. Dr. Oepen, für die Möglichkeit die Arbeit in der Gruppe G anzufertigen, die Betreuung der Arbeit und die vielen fachlichen Beiträge, insbesondere beim Interface Model.

Prof. Dr. Blick für die Übernahme des Zweitgutachtens.

Dr. Eva-Sophie Wilhelm und Dr. Carsten Thönnißen für die gemeinsame Arbeit in dem Projekt und die Korrekturen an der Arbeit.

Dr. Philip Staeck für die Simulation der Schaltfläche.

Dr. André Kobs für die Zusammenarbeit bei den ultradünnen Filmen.

Dr. Robert Frömter für vielfältige Unterstützung im Labor, während des Institutssumzugs und allgemein neuer Denkanstöße.

Dr. Alexander Neumann und Jonathan Jacobsohn für die Einarbeitung in die Arbeitsgruppe.

Dr. Jochen Wagner und Dr. Kai Bagschick für die Zusammenarbeit im Holographie Projekt.

Simon Marotzke und Jackson Barp für die Messungen der dünnen Filme.

Matthias Riepp für die Zusammenarbeit bei der E-Beam Lithographie.

Dr. Robert Zierold für die Unterstützung bei den Messungen am Dynacool.

Sonja Hesselmann für die Probenpräparationen und Unterstützung im Labor.

Brigitte Muhlack und Stephanie Baer für administrative Unterstützung.

Prof. Dr. Huse, der die Arbeitsgruppe übernommen hat. Für die nette Arbeitsatmosphäre bedanke ich mich bei allen Mitgliedern der Gruppe G.

Bei meiner Familie bedanke ich mich für die Unterstützung und die aufgebrachte Geduld.

Eidesstattliche Versicherung / Declaration on oath

Hiermit versichere ich an Eides statt, die vorliegende Dissertationsschrift selbst verfasst und keine anderen als die angegebenen Hilfsmittel und Quellen benutzt zu haben. Die eingereichte schriftliche Fassung entspricht der auf dem elektronischen Speichermedium. Die Dissertation wurde in der vorgelegten oder einer ähnlichen Form nicht schon einmal in einem früheren Promotionsverfahren angenommen oder als ungenügend beurteilt.

Hamburg, im August 2020